

Clemson University

TigerPrints

All Dissertations

Dissertations

May 2021

The Fundamentals of Fretting Crevice Corrosion of Metallic Biomaterials for Orthopedic Implants

Dongkai Zhu

Clemson University, zhudongkai1990@gmail.com

Follow this and additional works at: https://tigerprints.clemson.edu/all_dissertations

Recommended Citation

Zhu, Dongkai, "The Fundamentals of Fretting Crevice Corrosion of Metallic Biomaterials for Orthopedic Implants" (2021). *All Dissertations*. 2772.

https://tigerprints.clemson.edu/all_dissertations/2772

This Dissertation is brought to you for free and open access by the Dissertations at TigerPrints. It has been accepted for inclusion in All Dissertations by an authorized administrator of TigerPrints. For more information, please contact kokeefe@clemson.edu.

THE FUNDAMENTALS OF FRETTING CREVICE CORROSION OF METALLIC
BIOMATERIALS FOR ORTHOPEDIC IMPLANTS

A Dissertation
Presented to
the Graduate School of
Clemson University

In Partial Fulfillment
of the Requirements for the Degree
Doctor of Philosophy
Bioengineering

by
Dongkai Zhu
May 2021

Accepted by:

Dr. Jeremy L. Gilbert
Dr. John D. Desjardins
Dr. Melinda K. Harman
Dr. Hai Yao

ABSTRACT

Metallic medical devices have been widely used in clinical applications, especially for joint arthroplasty or joint replacement surgery. Fretting corrosion, one of the most common forms of mechanically-assisted corrosion (MAC), has become a major concern associated with orthopedic medical devices. Crevice corrosion, a second mechanism of corrosion related to metallic medical devices, is a second factor of corrosion for many circumstances in medical devices that is an additional factor in the overall corrosion performance of these implants. It is a form of localized corrosion of metal surfaces present within the gap or crevice between two adjoining interfaces. The relationship and interplay between fretting and crevice corrosion is poorly understood and the observed damage seen in retrievals, which includes pitting, selective dissolution, intergranular and interphase corrosion has not been adequately duplicated in in vitro tests of mechanically assisted crevice corrosion.

CoCrMo alloy, Ti-6Al-4V alloy and stainless steel are the principal alloys in use today in orthopedics and are the focus of corrosion related studies. In addition, alternative materials, including ceramic materials with trusted biocompatibility, are also playing an increasingly-important role in medical device implantation. Here, we performed a series of studies intended to explore the fundamentals of fretting crevice corrosion of metallic biomaterials for orthopedic implants. We first studied CoCrMo alloy fretting corrosion debris generation and distribution using a range of characterization techniques and a custom-made fretting corrosion testing system. These several analytical surface

techniques include SEM/EDS, AFM, and XPS. They were used to determine what debris was generated and to where it was distributed. Also, solution chemistry measurement (using ICP-MS) after testing was included to determine which ions and in what proportion remained in the solution. Next, a tribocorrosion model, which linked fretting mechanics, current and potential, was developed to predict currents and potential shifts resulting from fretting corrosion based on tribocorrosion theory. The model was tested against controlled fretting corrosion test conditions for its ability to predict the current-time and potential-time response. This model established a strong connection between mechanical and electrochemical aspects to demonstrate that potential and current affect each other during tribocorrosion and both are affected by other electrochemical factors (electrode area, impedance, contact mechanics, etc.) In the next step, fretting-initiated crevice corrosion in stainless steel alloys was observed and described, where fretting disruption of the surface initiated a self-sustained crevice corrosion reaction that continued even in the absence of additional fretting. The result was to comprehensively investigate fretting initiated-crevice corrosion (FICC) mechanism of stainless steel and to explore the factors, including potential and fretting duration that leads to this process. Lastly, device testing using the MTS servo-hydraulic test frame was performed to measure fretting corrosion performance of Si_3N_4 heads/Ti-6Al-4V modular tapers for total hip replacements *in vitro* and compared their behavior to standard CoCrMo heads/Ti-6Al-4V modular tapers tested under identical conditions. It was shown that using a Si_3N_4 ceramic head on metal trunnion significantly reduced the fretting corrosion reactions present.

ACKNOWLEDGMENTS

I want to express my sincere thankfulness to everyone I mention below. This work would not been done without their help. I would first like to thank my advisor, Dr. Jeremy Gilbert, for the time, energy, and patience he has dedicated to both my research and my career. As my research advisor, Dr. Gilbert never hesitated to help me to understand new knowledge and guide me for each project I have done so far. As my mentor for professional development, he makes me a well-trained engineer who has confidence to face challenges in the future. I hope one day I can be the type of mentor he was to me.

I also want to express thankfulness to the committee members who provide incredibly support to help me complete my research. Dr. John Desjardins, Dr. Hai Yao, and Dr. Melinda Harman all provided valuable insight and guidance into my dissertation and my research work.

This work would not be completed without the help of people from the Gilbert lab, past and present. Specifically, I want to thank Dr. Yangping Liu, Dr. Stephanie Smith, Dr. Piyush Khullar, Dr. Aarti Shenoy and Can Aslan for their assistance and collaborations.

I want to say thanks to all faculty and staff of Clemson-MUSC Bioengineering Program and the department of bioengineering in Clemson University for assisting me to pursue the degree. Some of the work were completed at the Syracuse Biomaterials Institute in Syracuse University. I also want to thank all the people I met in there, faculty and staff from the department of biomedical and chemical engineering and machine shop.

Syracuse University will always have a special place in my heart. I would also like to acknowledge the funding sources that have supported my research, including the Wyss Foundation, Bausch and Lomb Incorporated and SINTX Technologies.

Lastly, I want to thank my family, especially my parents and my wife, for supporting me in the past few years. As an international student, it is difficult for studying abroad and I could not have done it without their love, support, and encouragement.

TABLE OF CONTENTS

	Page	
TITLE PAGE	i	
ABSTRACT.....	ii	
ACKNOWLEDGMENTS	iv	
LIST OF TABLES	viii	
LIST OF FIGURES	ix	
CHAPTER		
1. Introduction		
1.1 Metallic Biomaterials and Total Joint Arthroplasty (TJA).....	1	
1.2 Mechanical Assisted Crevice Corrosion (MACC)	4	
1.3 MACC on Metallic Implant Materials	9	
1.4 Challenges.....	13	
1.5 Goals	15	
2. Aims and Hypotheses		17
2.1 <i>In vitro</i> fretting crevice corrosion damage of CoCrMo alloys in phosphate buffered saline	17	
2.2 A metallic biomaterial tribocorrosion model linking fretting mechanics, currents, and potentials	18	
2.3 Fretting initiated crevice corrosion of 316LVM stainless steel in physiological phosphate buffered saline	19	
2.4 Fretting corrosion of Si ₃ N ₄ vs CoCrMo femoral heads on Ti-6Al-4V trunnions	19	
3. <i>In vitro</i> Fretting Crevice Corrosion Damage of CoCrMo alloys in Phosphate Buffered Saline: Debris Generation, Chemistry and Distribution		21
3.1 Introduction.....	21	
3.2 System Development	23	
3.3 Materials and Methods.....	23	
3.4 Results.....	30	
3.5 Discussion	41	

3.6 Conclusions.....	47
4. Metallic Biomaterial Tribocorrosion Model Linking Fretting Mechanics, Currents, and Potentials: Model Development and Experimental Comparison	48
4.1 Introduction.....	48
4.2 Fretting Corrosion Model	51
4.3 Materials and Methods.....	64
4.4 Results.....	72
4.5 Discussion.....	80
4.6 Conclusions.....	88
5. Fretting Initiated Crevice Corrosion of 316LVM Stainless Steel in Physiological Phosphate Buffered Saline: Potential and Cycles to Initiation	90
5.1 Introduction.....	90
5.2 Materials and Methods.....	93
5.3 Results.....	99
5.4 Discussion.....	112
5.5 Conclusions.....	122
6. Fretting Corrosion of Si ₃ N ₄ vs CoCrMo Femoral Heads on Ti-6Al-V Trunnions. 124	
6.1 Introduction.....	124
6.2 Materials and Methods.....	126
6.3 Results.....	130
6.4 Discussion.....	138
6.5 Conclusions.....	144
7. Synthesis of the Work.....	146
7.1 General Discussion	146
7.2 Detail of Accomplishments.....	148
8. Future Work	155
9. Conclusions.....	157
10. References.....	160

LIST OF TABLES

Table		Page
3.1	Composition of CoCrMo.	27
4.1	Nomenclature table for parameters terminology	52
4.2	Oxide physical properties based on Mole fraction estimation of alloy composition.....	69
4.3	Parameters used for current and voltage calculations.....	70
4.4	Parameters used in scratch test to calculate theoretical current.....	72
4.5	Parameters used for current calculation in different waveform and different solution.....	79

LIST OF FIGURES

Figure	Page
1.1	A schematic of modular taper junction of common total hip arthroplasty. 3
1.2	Schematic showing MACC of a passive metal and the associated redox reactions..... 7
3.1	(A) Schematic of the fretting corrosion test system and (B) 3D schematic of electrochemical part 26
3.2	Digital microscope image of debris generation from CoCrMo pin and disk at different time 31
3.3	(a) Optical micrograph of the fretted surface covered by debris. (b) A colored halo region was observed around the debris region. (c) A higher magnification optical image of the rainbow area..... 32
3.4	SEM pictures of sample surface and debris 35
3.5	EDS mapping result of fretting surface 36
3.6	a,b) show atomic concentration variation; intensity and binding energy of Cr2p (c, d) and Co2p (e, f) peaks at different depth on fretted and unfretted areas 38
3.7	AFM contact mode images ($30 \times 30 \mu\text{m}^2$) of surface after fretting corrosion test. 40
3.8	ICP-MS result 41
4.1	High field film currents with oxide thickness based on Gunter-Schulze Betz Eqn..... 54
4.2	Schematic of the disruption-repassivation process of an asperity 58
4.3	Pin-on-disk impedance-model used in this study to relate potential-time behavior to abrasion-time behavior 62

4.4	A simple algorithm for the coupled iterative calculation of both the $V(t)$ and $I(t)$ heredity integrals over time.....	64
4.5	Examples of fretting current and potential time plots from both experiments and Duhamel integral calculations for a) 0.2 Hz, b) 1 Hz, and c) 5 Hz	74
4.6	A high temporal resolution example from a 0.5 Hz test of the current vs time and potential versus time for both experiment and theory.....	75
4.7	Summary analysis of a) average and root mean square about the average currents and b) potential drop during fretting corrosion of CoCrMo surfaces under controlled loads, electrode area and sliding distance as a function of sliding frequency	76
4.8	a) Examples of single asperity diamond scratch currents at different loads and speeds	77
4.9	Summary of optical micrograph measurement of scratch widths in CoCrMo surfaces under controlled loads using the diamond stylus.....	78
4.10	Summary of experimental and calculated fretting current in (a) sine-wave and (b) square-wave	79
4.11	Summary of average fretting current between 4 s to 8 s in (a) DMEM and (b) PBS	80
5.1	Schematic of a) 3D and b) 2D fretting corrosion systems	96
5.2	a) 3D Convex geometry of pin by Digital Optical Microscopy, note the vertical scale is expanded to emphasize the slight convexity; b) Contact, crevice and depth profile features on pin surface after test; c) Fretting load-displacement plot for one cycle of fretting motion	100
5.3	Current profile during fretting corrosion tests at different voltages	101
5.4	Potential-dependent regions of fretting corrosion and FICC behavior of 316 SS.....	103

5.5	SEM images of fretting contact regions after tests at different potentials Continue listing your figure captions here	105
5.6	Element mapping of surface after FICC at 200 mV by low kV (6 kV) EDS.....	106
5.7	AFM tapping mode images (50*50 μm^2) of surface after FICC test at 250 mV	108
5.8	a, b) 2D pin-on-disk interface before and after fretting by digital optical microscopy and c) Pin-on-disk interface after initiation of crevice corrosion at different time points at 250 mV.....	109
5.9	a) Current profile of FICC induced by fretting within 2 s. b) Circle-by circle crevice feature. c) Depth profile across the crevice surface. d) Digital optical microscopy depth analysis of surface damage.....	110
5.10	3D imaging and depth profile analysis of crevice corrosion area after 120 s of fretting and different FICC times (a.1 min, b.15 min, c. 90 min) at 250 mV	111
5.11	Cyclic potentiodynamic polarization curve of stainless steel	112
6.1	Schematic of assembled femoral head-neck taper immersed in phosphate buffer solution with three electrochemical setups	127
6.2	Schematic showing the complete testing protocol including static seating, short term ICFC test, one million cycles test, pull-off and post-test analysis methodology	130
6.3	(A) Typical example of currents (vs time) measured using the electrochemical setup for CoCrMo head. (B) Fretting currents recorded at three load levels (at about 2 hours, and above onset load) for CoCrMo head. (C) One second fretting currents at 3600 N (circled in B) is shown consisting of three higher and three smaller current peaks directly associated with the cyclic loading	132

6.4	RMS current vs max cyclic load for Si ₃ N ₄ head and CoCrMo head.....	133
6.5	Box plots showing fretting currents at three load levels for Si ₃ N ₄ and CoCrMo heads.....	134
6.6	(A) Fretting currents vs time at 3200 N (15 Hz) for both Si ₃ N ₄ and CoCrMo heads during 1 million cycle fretting tests.....	135
6.7	Box plot of pull-off forces measured during head-neck disengagement for Si ₃ N ₄ and CoCrMo samples.....	136
6.8	Scanning electron microscopy image and EDS spectra of a Ti-6Al-4V trunnion that interfaced with a CoCrMo femoral head.....	137
6.9	Scanning electron microscopy image and EDS spectra of a Ti-6Al-4V trunnion that interfaced with a Si ₃ N ₄ femoral head.....	137
6.10	(A) CoCrMo head (inferior). (B) Si ₃ N ₄ head (inferior) that interfaced with Ti-6Al-4V trunnion	138

1. Introduction

1.1 Metallic Biomaterials and Total Joint Arthroplasty (TJA)

Total joint arthroplasty (TJA) is considered as one of the most successful orthopedic surgeries performed today. Within this category, the number of cases of total hip arthroplasty (THA) shows a rapidly increasing growth trend with an increasing rate since 2002 [1-2]. There are many reasons that may lead to THA procedures, such as femoral-neck fracture, osteoarthritis, degenerative arthritis and even tumor etc. [3-5]. The average age of the patient population who receives these surgeries shows a decreasing trend which indicates that long-lasting implants are a mandatory aspect to consider when developing new orthopedic implants related to THA [6].

Metallic orthopedic devices, such as modular hip joint replacements, have been widely used in THA over decades. Many metallic biomaterials like stainless steel (316LSS), titanium-based alloy (Ti-6Al-4V) and cobalt-chromium alloy (CoCrMo) have been documented as suitable implant materials [7]. The main reason behind these popular materials is that they have excellent mechanical properties and biocompatibility. CoCrMo alloy and Ti-6Al-4V are widely used in total hip arthroplasty surgery, where CoCrMo alloy is mainly for manufacturing femoral heads due to its excellent wear properties, while Ti-6Al-4V serves as the stem to avoid stress shielding and enhance bone in growth [8-9]. 316L stainless steel has been used for bone plates, bone screws and cardiovascular stents due to its excellent corrosion resistance and reasonable cost. However, compared with CoCrMo or Ti-6Al-4V, the surface oxide of 316L stainless steel is highly dynamic under many physiological conditions [10] and is more susceptible to breakdown.

A typical artificial hip joint for THA is made by several components: a metallic acetabular shell (typically Ti-alloy), a liner that is usually made from a polymeric material (ultra-high molecular weight polyethylene, UHMWPE) sits in the shell, a femoral head (made from CoCrMo or ceramic), and a stem (typically Ti-Alloy or CoCrMo, and sometimes 316L SS). This modular design allows each different material to achieve their maximum contribution to the overall design. The modular components are easy to assemble in different sizes and shapes, which allow for highly customizable implants to be considered based on each individual circumstance. Also, this design allows the surgeon to easily revise portions of the construct during revision surgery without having to remove the whole device and potentially induce significant damage to the bony structures of the joint.

The common connection type used in THA to connect components is a physical locking connection of a conical tapered construct known as the modular taper (Figure 1.1). Multiple modular junctions exist in a range of hip replacements and each consists of a pair of modular components fitting together, one male the other female. More specifically, this could happen between the shell and liner, within the stem, between the stem and neck, and most commonly, head and neck taper junction.

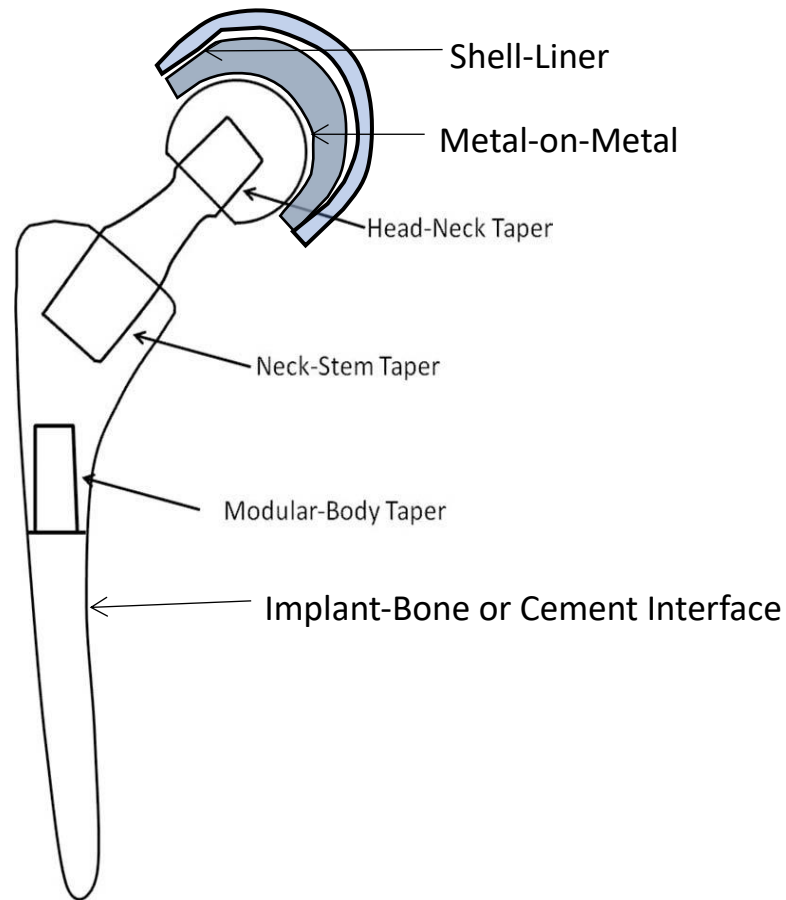


Fig. 1.1. A schematic of modular taper junction of common total hip arthroplasty [53].

The stem-bone connection is usually by biological fixation, where a porous meshed surface is created on the stem surface for bone cells, e.g., osteoblast, to grow into and to create bone in the interstitial spaces [11] locking the implant in place. Physical fixation of components to each other, using modular taper junctions, can raise potential concerns after patients received THA, such as wear and stress concentration, and could directly lead to device failure, e.g., dislocation and fracture, which has been well-documented over decades [12-13]. This is because the activities of daily living, e.g.,

walking, could apply forces and torsion on each junction, which will cause undetected micromotion (i.e., fretting), and lead to corrosion. The associated electrochemical (corrosion) reactions could cause metallic material degradation and disfunction of the device may eventually occur.

a 1.2 Mechanical Assisted Crevice Corrosion (MACC)

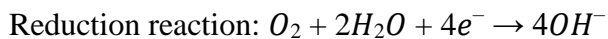
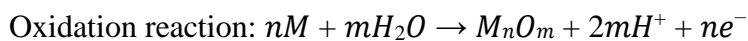
Even though different implant materials used within modular designs provide a variety of choices for THA, metallic implant materials are still required within modular junctions and these may still suffer from MAACC-based failure modes. Many failures have been reported *in vivo* related primarily to corrosion processes, which can significantly limit implant lifetime [14-16]. Metal-metal or metal-ceramic modular connections (e.g., modular taper junctions) cannot avoid the generation of corrosion and fretting debris that may result in biocompatibility concerns. Implant corrosion, which may in some cases be associated with revision surgery, is associated with loosening, local tissue reactions and other issues. Biological reactions, like local inflammatory reactions, stress shielding, pain in the joint and osteolysis, to name a few have been associated with metal degradation processes [17-18].

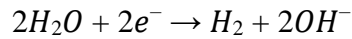
1.2.1 Corrosion Mechanism

Corrosion is an electrochemical reaction that occurs with metallic materials. The alloys commonly used as orthopedic implant materials are, typically, Ti-6Al-4V, CoCrMo and 316L stainless steel alloy, which are all demonstrated as corrosion-resistant materials. All these materials form a nanometer-scale layer of oxide film on their surface

to prevent the metals from acting as continuously active corrosion surfaces. The oxide film provides a kinetic barrier between the bulk material and aqueous phase that limits the rate of oxidation by slowing transport of ionic species from metal to solution. The thickness of the oxide film is between 2-5 nm in equilibrium condition but can be affected by many aspects, e.g., potential [19], solution, etc. The composition of the oxide film for different alloys is also variable. For Ti-6Al-4V, this oxide is mostly composed of TiO₂ while CoCrMo and 316L stainless steel alloy have chromium-based oxide.

As a bearing surface for many implant devices, especially THA, oxide film surfaces can provide a stable surface covering for the alloys. However, for many junctions, e.g., head-neck taper junction, oxide film can be disrupted by mechanical processes. Any time the oxide film is damaged or removed, the bare metal alloy will immediately react with the aqueous phase, which is body fluid, to generate a new passive oxide film and release metal ion at the same time prior to film reformation. This process is called repassivation, which only last for a few milliseconds. Corrosion is the combination of oxidation and reduction reactions or redox reactions, which lead to metal ion release or oxide formation and electron accumulation within the metal phase. Further on, these electrons, which under the bare metal surface, will react with water molecules and oxygen molecules to form hydroxide and hydrogen gas. These redox reactions can be explained using the following reactions:





The redox reaction can not only lead to ion release but also have strong connection with debris generation. Studies has shown that large amounts of Co ions were detected, and large Co/Cr ion ratio was observed in serum from patients who have CoCrMo alloy implant inside their body [20]. The disrupted oxide film could form into debris particles or react with molecules like phosphate to form metal-phosphates. These degradation products can move within the body and attach in tissue to initiate an adverse local tissue reaction [21].

1.2.2 Mechanical Assisted Corrosion (MAC)

Once the oxide forms on the metal surface, it acts as a kinetic barrier which limits further redox reactions. However, whenever the oxide is removed or disrupted mechanically, the underlying metal is re-exposed to solution, and repassivation occurs until fresh oxide film grows thick enough to dramatically slow the electrochemical circuit. This mechanically assisted corrosion (MAC) process is due to an interaction between mechanical and electrochemical factors leading to accelerated damage [22]. MAC happens at the interface of two phases and may damage both surfaces. Figure 1.2 demonstrates the process of MAC. Oxide film is abraded by an asperity (a small protrusion from the opposing surface), thus exposing the underlying fresh metal surface to the surrounding solution. Once the redox reaction is initiated, metal ions dissolve into solution and metal oxide formation begins. Both release free electrons which remain at the metal surface, where they attract water molecules and transfer negative charge to the

solution. This reaction could affect the solution chemistry and eventually cause a loss of bulk metal as it repeatedly occurs over time.

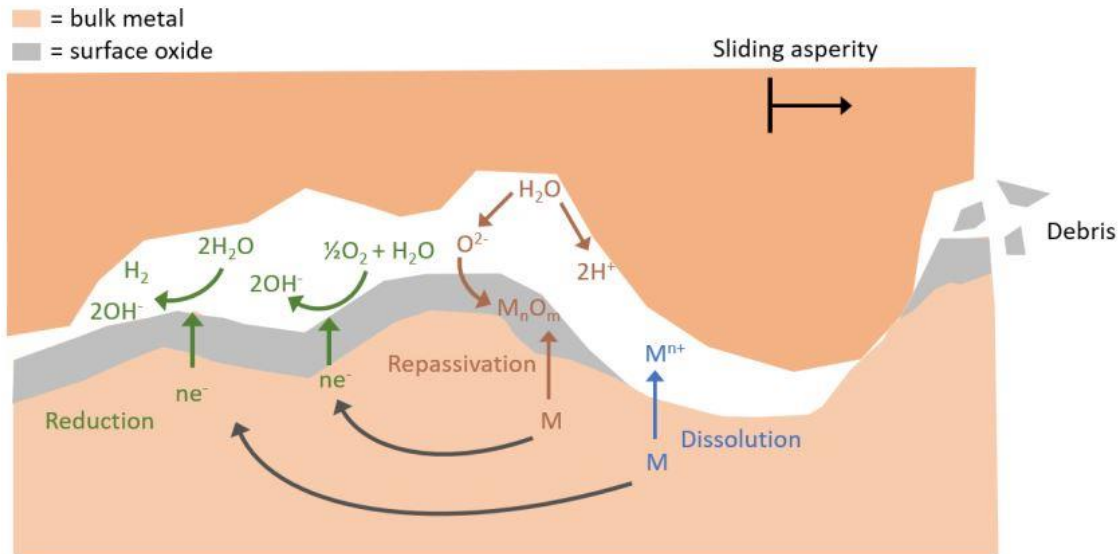


Fig. 1.2. Schematic showing MACC of a passive metal and the associated redox reactions. Abrasion by an asperity removes the metal oxide and initiate repassivation. [23]

When MAC occurs repeatedly in very small scale, e.g., micro-level, the corrosion process is defined as fretting corrosion. It consists of cyclic micro-motion, which is less than $100\ \mu\text{m}$, between two surfaces that disrupt the passive oxide film and accelerates corrosion. Asperities on both surfaces will abrade the surface oxide film, when fretting motion is initiated and it will give rise to a series of redox reactions due to abrasion of the two surfaces. The repassivation process, subjected to redox reactions, will shift the potential of the implant to more negative potentials and generate fretting-corrosion currents. The potential of oxide-covered surfaces is relatively stable if there is no fretting motion causing oxide disruption. The potential when no oxide disruption occurs is called the resting Open Circuit Potential (OCP) and it depends on the characteristics of the

metal itself, the oxide film and the reduction reactions present. When the oxide film is disrupted, oxide repassivation and metal ion release will generate significant drops in electrode potential as these burst reactions generate the accumulation of free electrons in the metal (lowering the potential) until reduction reactions can consume these electrons and depolarize the surface. Due to the asperity-like nature of the surface roughness, crevices exist in most metal-metal taper contact interfaces. Crevices are a small space that allows for a small amount of fluid to enter from the outside environment. Corrosion occurs within this space and is called crevice corrosion. Evidence of crevice corrosion occurs on metallic implant materials has been reported in many retrieval studies and has become a concern that may affect implant lifetime [24-25]. However, only limited *in-vitro* testing methods are developed to simulate crevice conditions [26], and there is a lack of demonstration of in vivo observed crevice corrosion processes *in vitro*. During MAC, the continuously repeated redox process consumes the free oxygen in the crevice. Because of the tiny space, oxygen concentration is very low. In this circumstance, oxidation rate is limited by oxygen, which allows metal ion concentrations to rise within the crevice. Metal ion then will react with nearby chloride ions to form metal-chlorides. Further, metal-chlorides can form metal hydroxide and hydrochloric acid with water molecules, eventually lowering the pH within the crevice environment. This process is considered as mechanically-assisted crevice corrosion (MACC). MACC requires that the metal oxide be abraded, and crevice geometry existence, which will restrict fresh media flushing into the space to provide enough oxygen species. So, cyclic surface abrasion like fretting corrosion could quickly create MACC conditions and it can be named as fretting

crevice corrosion. This process can cause implant failure by releasing metal ion species and debris particles, which has been documented in several studies [27-28].

1.3 MACC on Metallic Implant Materials

Clinical evidence of MACC on head-neck taper junctions began in the late 1980's. An increasing number of complications in patients who have metal-metal contact surfaces showed that corrosion products, e.g., oxide debris, existed in periprosthetic tissue and inflammation of the joint region was associated with this debris [29]. These products have been associated with a chronic inflammatory reaction. MACC can create a highly aggressive environment that increases the implant's electrochemical reactivity and may accelerate implant degradation. These adverse tissue reactions have been associated with pain, loosening, osteolysis, and fracture, which all lead to revision surgery to replace the dysfunctional implant devices [30-31].

Gilbert et al. first proposed the theory of MACC as the reason for *in-vivo* corrosion of the head-neck taper region for metal-on-metal contact interface and found evidence of fretting corrosion in metal head-neck junctions [32]. Another study confirmed that greater amounts of fretting corrosion damage in mixed metal couples (CoCrMo/Ti-6Al-4V) than similar materials combinations [33]. One of the popular methods for studying MACC is to retrieve the implant from patient and perform a series examinations and analyses, which is known as retrieval analysis. Retrieval analysis could help to determine the reasons for implant failure and complications. However, these studies are not sufficient to generate conclusions regarding of the impact on metal

damage. Reasons for the defects could be due to selection bias of each implants, or the inherent variability in surgical technique and even patient health history could affect implant behavior.

Instead of using retrieval studies alone to assess MACC on metallic implant devices, *in-vitro* testing methods provide more in-depth and systematic exploration of metal degradation and the factors that affect it. Such methods allow for any investigation into the performance of different materials under varied test conditions, which becomes an important part of pre-clinical study. The test method itself could be varied depending on the samples and other parameters. However, the general purpose should involve measuring and acquiring the correlated electrochemical and mechanical data at the same time. Typically, an *in vitro* testing method for MACC or more specifically, fretting corrosion, includes a metal sample, electrochemical chamber, and mechanical system, which can abrade surface oxide so as to create a corrosive environment. The mechanical system could be composed of displacement sensors to measure relative distance between samples, and load part that can apply constant load during testing and actuator that can provide cyclic movement in the micron range for abrasive conditions for one or more sample surfaces [34-35].

Usually a three-cell potentiostatic electrochemical setup is used for measuring current in the electrolyte. This setup is made by a working electrode (WE), which is the test sample itself, a reference electrode (RE), which usually use Ag/AgCl or SCE, and a counter electrode, which usually made by carbon, platinum or gold. In a potentiostatic experiment, the potential is held fixed in order to measure the currents. In other

experiments the potential is not held fixed but is allowed to vary with testing and currents can be measured between the abrading electrode and a second electrode on which the reduction reactions will predominantly take place.

The magnitude of the potential and current can reflect the extent of abrasion-repassivation process of oxide film. The rate of oxide repassivation can be quantified as current when fixed potential is applied to the system. The common electrochemical environment for measuring MACC for metallic material is under potentiostatic circumstance, where fixed potential is applied, and current is easy to characterize. Any time the working electrode (WE) is abraded, current transients will flow from the samples to the counter electrode as the oxide reforms. Ionic conduction through the electrolyte solution allows the current to pass from the counter to the working electrode, completing the circuit. One thing worth noticing about MACC measurement is that metal ion release exists during repassivation, which is also considered as part of the contribution to the current generation. However, current due to ion dissolution is typically much less than the current generated by oxide repassivation for these alloys and experimental conditions, and hard to be distinguished when the system is held at a fixed potential [36].

Other testing methods, which can reflect surface electrochemical properties, are also introduced to study MACC between different materials. Anodic polarization testing, cyclic voltammetry, and electrical impedance spectroscopy (EIS) are three most common techniques for analyzing electrochemical behavior of metallic materials. Anodic polarization test, which applies a slow scan of a range of potentials between working electrode and reference electrode and measures the current response [37]. It can

characterize different regions, including the active region, passive region and transpassive region, for any testing materials. Cyclic voltammetry is an electrochemical technique which measures the current that develops by cycling the potential of a working electrode and measuring the resulting current [38]. EIS is performed by applying a small sinusoidal voltage over a static voltage using a range of frequencies. The current response is then used to calculate the interface's impedance, which can be related to a resistive-capacitive circuit model to characterize its electrical properties [39]. Results from these tests can be used to characterize material's susceptibility to corrosion before and after MACC occurs, where damage region could exhibit different results compared with the rest of the area.

As one of the most representative modes of MACC, fretting corrosion has been studied over decades. *in vitro* testing methods have been developed to simulate the corrosion damage which may occur within human body, such as ball-on-platform and pin-on-disk etc. [40-41]. Among all of them, pin-on-disk (POD) testing method has been demonstrated as an effective way to characterize corrosion during fretting motion under various electrochemical and mechanical circumstances. This testing method usually involves a cone-shape pin with small amount of exposed area and a disk with known surface geometry. A constant force and periodical fretting motion, which is less than 100 μm with fixed frequency, is applied between two sample surfaces under constant potential. A variety of information can be obtained during this test, including sliding displacement, frictional force of the pin and fretting current. Since the general goal of this dissertation is to study the fundamental mechanism of fretting crevice corrosion between different implant materials, pin-on-disk testing method would become a major technique

of the studies presented here. It is a very useful technique when studying fretting crevice corrosion at the materials-level. Previously developed American Society for Testing and Materials (ASTM) guidelines for modular implant interfaces will also be applied to assess fretting corrosion resistance of implant devices, especially for hip implants [42]. This method involves seating the femoral head onto the femoral stem component, submerging the implant in solution, and applying an incremental cyclic load to the implant at fixed frequency after an initial loading period. A potentiostat with a three-electrode system, which same as is used in POD testing, holds the setup at a fixed potential and measures current during the test. This guideline, and other similar methods, have been used to investigate fretting corrosion behavior of modular implant devices regarding of different circumstances.

1.4 Challenges

Even though corrosion of metallic implants has been studied over decades, there are still many challenges that are not well-understood or explored, e.g., clinical observation, materials selection and model prediction etc. The studies included in this dissertation will fill some of the gaps and provide new insight for future studies of metallic implant corrosion.

Retrieval studies have shown evidence of fretting corrosion at head-neck taper junctions, which could cause ion dissolution. Clinical research shows that Cobalt (Co) and Chromium (Cr) ion was detected in THA patients' blood samples, where Co has a much higher ion concentration than Cr ion [43]. Similarly, chromium oxide and

phosphate solid debris are formed in vivo and typically gets retained within the taper crevice, lodged in the periprosthetic tissue, or transported systemically [44]. Thus, the ion release process comes along with debris generation during fretting corrosion. So far, there is no experimental evidence to demonstrate both occurs simultaneously or how the partitioning between cobalt ions and chromium solid produces occur.

To better understand the mechanisms of fretting corrosion and explore its potential mechanical or electrochemical factors, many theoretical models or analysis methods have been developed. For example, finite element analysis (FEA) has been adapted to simulate fretting corrosion at alloy interface [45-46]. Fallahnezhad et al., developed an algorithm that can predict the repassivated oxide volume based on some conditions. This model can also simulate the fretting corrosion consequence for various sliding regime. However, one of the limitations of current FEA models is that the model does not consider surface resistive and capacitive properties could affect oxide repassivation on the contact surface.

Since fretting crevice corrosion, which is the representative of MACC, is a combination of fretting corrosion and crevice corrosion, there could be other potential unexplored phenomena that may exist between these two types of corrosion. Crevice corrosion usually happens within a tiny space without mechanical influence. However, no studies have demonstrated whether mechanical factors could trigger crevice corrosion which then continues even in the absence of fretting. Some clinical studies show that localized corrosion damage is observed in metallic implant for TKA [47]. The damage is not due to typical fretting corrosion but more like crevice corrosion or pitting corrosion.

Exploring new corrosion mechanism that are affected by fretting corrosion could provide a potential explanation for corrosion damage observed in retrieval studies that remain unexplained (e.g., selective dissolution, grain boundary corrosion, etching, etc.).

In order to protect implants from MACC in THA, ceramic materials have also been chosen to replace metallic materials due to their non-conductivity and excellent biocompatibility. Common ceramic materials used in THA are Alumina and zirconia-toughened alumina since they have shown biocompatibility and corrosion resistance in taper junction [48-49]. Recently, silicon nitride (Si_3N_4) has been drawing more attention for their clinical application, including cervical and thoracolumbar spine fusion. However, most of the research so far on silicon nitride has focused on the bearing properties rather than fretting corrosion performance against the commonly used titanium alloy, e.g., Ti-6Al-4V. Filling this gap could provide supportive evidence for surgeons to choose more suitable materials in THA.

1.5 Goals

The goal of this dissertation is to increase our current understanding of the fundamentals of fretting crevice corrosion of orthopedic implant materials. More specifically, works in this study can provide more information to fill the gaps that were mentioned in challenge section. To date, we have shown how metallic implant materials react under different circumstance *in vitro* and develop strong relationship between theoretical aspect with experimental aspect. Continued research related to each aim will provide additional data to assist people in understand the basic mechanism of fretting

crevice corrosion. We expect to have more understanding of the interactions and factors that are involved during these electrochemical processes and use them in the future to design orthopedic implants which have better corrosion resistance. This work is significant to the field of orthopedic implants because it looks to understand fretting corrosion of metallic implant materials and may, in the long term, lead to smarter biomedical alloys development and dynamic implant coatings that have greater corrosion resistance. This could ultimately lead to more predictable implant lifetimes with an increase in efficiency and safety.

2. Aims and Hypotheses

A series of experiments was performed to provide information and evidence of several aspects of the fretting crevice corrosion behavior of metallic implant materials and devices including debris generation, model development, electrochemical reactions and materials combination. We plan on investigating the fretting corrosion behavior of different materials in various experimental conditions and establishing a theoretical model of the process to predict the electrochemical changes during fretting corrosion. Each goal, specific aim, and hypothesis is outlined below.

2.1 In vitro fretting crevice corrosion damage of CoCrMo alloys in phosphate buffered saline: debris generation, chemistry and distribution

Goals: To demonstrate the debris generation processes and to show that Cr-phosphate rich solid corrosion debris and preferential Co-ion release into solution was the result of fretting crevice corrosion.

Specific Aim: A custom-made “two-dimensional” pin-on-disk fretting test system was used to generate debris. The whole system was placed under a digital optical microscope, which allowed the user to observe debris generation directly at the contact region. The test was performed after a certain amount time and the debris was isolated from solution using a syringe and was analyzed for morphology and chemistry. Surface characterization using several analytical surface techniques (SEM/EDS, AFM, XPS) after testing and solution chemistry measurement (using ICP-MS) was also included in this study.

Hypothesis: The hypothesis is that the debris generated from fretting crevice corrosion of CoCrMo alloy is partitioned between ionic and oxide chemistries, as observed in vivo, where Co ions predominate in solution, and solid Cr-oxides and phosphates are formed and adhere to the surface in a location dependent way.

2.2 A metallic biomaterial tribocorrosion model linking fretting mechanics, currents, and potentials: Model development and experimental comparison

Goal: The goal of this study is to present a coupled set of heredity integrals to describe the abrasion-current-impedance-voltage behavior during tribocorrosion. This model will link the abrasion mechanics with the fretting currents and also to link currents to the electrode potentials over time for any arbitrary abrasion-time process.

Specific Aim: In this test, the pin and disk sample comprised one electrode, while a second electrode, also made from CoCrMo alloy was connected to the pin and disk through a zero-resistance ammeter. A freely corroding condition was established and monitored. The frequency of fretting sliding was varied, and the fretting currents and electrode potentials was captured in each test for comparison. Comparisons were made between the experimental potential-time and current-time response for each frequency and the model prediction based on the measured sliding displacement time behavior and parameters related to the contact mechanics such as hardness and normal load, and impedance values.

Hypothesis: The hypothesis of this aim is that this model can well-predict the potential and current behavior based on the pre-set parameters. The model will be compared to experimentally obtained fretting currents and potential shifts to assess its capabilities.

2.3 Fretting initiated crevice corrosion of 316LVM stainless steel in physiological phosphate buffered saline: potential and cycles to initiation

Goal: The goal of this study is to investigate fretting initiated-crevice corrosion (FICC) behavior of stainless steel in physiologically representative saline solution in an *in vitro* pin-on-disk fretting corrosion model.

Specific Aim: The material used in these experiments was 316 L Stainless Steel (ASTM F138) alloy pins and disks. Fretting corrosion tests were conducted using a pin-on-disk system. All electrochemical measurements were obtained through a potentiostat. The potential of the working electrode was varied from -700 mV vs Ag/AgCl to 250 mV vs Ag/AgCl with an increment of +50 mV or 100 mV between each voltage. Damage induced at the fretting interface was investigated using several analytical surface techniques (SEM/EDS, AFM, XPS) after testing.

Hypothesis: The hypothesis is that FICC requires the existence of a crevice and may be affected by the electrode potential. Also, this phenomenon can develop easily with just a few cycles of fretting motion.

2.4 Fretting corrosion of Si₃N₄ vs CoCrMo femoral heads on Ti-6Al-V trunnions

Goal: The goal of this aim is to measure fretting corrosion performance of Si_3N_4 heads/Ti-6Al-4V modular tapers for total hip replacements *in vitro* and compare their behavior to standard CoCrMo heads/Ti-6Al-4V modular tapers tested under identical conditions.

Specific Aim: The test group consisted of samples where the trunnion coupon was a cylindrical sample made from Ti-6Al-4V rod with a trunnion machined into it. The head component was made from Si_3N_4 or CoCrMo with identical taper features with commercial quality taper surfaces. Seating tests were initiated at beginning and followed by incremental cyclic fretting corrosion (ICFC) tests, where cyclic loads were applied vertically to the head of the head-neck taper construct. Immediately after ICFC testing, a long-term fretting corrosion test was performed, which total number of cyclic loading reached to 1 million times. At the end of the one million cycle test, the samples will be subjected to a pull-off test where the head is distracted from the trunnion in a static mechanical test. After disassembly, the taper surfaces will be imaged using optical and electron microscopy methods. EDS analysis will be carried out to observe material transfer. Fretting current and mechanical signal was captured during the whole process to assess fretting crevice corrosion damage between head-neck taper junction.

Hypothesis: The hypothesis is that Si_3N_4 will provide better corrosion resistance compare to CoCrMo alloy when both are tested against Ti-6Al-4V.

3. *In vitro* Fretting Crevice Corrosion Damage of CoCrMo alloys in Phosphate Buffered Saline: Debris Generation, Chemistry and Distribution [27]

3.1 Introduction

Metallic orthopedic devices, such as joint replacements, spinal screws, and bone plates, have been widely used for decades. Many metallic biomaterials like stainless steel (316LSS), titanium-based alloy (Ti-6Al-4V) and cobalt-chromium alloy (CoCrMo) have been documented as suitable implant materials. However, implant material failures have been reported *in vivo* and many of them occur prior to the ideal lifetime of implant systems [50–53]. Many retrieved implants show evidence of corrosion and wear phenomena [54].

Fretting corrosion, one form of mechanically assisted corrosion, consists of cyclic relative motion between two surfaces of less than 100 μm and may be present in head-neck, neck-stem, and acetabular taper junctions in total hip replacements [55]. In order to have a better understanding of the failure mechanisms of metallic implants, test systems and mathematical theory have been established to help understand fretting corrosion [56–67]. However, most of these test systems focus on the mechanical aspects of wear, such as friction force and energy loss and pay less attention to the details of fretting corrosion, like debris generation, electrochemical processes of ion release and changing of electrochemical parameters (e.g., voltage and fretting current). In addition, there have been no direct observational tests of *in vitro* fretting corrosion debris generation

previously published that seeks to correlate the debris composition and generation processes to *in vivo* observed results, particularly as they relate to the nature of the solid debris as well as the chemical distribution of the ionic debris generated. It is useful to combine electrochemical and mechanical testing with visualization to better understand the fretting corrosion process, especially in debris generation. Visualization of the fretting corrosion process using optical microscopy methods provides direct information about fretting debris generation, deposition and propagation processes.

As one of the most common metallic biomaterials used in total hip replacement, CoCrMo alloy (ASTM F-75, ASTM F-1537) has been used as femoral head for decades due to its ideal biocompatibility and wear resistance [68–70]. However, the degradation products that come from CoCrMo fretting corrosion processes have been implicated to cause clinical concerns [77]. In particular, it has been shown that when modular taper-based mechanically assisted corrosion processes occur, two unique aspects of the degradation are observed *in vivo*. First is the generation of chromium phosphate particles that have been identified in the periprosthetic tissues surrounding hip implants with corroded modular tapers [72]. Second is the relatively high ratio of cobalt to chromium observed in patients' blood serum with corroding modular tapers [73–75]. The reasons for these observations and the mechanisms for their generation have not been studied previously in an *in vitro* test to determine if this is a physicochemical consequence of the fretting crevice corrosion mechanism or has other biologically-based reasons. Most wear debris or particles used in biological response studies come from wear simulators, which generate particles using large scale sliding motions and do not contain crevice conditions.

Fretting crevice corrosion is another way to generate debris which has not been well developed, characterized or utilized in such studies.

In this study, a 2-dimensional (2D) fretting corrosion test system was developed to perform direct visualization of the fretting corrosion process and debris generation [76]. Thin-sectioned CoCrMo alloy pin and disk samples (about 500 μm thick) are fixed between two glass slides between which a small volume (less than 2 ml) of solution was added to simulate fretting corrosion conditions and to directly observe debris generation mechanisms. The transparent glass above and below the sample allows the operator to use a microscope to observe and record the details of fretting corrosion at the interface during the whole process. It is hypothesized that a simple fretting corrosion pin-on-disk test system and phosphate buffered saline solution can generate similar fretting corrosion degradation products (CrPO_4 debris and high Co ion solutions) as seen in *in vivo* when CoCrMo alloy pin and disk are tested. The goal of this work is to demonstrate the debris generation processes and to show that Cr-phosphate rich solid corrosion debris and preferential Co-ion release into solution is the result of MAC in a fretting crevice environment. This work will also document the debris accumulation process and morphology and chemistry of the solid debris generated within fretting crevice regions. This combined set of capabilities enables us to explore a range of research questions associated with the process of fretting corrosion.

3.2 System Development

The test system (Fig. 3.1a) was custom built and consists of a customized load cell, which includes a double-cantilever design with an aluminum mount, two brass cantilevers, a linear variable differential transformer (LVDT) (DC 750-50, Macro Sensors, Pennsauken Township, NJ, US) and a brass rod support. This load cell had a spring-like system with lateral rigidity to achieve its function of applying a controlled normal load and an ability to slide laterally while measuring lateral forces. The two cantilevers bend when pin and disk are in contact and apply a known load between them. Lateral stiffness of the cantilevers provides for an ability to impart fretting displacements. Fretting motion was induced by a saw-tooth voltage waveform applied to a piezoelectric actuator (Burleigh, Queensland, Australia), which was connected to an amplifier (PZ-300M, Burleigh, Queensland, Australia) and a function generator (FG-8002, EZ Digital, Melrose, MA, US). Three mechanical parameters: normal load, friction force, and relative displacement was measured separately. Normal load was measured by the described load cell converting LVDT displacements into normal load. Frictional force was obtained through a non-contact differential variable reluctance transducer (DVRT) (SN3327, Micro-Epsilon, Raleigh, NC, US). This sensor measured the lateral deflection of the pin, which changed with fretting motion and the lateral force was proportional to the measured lateral pin deflection. True pin-disk relative displacement was determined by subtracting pin deflection from stage movement measured by a second LVDT sensor. The raw data captured by computer data acquisition methods was converted to force or displacement based on the manual calibration of each sensor using either known weights or precise displacement calipers. The electrochemical circuit is shown in Fig. 3.1b, which

represents the pin & disk contact region in Fig. 3.1b. Here, the thin-sectioned disk and pin, both about 500 μm in thickness, are the working electrodes and solution was injected between the two glass slides, both of which were connected to the disk sample. The solution was held in place by surface tension and fully immersed the working, reference and counter electrodes in a small volume of solution (about 1.5 ml). The load was applied along with the negative x-axis direction and the system performed back-and-forth fretting movement along y-axis. The observation direction was through z-axis, which focused on the contact interface. The wire reference (Ag/AgCl wire) and counter (Au wire) electrodes were positioned within the solution. Because the disk-pin contact region was near the edge of the glass slides, solution was able to fully cover the contact region. Only the contact region was exposed, the rest of working electrode surface area was covered by an isolating lacquer material. A metal screw penetrated through the top of a plastic holder and contacted with the disk sample to ensure electrical connection outside of the solution. A custom written LabVIEW (National Instrument, Austin, TX, US) program was developed to capture and graph the data.

3.3 Materials and Methods

CoCrMo alloy (ASTM F1537, low carbon, see Table 3.1) slices and cone-shaped flat-bottomed pins (interfacing surface area nominally: 0.002 cm^2 to 0.009 cm^2) were tested in each test round.

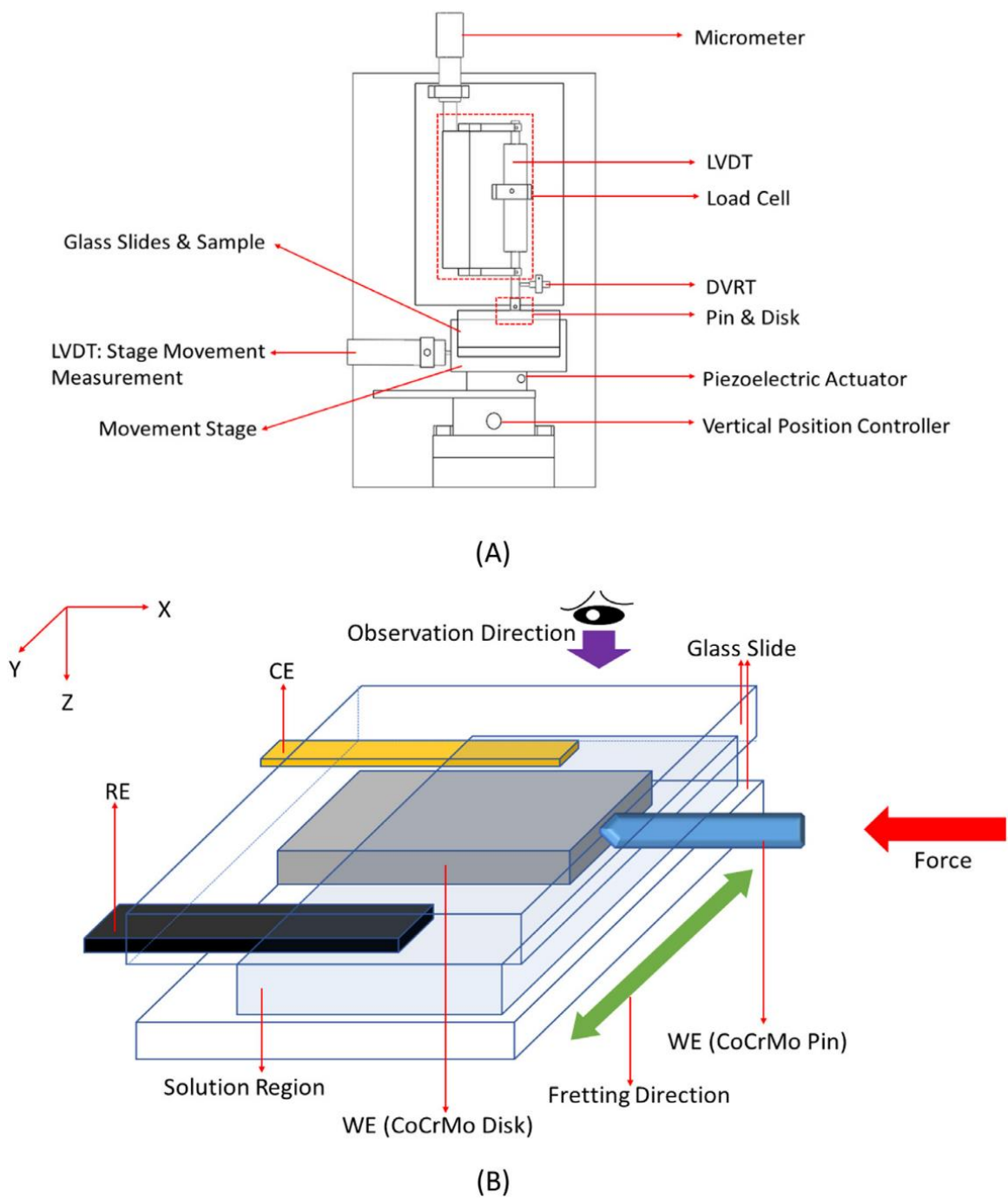


Fig. 3.1. (A) schematic of the fretting corrosion test system. Note that pin and disk are recognized by smaller rectangle and will be detailed in the electrochemical section below. 3D schematic (B) of electrochemical part. Note that WE are the working electrode, RE stands for reference, CE stands for counter electrode.

Table 3.1. Composition of CoCrMo [77]

Co	Cr	Mo	Ni	Fe	Si	Mn	N	C
Bal.	26.0-30.0	5.0-7.0	<1.0	<0.75	<1.0	<1.0	<0.25	<0.14

The disk slice was cut using a low-speed diamond saw in a rectangular shape (200–500 μm thick). Each pin and disk slices were polished on the thin section by hand to 600 grit using emery paper under flowing water until the scratches were aligned yielding an approximation of a ground finished surface as seen *in vivo*. After polishing, the samples were cleaned in ethanol and deionized water to remove any possible remaining particles from the emery paper. In order to have a consistent electrochemical environment, a relatively constant area, approximately 0.0045 cm^2 (nominally: 0.003 to 0.006 cm^2), was exposed while the rest of the surface was covered by an electrically insulating lacquer material. Three trials ($n = 3$) were performed for each test. The Ag/AgCl reference electrode used in this study was a chlorided silver wire that was subjected to a 2 s open flame treatment followed by a 10% bleach solution, dried and then immersed in the test solution.

3.3.1 Observation of debris generation

In order to visualize debris generation during fretting corrosion, the whole system was combined with a digital microscope (KH-870, Hirox, Tokyo, Japan). Both the pin and disk were immersed in phosphate buffered saline (PBS) (P3813, 0.135 M NaCl, 0.0027 M KCl, 0.01 M Na_2HPO_4 and 0.002 M KH_2PO_4 , SigmaAldrich, St. Louis, MO, US) solution for 2200s at room temperature (RT) before each test. A three electrode potentiostatic test (-100 mV vs Ag/AgCl), was controlled by a potentiostat (Model

263, EG&G, Princeton Applied Research, Oak Ridge, TN, USA) during fretting. In order to have a better debris generation rate, 5 Hz and 0.7 N was used with 65 μm sliding amplitude. A 350x magnification was used to provide high resolution imaging during fretting. Videos, which lasted for 5 s, were first recorded at 12 min after the test started and again recorded at 20 min, 30 min, 60 min, and 120 min.

3.3.2 Debris and surface characterization

In order to generate fretting debris to obtain composition, morphology and deposition characteristics, fretting tests were performed at -100 mV vs Ag/AgCl, 0.5 N normal load, 65 μm displacement at 3 Hz for 10 h were performed. This potential was chosen because it is at, or near, the non-mechanically-abraded resting Open Circuit Potential for this alloy in PBS. The load and displacement conditions were selected for optimized conditions for the test system (i.e., prevent sticking) and to develop representative contact stresses within the contact region as well as sliding distances that are seen in retrieved modular taper junctions. Three Hertz was selected to provide sufficient cycles within 10 h, but to also keep within a frequency where full oxide film repassivation can occur with each cycle of sliding. After each trial, solution was extracted from the fretting region and stored in a test tube. Both pin and disk were dried out in room temperature and then subject to a digital optical microscopy (Keyence VK-8700, Itasca, IL, US) for initial observation. Then the disk was imaged using a scanning electron microscopy (SEM) (Hitachi S-3700 N, Tokyo, Japan) equipped with energy dispersive X-ray spectrometer (EDS) (Oxford Instruments X-Max, United Kingdom) to firstly image the overall surface topography. Debris were partially removed using

adhesive tape so the backside of debris and the covered surface could be analyzed. Both tape and the sample were re-examined using the same SEM & EDS system to image debris, the fretted surface and to determine the chemical composition of solid debris.

Post-test disk samples were investigated using an X-ray photoelectron spectroscopy (XPS) system. It was conducted on a Quantum 2000 Scanning ESCA (Electron Spectroscopy for Chemical Analysis) microscopy (Physical Electronics, Chanhassen, MN, US) system, using Al radiation $K\alpha=1486.6$ eV with passing energy of 117.40 eV, and 50 μm probe size. The takeoff angle between the sample surface and analyzer was 45° . Sputter Depth Profile mode were conducted on the fretted area and unfretted area on CoCrMo surfaces. Depth profile results provide information about element depth profiles from the surface. Surface argon sputtering of CoCrMo samples was conducted for 30 cycles at intervals of 0.3 min, which led to a total sputter depth of 7.5 nm (0.25 nm at each interval). Analysis of XPS spectra was performed using the MultiPark software (Physical Electronics, Chanhassen, MN, USA). Atomic concentration of O1s, P2p, Cr2p, Co2p, Mo3d peaks were plotted versus etch time/depth and shift of binding energy of each peak at different depth was analyzed. Both regions where fretting contact occurred and regions outside of the fretting zone were analyzed.

The surfaces of disks after fretting corrosion tests were also imaged by contact mode Atomic Force Microscopy (Dimension ICON AFM, Brukers, Billerica, MA, US), to investigate the nanometer scale topography of fretted regions and regions immediately adjacent to the fretting site. Wear-resistant diamond-coated AFM probe (NMTC,

Brukers, US) (Spring constant 350 N/m) was used for imaging the surface. Deflection sensitivity of the probe was 84.95 nm/V.

The ionic concentrations of the three major metallic elements: cobalt (Co), chromium (Cr) and molybdenum (Mo) were measured in the solution using inductively coupled plasma mass spectrometry (ICP-MS) (ICAP RQ, ThermoFisher Scientific, Waltham, MA, US). This equipment can detect metals and several non-metals in liquid samples at very low concentrations. Since the solution did not contain any organic or cellular tissue, samples for ion measurement were prepared following a similar protocol which was reported in the literature [78]. Samples were allowed to settle for 30 min and centrifuged at 15,000 g for 10 min at 20 °C. Then the supernatant was poured off and diluted 10-fold with deionized water. The mixture was then measured in the ICP-MS. Both debris and ion tests were repeated a minimum of three times for each.

3.3.4 Statics analysis

Statistical analysis of the solution ion results was carried out using ANOVA and Tukey post-hoc tests. The critical value p is equal to 0.05 ($p = 0.05$) to determine significant differences between or within each group.

3.4 Results

3.4.1 Observation of debris generation

Video microscopy of the fretting corrosion process (Fig. 3.2, images at various time points from 12 min to 120 min) captured the development and extrusion of debris from the interface. The pin (dark, on left) and disk (bright, right) moved vertically in the

image as the microscope looks down from above. The interface-generated debris started as early as 12 min and continued over the 120 min test. Debris first showed up at the fretting interface and continued to develop with time. After 120 min newer-formed debris pushed the older debris to the peripheral area. This led to a phenomenon where the outer layer of debris was pushed away from the center and led to some of the debris becoming disconnected from the original generating area.

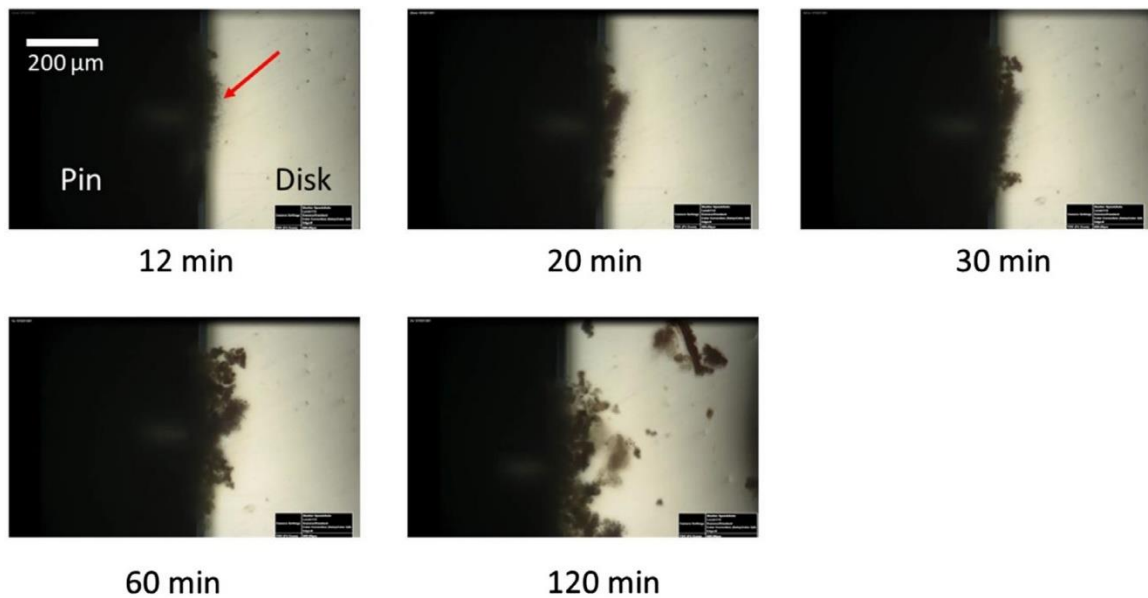


Fig. 3.2. Digital microscope image of debris generation from CoCrMo pin and disk at different time. Note that visible debris first showed up in 12 min after test begin. Arrow indicates debris extruding from the interface which increases in quantity with time.

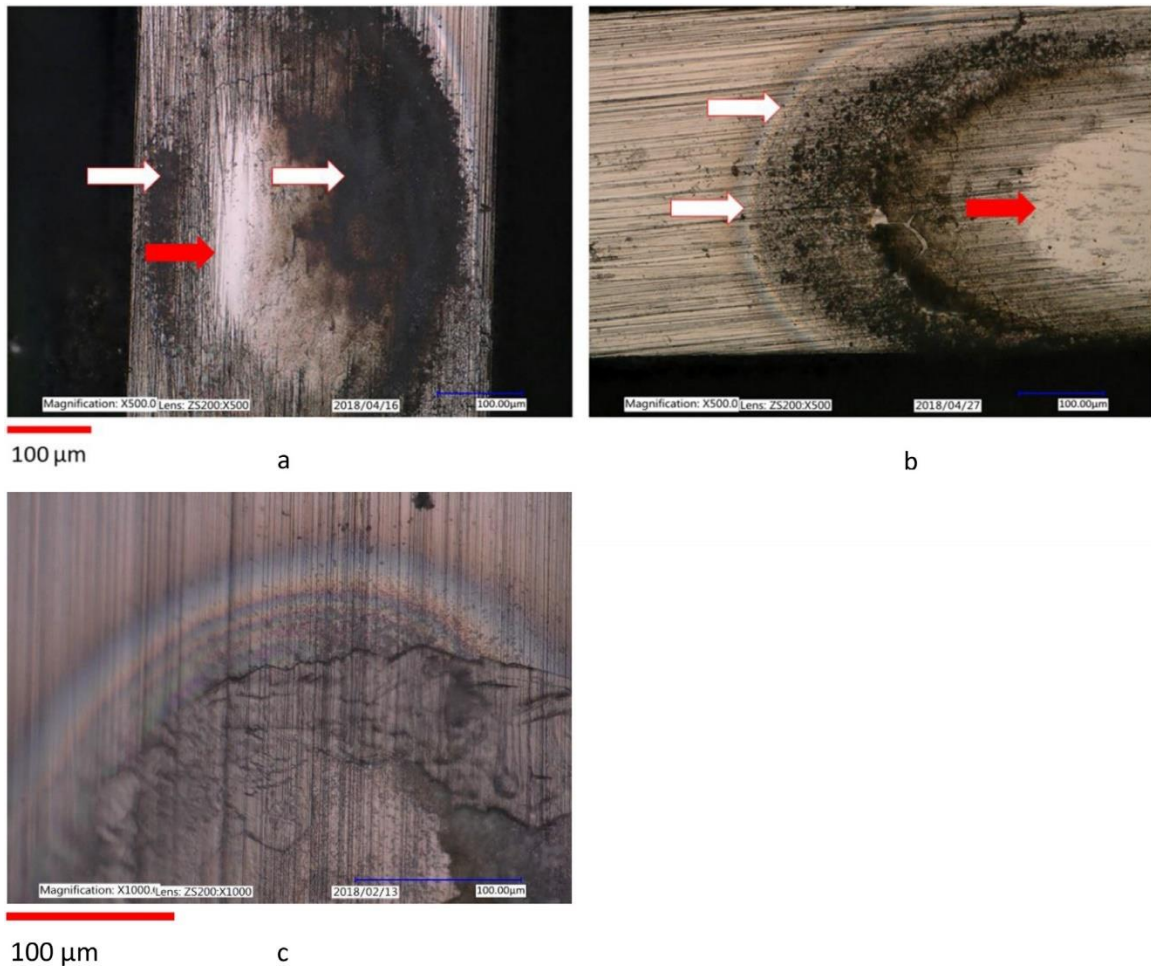


Fig. 3.3. (a) Optical micrograph of the fretted surface covered by debris. (b) A colored halo region was observed around the debris region. (c) A higher magnification optical image of the rainbow area. Red arrows (a and b) point to the contact zone between pin and disk, while the white arrows point to generated debris. Note that a and b have same scale. (For interpretation of the references to color in this figure legend, the reader is referred to the web version of this article.)

Digital optical micrographs of CoCrMo disk samples (Fig. 3.3a and 3.3b) were taken after 10 h of fretting corrosion, where solution was extracted for further analysis. Evidence of surface wear (bright burnished regions, red arrows) and debris generation (dark regions, white arrows) can be seen in these images. The bright burnished contact

regions were surrounded by a debris field that outlined the outer dimensions of the pin. Only a small portion of the nominal pin area actually made contact with the disk. The remaining region was a crevice geometry that provided space for fluid and for debris accumulation. Virtually all of the debris generated remained within the fretting crevice region as only a few visible debris particles were seen in the solutions subsequently collected from these tests. It was typical that a halo of debris and discoloration was observed at outer layer of debris which coincides with the transition from under the pin area to outside. The colored surfaces (Fig. 3.3b) associated with the halos are regions where corrosion products adsorbed to the surface of the alloy at the crevice-to-outside junction region in a very thin layer. A rainbow area associated with the perimeter of the debris field can be seen in Fig. 3.3c. The repeating fringe color pattern indicates a progression of thickness of the corrosion-deposited layer from the thinnest outside toward thicker layers as one moves inward. This occurs at the edge of the pin contact region with the disk.

3.4.2 Debris characterization

Scanning electron microscopy (SEM) images (Fig. 3.4) were taken of selected fretted surfaces as well as from the debris that had been adhered to the disk surface after testing. Fig. 3.4A and 3.4B shows the same sample before (Fig. 3.4A) and after (Fig. 3.4B) partial removal of the debris from the surface with tape. These images (both backscattered electron images) show the overall pin geometry, where the actual contact took place (bright region in Fig. 3.4A), which only comprised about 20 to 50% of the nominal contact region, and the accumulated fretting corrosion debris field within the

crevice. Even after partial debris removal, some adhered debris remained (Fig. 3.4B). Fig. 3.4C is a backscattered electron micrograph of the CoCrMo fretting contact surface after fretting against the CoCrMo pin. Evidence of burnishing (plastic deformation) and sliding can be seen. Also, some of the individual grains of the microstructure can be seen in this image within the fretting contact region. The surface is, for the most part, very smooth and shows little evidence of particulate debris. Fig. 3.4D and E is backscattered electron micrographs of the debris (Top side of the debris: Fig. 3.4D, and bottom side, Fig. 3.4E) to reveal the nature of the debris accumulated process and structure. These debris formed a dry lake-bed appearance that is likely due to the process of accumulation taking place and not from dehydration after testing, (Fig. 3.4D). This was confirmed by imaging the debris field in the digital optical microscope after fretting corrosion while still immersed in the test solution and the plate-like dry lake-bed appearance was seen (data not shown). The debris also formed an integral interface on the backside (Fig. 3.4E) with the metal substrate as can be seen by the imprinted polishing scratches on the surface of the debris. This indicates that the debris was compacted into the surface by the fretting corrosion process. There are almost no bright metallic particles seen within these images of the debris which implies that almost all of the metallic fretting corrosion debris are subsequently converted entirely into non-metallic oxides and phosphates over time of fretting corrosion. Fig. 3.4F shows an EDS spectrum with a backscattered SEM micrograph of the debris. Chemical analysis shows the presence of Cr, P, O with only small amount of Mo, Co, and salts. This indicates that the principal chemistry is one of phosphates and oxides of chromium being present in the debris.

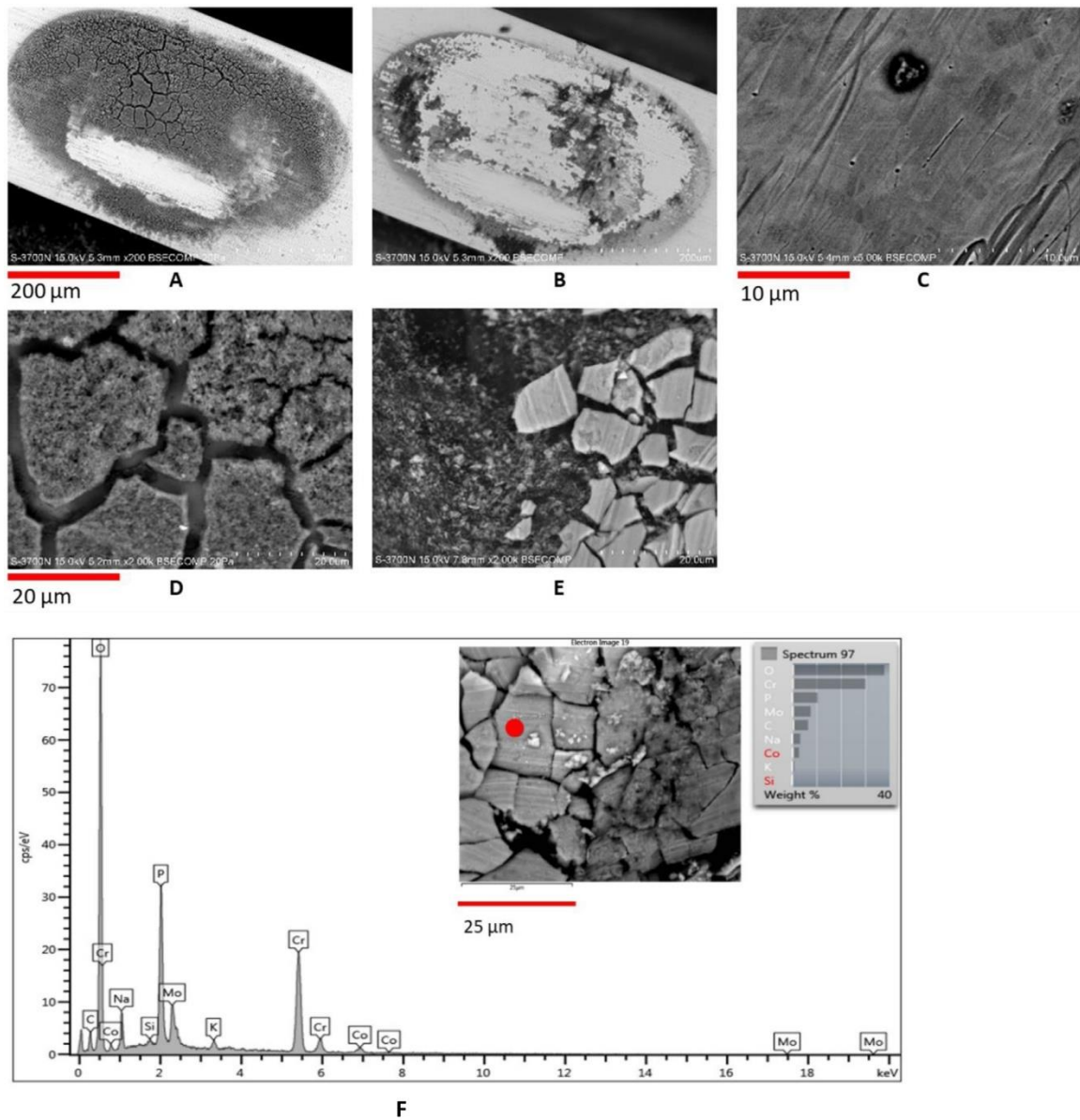


Fig. 3.4. SEM pictures of sample surface and debris. (A) and (B) were taken before and after debris was removed. (C) shows pitting corrosion was found in contact region. (D) and (E) are debris outlook which were taken from top and bottom. (F) is the EDS result of debris characterization. Note that A, B and D, E have the same scale.

Energy dispersive X-ray mapping results (Fig. 3.5) present an assessment of the composition of the debris deposited during fretting corrosion. The debris appears to be

entirely made from reacted metal degradation products comprised primarily of Cr-phosphate/oxide and Mo-phosphate/oxide. No metallic particles were observed in this solid debris. The debris filled the crevice space between pin and disk not in direct contact. Optically, the debris had a green appearance similar to that seen in retrieved tissue samples containing Cr-phosphate. There is a notable absence of Co from the solid corrosion debris and is only evident from the alloy itself.

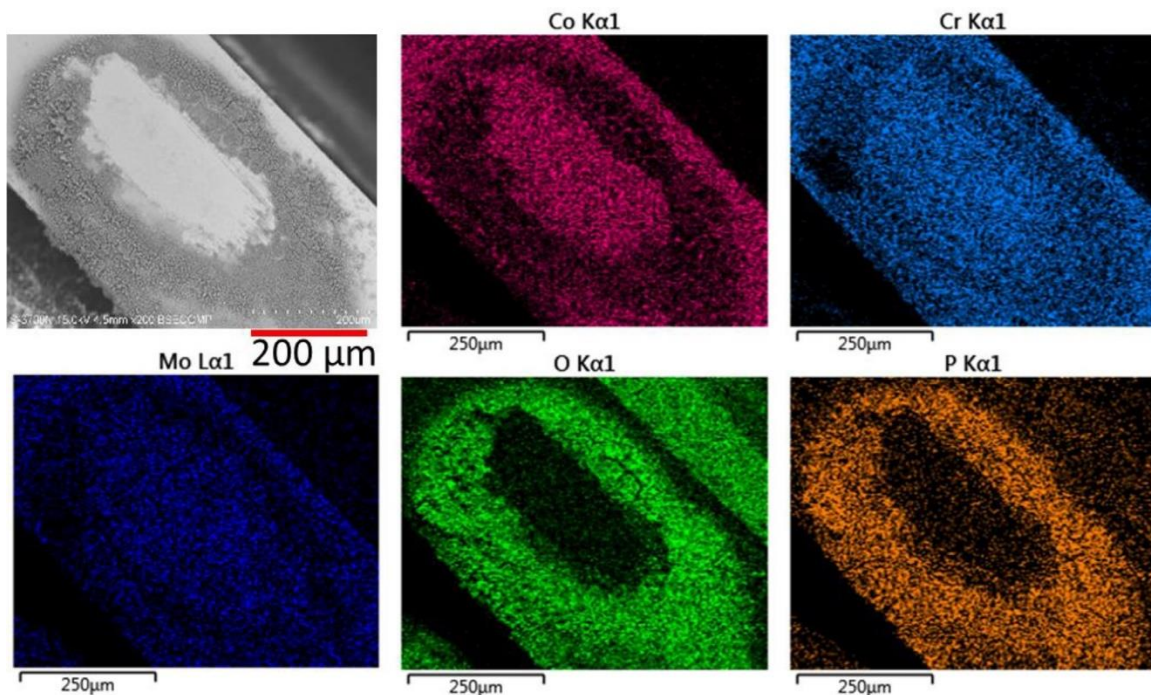


Fig. 3.5. EDS mapping result of fretting surface. Note that debris region rich in chromium (Cr), oxygen (O) and phosphate (P) but contact region reveal original elemental composition of CoCrMo alloy.

XPS results (Fig. 3.6) show the sputter depth concentration profiles for a fretted (Fig. 3.6a) and unfretted (Fig. 3.6b) regions of the alloy surface for O 1s, P 2p, Cr 2p, Co 2p and Mo 3d. A decrease of O1s concentration with depth into the sample was observed with high oxygen levels present in the fretted area compared to the unfretted area. The

individual XPS spectra for Cr (Fig. 3.6c and 3.6d) and Co (Fig. 3.6e and 3.6f) for fretted and unfretted regions are also presented. About 50% decrease of O1s concentrations occurs with 2 nm in both cases. The fretted area exhibited a thicker region where the O1s concentration remained well above the 5% level throughout the sputtering time, while the O1s concentration on the unfretted area fell to below 5% after 4 nm depth. Co was the dominate element after 1 nm depth. It reached to above 50% in both cases. However, Co 2p concentration in the fretted area was slightly lower than that of the unfretted area reflecting small losses of Co from the near surface region. Cr 2p, Mo 3d show similar concentration vs depth profile with small variation with depth for fretted and unfretted areas. Only small amount (within 5%) of P 2p was observed in both cases although the fretted area exhibited slightly stronger signal. A shift in binding energy of Cr 2p from higher energy states (Cr_2O_3 and $\text{Cr}(\text{OH})_3$ to lower state (metallic Cr), started from the second layer in both cases, was observed. However, the gradual shift stopped after the fifth layer on the fretted area case while it ended on the third layer for unfretted area, indicating difference in Cr depth profile was caused by fretting corrosion. No shifts of Co 2p peaks as depth increases were observed in both situations (Fig. 3.6e and 3.6f).

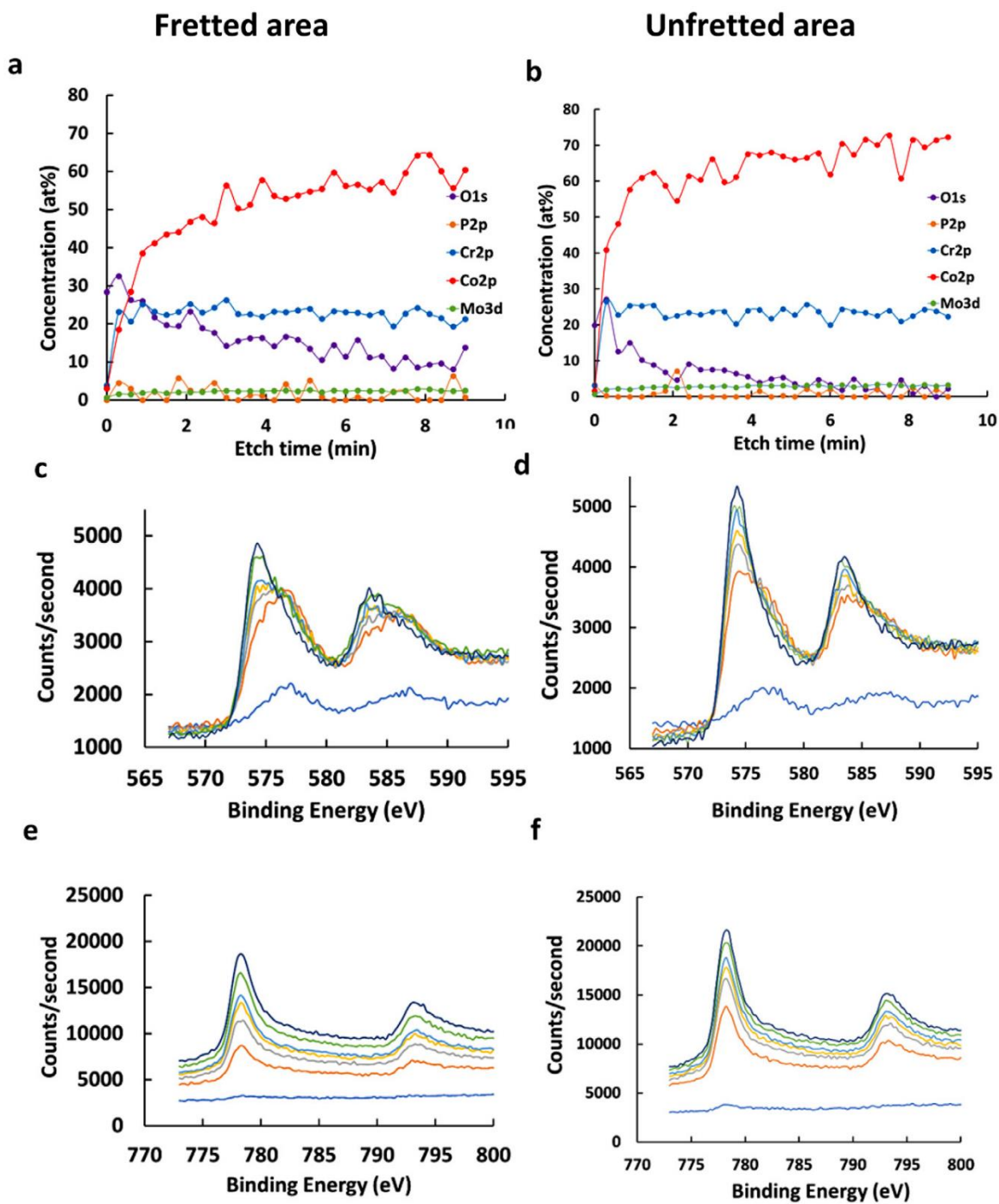


Fig. 3.6. a,b) show atomic concentration variation; intensity and binding energy of Cr2p (c, d) and Co2p (e, f) peaks at different depth on fretted and unfretted areas. (a, c, e for fretted area; b, d, f for unfretted area).

Fig. 3.7a and b shows AFM contact mode images (30 μm x 30 μm) of the CoCrMo surface at the boundary between the debris accumulated area and surface outside of fretted corrosion affected zone. Debris, ranging from sub-micrometer to 5 μm , appears in dome-like shapes and accumulated and aggregated, forming different debris layers. Fig. 3.7c and d shows height and deflection images that reveal possible grain boundary dissolution of CoCrMo alloy surface around the debris-accumulated region just outside of the fretting contact zone (but still within the crevice). The observation could also be due to the dry lake-bed effect of debris, mentioned earlier, since the observed region was close to the debris accumulated area and confirmatory results could not be found under SEM due to the shallow depth change of the boundaries, about 100 nm, which was hard to detect using SEM. The possibility that this is evidence of grain boundary corrosion comes from the height image (Fig. 3.7c) where there is no significant rise in the topography from left (just inside the fretting deformation zone) to the right (where the boundaries are present) that would correspond with an attached corrosion layer, but rather the height is roughly consistent until the grain boundaries appear. There is some attached corrosion debris in these images that overlay the substrate surface which are distinct from the substrate. The depth of the grain boundary grooves increased from outside towards fretting corrosion center. Corrosion, even at one single grain, was not uniform, some grains were only partially subjected to dissolution at their boundary.

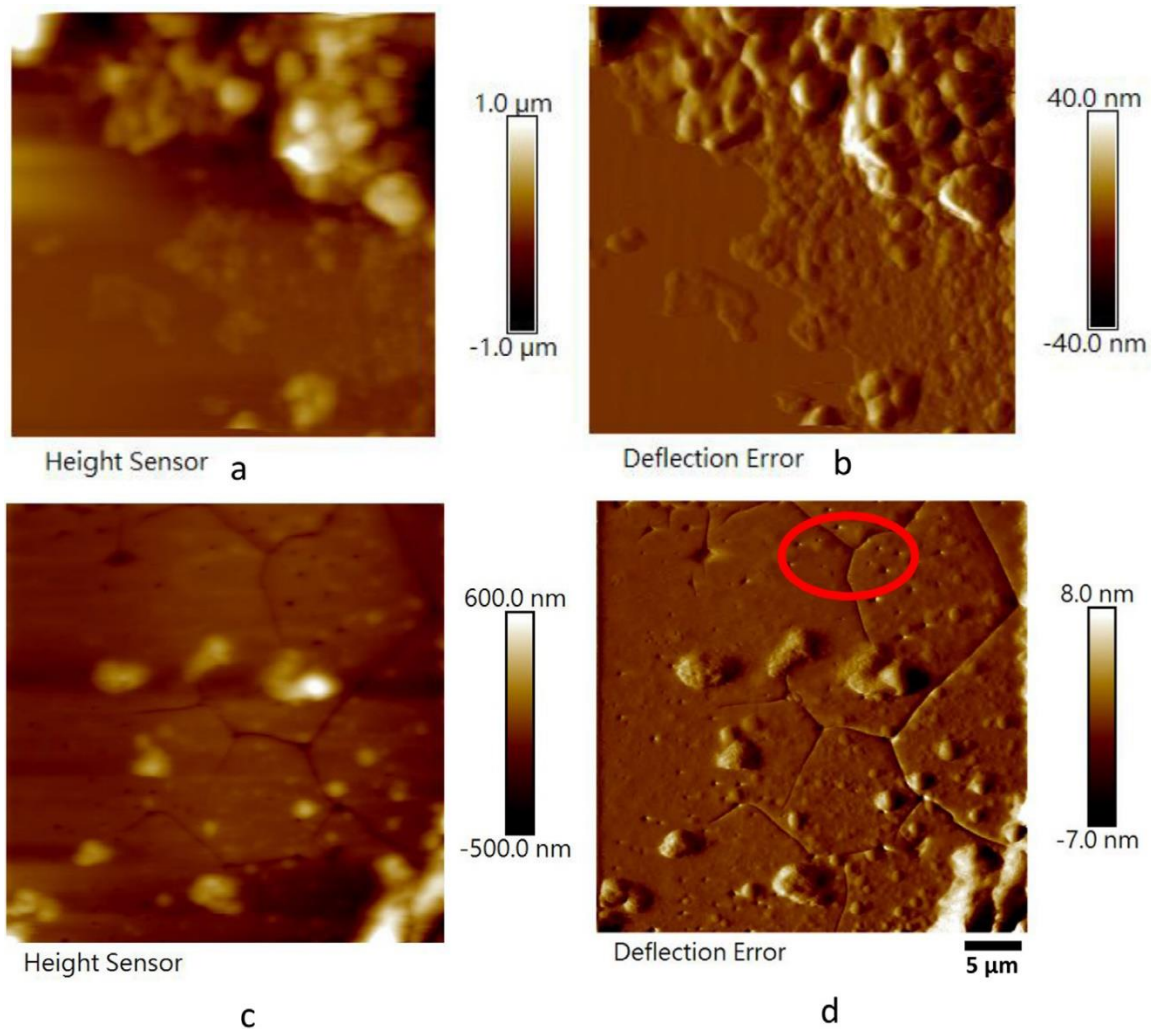


Fig. 3.7. AFM contact mode images ($30 \times 30 \mu\text{m}^2$) of surface after fretting corrosion test. a,b) Height Sensor and Deflection Error images shows surface of debris accumulated region. c,d) Grain boundary dissolution (red circle) was observed at debris accumulated regions outside fretting contact region.

The ICP-MS results are plotted in Fig. 3.8. Among the three of them, Co (1.46 ppm) showed significantly higher solution concentrations than other two elements: Cr (0.07 ppm) and Mo (0.05 ppm) ($p < 0.05$). This indicated that most of the cobalt in the alloy was oxidized into Co ions and released into solution, while the other two metallic elements, Cr and Mo, did not oxidize into an ionic form in solution but rather became

solid corrosion products of Cr/Mo oxides and phosphates. These results support the earlier EDS results which showed that Co was deleted in the fretting debris.

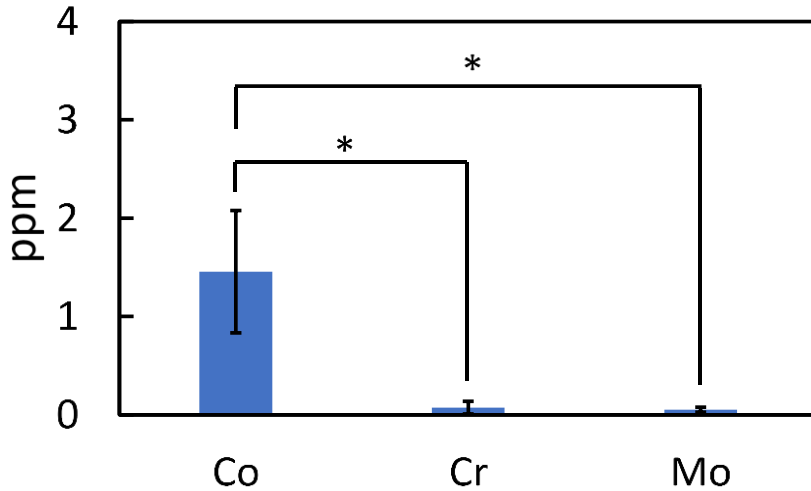


Fig. 3.8. ICP-MS result. Cobalt (Co) has significant higher concentration ($p < 0.05$) compare with the rest of two elements, Cr and Mo. Note that error bar stands for the standard deviation.

3.5 Discussion

The goals of this work were to directly observe the process of debris generation microscopically using a 2D fretting corrosion test system and microscope and to detail/characterize the degradation products and damage modes coming from fretting crevice corrosion of CoCrMo alloys. The whole device can be placed under a digital microscope to visualize the process of fretting corrosion directly. The sample chamber is made of two glass slides and hold much less solution volume. This feature can be used to study the products of fretting corrosion. In addition, the small thickness of the disk sample provides small contact areas which is useful for studying the fundamental theory of fretting corrosion. We have demonstrated that principally chromium-based phosphates and oxides are generated during fretting corrosion and cobalt is principally dissolved in

an ionic form into the solution. Little to no metallic debris (i.e., zero valence metal debris) is generated during fretting crevice corrosion. The fretting crevice corrosion process mostly sequesters solid degradation products within the crevice, with some debris egressing from the contact region. Also, some of the corrosion products are transported away from the fretting region and deposited on the metal surface near to the edge of the nominal pin perimeter where the crevice region ends. This deposition appears to be chemically driven and not a physical adsorption as the rainbow-colored regions that form is not removable, even with cleaning.

All the solid debris was either metal oxide or metal phosphate. There were no observable metallic particles present within the debris. This indicates that the mechanically assisted corrosion process reacts (oxidizes) the metal into virtually 100% corrosion reaction product (both ions and oxide/phosphate). The solid debris accumulates just outside of the contact zone but still within the nominal pin contact area. Debris can also be extruded from this region into the larger solution space as additional fresh debris is generated in the contact zone. Such debris extrusion likely occurs *in vivo* and results in accumulation into the peri-prosthetic space, as has been observed *in vivo*.

Debris particles are generally too small to be observed directly or even in an optical microscope. The isolation process used in this work was only able to harvest a small amount of debris since most of the debris remained attached to the fretted surface. It is only when they are agglomerated together to form a larger piece that they are visible. Visible debris first showed up at 12 min after test began. The junction formed by pin and disk filled with debris that has fluffy appearance on the outward surface. As time

progressed, more debris was created and compacted with each other to form larger pieces. As the fresh debris was generated in the contact zone, the older debris was either compacted into the metal surface or forced out from the center. This could lead to some large piece of debris to be removed from the fretting region and to egress from the crevice. The compacting debris resulted in the dry lake-bed appearance of accumulated debris and the observations of tape-removed debris undersides showed that the surface topography (scratched) was imprinted into the back side of the accumulated debris.

Halos appeared on both fretting interfaces and the side observation surface after the solution was removed. The fretting region was surrounded by the halo, where the inner portion transitions into fretting debris. The halo exhibited color variations (rainbow) from its outer edge to the inside, with a repeating rainbow appearance. This interference effect, similar to anodization effects, indicates an increasing thickness of the corrosion products in this region. The process of halo formation is likely due to corrosion product deposition which has been reported in several studies [79–80]. Halo formation likely results from a gradient of corrosion product accumulated within the crevice between pin and disk. When pin and disk came into contact, a crevice formed between the two surfaces that could lead to a gradient of ionic concentration due to the redox reactions during fretting corrosion. Debris, which is generated along with the electrochemical reactions, began to spread from the contact zone but still within the crevice. The halo only appeared around the pin's edge indicating there was a concentration difference between the inside and outside space of pin's edge. This could include pH gradients, anion gradients and others leading to a precipitation process. Another study from

Stevenson et al., detected a halo and wear debris in serial tribology experiments using bovine calf serum (BCS) and human synovial fluid (HSF) as electrolyte [81]. Thus, halos can develop not only in inorganic (PBS) solutions, as in this study, but also can be formed in more physiological, protein-containing environments as well.

The ionic corrosion products are preferentially enriched in cobalt (Co) ions, where the Co:Cr ratio was about 20, a ratio much higher than the alloy ratio and consistent with the reported higher ratio of Co to Cr in blood samples associated with corrosion modular taper junctions. Studies have shown that metal-on-metal modular taper interfaces produce a significantly higher systemic release of cobalt compared to chromium when significant corrosion of the tapers occurs [75,82]. They also point out that cobalt ion level is higher than chromium after measuring the ion concentration from patients who have total hip replacements for 12 months [83]. Their results and conclusion are consistent with the observation of this study. Ion generation is mainly due to oxidation reactions during the repassivation process. Both cobalt ion generation and chromium (and Mo) oxide and phosphate generation can contribute to electrochemical currents generated at the surface. This small volume controlled fretting test system may be able to quantitatively study the partitioning of degradation products by measuring dissolution currents while also capturing debris, ions and volume losses. In this way, the links between multiple measurement methods could be used to obtain a better understanding of the overall processes involved.

Increased oxygen concentration in the fretted area compared to unfretted area (XPS figure a, b) was contributed to by wear debris on the CoCrMo surface in the fretted

area. This is supported by the EDS results on the wear debris, where high levels of oxides were observed. Oxide film thickness results based on XPS depth profiles in unfretted areas was approximately 2.5 nm, which is consistent with previous studies [84], while that of fretted area, affected by wear debris, exhibits thicker oxide on surface (more than 7.5 nm at least). Meanwhile, slower shift of Cr 2p peak to lower binding energy (metallic form) within first 5 layers in fretted area indicates more Cr were in oxide form (Cr_2O_3 or $\text{Cr}(\text{OH})_3$) on fretted area surface compared to unfretted case. This could be caused by wear debris on the surface or changed chemistry of the native CoCrMo alloy oxide itself. More depletion of Co was observed in the fretted profile, implying that oxide film chemistry was altered due to fretting corrosion. It should be noted that shifts of the Co peak due to tribocorrosion was observed in a previous study in protein-rich environment (50% serum). Co was found to be changed from metallic form to oxidized and organometallic status [85] during tribocorrosion. Thus, protein plays an important role in the oxide film chemistry of CoCrMo alloy in fretting corrosion.

Previous studies show preferential grain boundary corrosion initiation in CoCrMo alloy due to Cr depletion [86-87]. Intergranular corrosion and carbide boundary dissolution have been reported [88-89]. However, grain boundary corrosion of CoCrMo alloy have only been seen above the transpassive potential, which is pH dependent (around 0.6 V vs Ag/AgCl). Our study is the first to show grain boundary corrosion on CoCrMo alloy might occurred in the passive region under potentiostatic (-100 mV vs Ag/AgCl) control. However, it should be noted that this grain boundary corrosion was not able to be identified using the SEM, only the AFM. This is because the dissolution

depth was only around 100 nm or less. The evidence of grain boundary corrosion shown in Fig. 7d could also be the result of a dry-lake effect of surface debris due to this phenomenon was observed near the debris accumulated region. Additional work is needed to confirm these results. It is worth noting that if grain boundary corrosion exists around the fretted region, it might be due to localized surface potential, grain boundary energy and solution chemistry, which favors dissolution at grain boundaries closer to the center of the fretting corrosion. Future study will focus on investigating grain boundary dissolution and its relationship to potential fretting-initiated corrosion in the passive potential region, which has only been observed on stainless steel [90].

This study provides new directions for the study of fretting corrosion using pin-on-disk fretting system. However, there are some limitations. First, no fretting currents were captured during this testing to use to assess the relative electrochemical processes. In addition, volume loss was able to be measured from digital optical microscopy, but the debris mass is difficult to measure. In order to measure the mass of debris precisely, debris from the surface and solution must be collected accurately and completely, which is hard to ensure. In addition, the amount of debris is very limited due to the tiny contact area and short fretting duration. Due to these two difficulties, this study was not able to provide quantitative analysis of mass loss during fretting corrosion. With this limitation, debris generation rate is also not quantitatively calculated in this study. It is worth noticing that debris can be easily generated and agglomerated together quickly after fretting corrosion was initiated. Further investigations are needed to understand the details of fretting corrosion debris generation. This may include, for example, better control and

measurement of crevice solution chemistry and its changes with fretting corrosion, local in situ nano-scale fretting corrosion testing using AFM methods and other approaches to address the fundamental metallurgical, electrochemical and tribological processes involved.

3.6 Conclusions

This study documented debris generation between CoCrMo alloy pin and disk samples, and the surface deformation resulting from fretting corrosion. It was found that debris was generated rapidly during fretting corrosion and that some of the debris egressed from the crevice site while also accumulating within the crevice area as fretting continued. The debris generated was comprised of ions and solid products. The ions were heavily comprised of Co and low levels of Cr and Mo, consistent with blood ion levels. The solid products were virtually entirely comprised of oxides and phosphates of Cr and Mo. This is consistent with observations of debris and ions from clinical patients and retrievals. A halo of corrosion deposition products was also observed at the outer junction between crevice and outside on the alloy surfaces. Finally, visualization of the fretting process using video microscopy methods could provide new insights into the damage modes and debris generation processes and is a useful tool for the study of these microscopy processes.

4. A Metallic Biomaterial Tribocorrosion Model Linking Fretting Mechanics, Currents, and Potentials: Model Development and Experimental Comparison [19]

4.1 Introduction

Mechanically assisted crevice corrosion (MACC) of metallic biomaterials in orthopedics, spinal and dental applications represent a significant concern for clinicians, researchers and implant designers. MACC consists of the conjoint effects of surface disruption of oxide films on passive alloy surfaces of titanium (Ti), cobalt-chromium-molybdenum (CoCrMo), and stainless-steel alloys (316L SS), and the electrochemical responses associated with surface oxide disruption. The process of fretting crevice corrosion in modular tapers (a particular form of MACC) has raised concerns related to release of corrosion and wear debris and metal cations, and the local tissue reactions that may arise [91-95].

Recently, significant work has been undertaken to experimentally study passive oxide film disruption due to fretting and to understand the corrosion response of surfaces to these events [96-101]. These efforts, however, have yet to fully elucidate the links between surface abrasion mechanics, fretting current response and the changes in electrode potential that occur over time during abrasion or immediately after abrasion.

Efforts by Papageorgiou, Mischler et al., and Neville et al. [99,102-105] have provided some of the underpinnings of tribocorrosion processes to model current and potential changes. These works, while providing insights, do not account for all of the

elements of the behavior of the system that are important to the overall response. This includes not accounting for the potential dependence of oxide film growth, or the possibility of non-equilibrium electrical transients wherein the instantaneous balance between anodic and cathodic currents intrinsic to the mixed potential theory may not hold. Mischler et al., have, for example, proposed using a Tafel-based approach for the reduction reactions to determine the cathodic potential excursions observed during tribocorrosion [105]. However, this proposed approach fails to account for the diminishing oxide repassivation response with more negative potentials and the limiting effect this has on the cathodic excursions possible. This model also does not account for the capacitive nature of the electrode interface and the high energy transient reactions associated with repassivation which are not likely to be instantaneously balanced with reduction reactions, but rather may result in a transient capacitive accumulation of charge at the interface. This capacitive effect and other impedance characteristics of the electrode surface are likely to be important in describing the electrode current and potential response.

Kolman et al., modeled current behavior for titanium during film disruption due to scratching, fracture or plastic strain in several publications to assess the true current densities arising from near-instantaneous disruption [106-109]. These studies identified many limitations associated with potentiostatic repassivation experiments, including solution resistance effects on potentiostatic repassivation measurements and their effects on high field modeling by comparing the result of scratch test and thin-film fracture on

titanium. However, many of these effects or concerns are reduced or eliminated when slow speed scratch testing is undertaken where the speed of disruption is slow.

They also graphically described a superposition model for summing multiple dislocation-based plastic deformation events leading to disruption of the oxide film and the individual currents associated with the repassivation process [109]. Each individual transient event can be summed over time into a total current response, similar to what is being developed here with a more formal mathematical description. That is, the basic concept of current superposition was laid out by Kolman and Scully, however, this approach was never formalized into a mathematical model and it was not coupled with an analysis of the potential excursions that also arise.

Recently, Gilbert et al., described an approach to relate fretting currents, electrode impedance characteristics and electrode potential transients [110]. In this work, a link was made between the asperity-based contact mechanics of metal-hard surfaces and the fretting corrosion currents that arise from oxide film disruption resulting from the sliding contact mechanics. An approach was proposed, using a Duhamel integral (also known as Boltzmann's superposition or heredity integral) in conjunction with the area-dependent surface impedance properties, to describe the potential-time response of the fretting electrode. This approach provided a conceptual framework to link the mechanics of oxide film abrasion with the currents and electrode potential changes that an electrode experiences and established a path for a complete and more holistic model of fretting corrosion.

The goals of this study are to extend this approach to develop a coupled set of heredity integrals to first link the abrasion mechanics with the fretting currents and second to link currents to the electrode potentials over time for any arbitrary abrasion-time process. It incorporates several new concepts including an oxide volume disrupted - fretting current transfer function, a hardness and voltage-based link between contact mechanics and volume of oxide abraded, the oxide film high field growth physics, and the impedance characteristics of the electrode surface into a series of expressions that predicts both current versus time and voltage versus time behavior for an arbitrary abrasion process and electrode area. Then, a series of pin-on-disk and single asperity diamond tip abrasion experiments with a range of cyclic sliding frequencies from 0.2 to 10 Hz and sliding speeds between 140 and 550 $\mu\text{m/s}$ were performed to capture impedance, current-time and potential-time behavior under controlled mechanical and electrode area conditions. The model was then analyzed for a fixed set of impedance and physical parameters for the same frequency and sliding contact conditions and the correspondence of the model, in terms of current-time and potential-time behavior, to the experimental results, are compared.

4.2 Fretting Corrosion Model

The fretting corrosion model to be described has several distinct elements. These include: 1. high field oxide film growth, 2. surface contact mechanics concepts for metal-hard contacts (e.g., metal-metal, ceramic-metal), 3. fretting sliding mechanics, 4. current-oxide volume transfer function, 5. electrode impedance concepts and 6. voltage-

impedance-current relationships. Table 4.1 is the nomenclature table for terminology explanation.

Table 4.1. Nomenclature table for parameters terminology

Parameter	Name
ρ	oxide density
n	valence
M_w	molecular weight
$\theta/\Phi(\rho nF/M_w)$	
H	surface hardness
F_N	normal load
τ	time constant for repassivation
m	anodization rate
E_o	onset potential
R_s	solution resistance
R_{ox}	oxide resistance
C_{ox}	oxide capacitance
τ_{ox}	oxide time constant

The impedance elements of the model are intended to incorporate the capacitive and the resistive nature of the interface where both interfacial charging and reduction currents can occur. While the associated reduction currents (also called the return currents) are distributed over and depend on the surface area and solution resistive paths, the impedance of the electrodes in this model is assumed to be in a lumped parameter condition reflective of the area of the electrode available for such return currents [110].

It should be noted that the current densities defined here are the result of both oxide film formation and ionic current passing the abraded surface. While both sources of current are included in the analysis, this work will focus mainly on the oxide film-based currents. High-speed electrochemical scratch tests have shown that Ti alloy and CoCrMo alloys experience spike-exponentially decay current transients due to oxide

abrasion which are well-described by the Ambrose Model [111-113]. Ionic dissolution current densities were considered as part of the terms of the peak current. However, within the range of potentials investigated in this work, it was estimated that only 10% of the peak current was due to dissolution and 90% or more was due to oxide film regrowth. The estimation of film current densities (due to oxide formation) are much larger than ionic dissolution current densities that may arise at the abraded metal interface and therefore, in this work, the ionic dissolution currents were not included in the analysis but are discussed later.

4.2.1 High Field Model of Oxide Growth and Linear Thickness-Voltage

Relationship

The high-field low temperature growth model of oxide films, first articulated by Cabrera and Mott, and Gunterschulz and Betz [114,115], shows that the oxidation currents associated with repassivation can be described according to equation 1:

$$i = A \exp\left(B \frac{V - V_o}{x}\right) \quad \text{Eq. (1)}$$

where i is the film based current density, V is the electrode potential (i.e., the potential drop across the film), V_o is the potential above which oxide film can form thermodynamically (i.e., the onset potential [112-114] or passivating potential [118]), x is the film thickness and A and B are material-specific constants. This function shows that the film current density drops rapidly with thickness, x , and the corresponding drop in the electric field (see Figure 4.1).

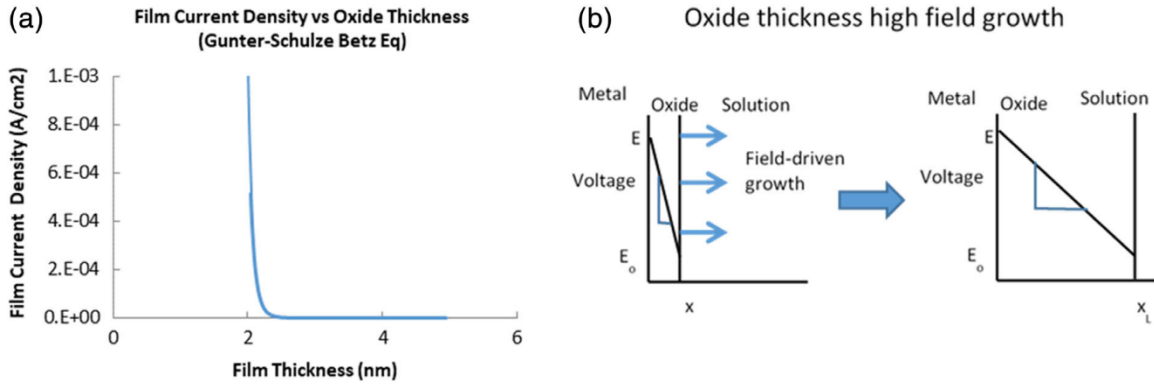


Fig. 4.1. High field film currents with oxide thickness based on Gunter-Schulze Betz Eqn ($i_L=10^{-7}$ A/cm², $A=10^{-18}$ A/cm², $B = 3 \times 10^{-6}$ cm/V). Film growth to a limiting thickness is predicted to be linearly dependent on electrode potential.

If one assumes that the oxide film will regrow up to a limiting film thickness, x_L , this will occur when the current density reaches a limiting value, i_L , and this expression can be recast as

$$x_L = B \ln^{-1} \left[\frac{i_L}{A} \right] (V - V_o) = m(V - V_o) \quad \text{Eq. (2)}$$

$$m = B \ln^{-1} \left[\frac{i_L}{A} \right]$$

where m is the so-called anodization rate (nm/V) for the oxide. Typical values for m are about 2 nm/V for Ti and CoCrMo oxide films [112-114]. This shows that the high-field model predicts a linear relationship between oxide thickness and voltage above the passivating potential and is consistent with studies showing a linear increase in scratch currents with potential [114] in the passive potential region at least up until another set of electrode reactions may arise (e.g., transpassive dissolution of oxides). Thus, oxide film thickness is directly related to the potential across the electrode interface for the range of

potentials where the film remains stable (i.e., above V_o and below the transpassive or breakdown potential).

4.2.2 The role of Contact Mechanics and Sliding Displacements on Current Generation

The next element of the model is the contact mechanics and the link between volume of oxide abraded to the volume of oxide repassivated. Prior work has shown that one can relate fretting currents to contact mechanics [100]. These currents depend on the surface contact and sliding mechanics present. For hard-on-metal surfaces, contact areas are a direct consequence of the normal load between the two surfaces and the effective hardness of the materials given as a stress. That is, from basic contact mechanics analyses, the real contact area can be estimated by

$$A = \frac{F_N}{H} \quad \text{Eq. (3)}$$

where F_N is the normal load across the surface, and H is the hardness of the surface [119]. This real area of contact is not dependent on geometry or roughness (for small roughnesses) but relies only on the fact that hard-on-hard surfaces will result in the surface plastic deformation needed to just carry the load. These areas are typically only a small fraction of the total nominal contact area.

To find the sliding area, or area of abrasion, if one assumes that the contact area is approximately circular, then the diameter, d , of the contact area (assumed to be circular in this case) is approximated by:

$$d = 2 \left(\frac{F_N}{\pi H} \right)^{1/2} \quad \text{Eq. (4)}$$

If the contact area is made up of multiple circular asperity contact points, then the above equation needs to be modified to account for the sum of all the asperity contact diameters as

$$d = \sum_{i=1}^n d_i = n\tilde{d}_i = 2 \left[\frac{nF_N}{\pi H} \right]^{1/2} \quad \text{Eq. (5)}$$

where d_i are the individual contact asperity diameters (assuming circular asperity contact) and n is the number of asperities in contact. Equation 5 shows that the length of fretting contact, d , depends on the number of asperities in contact and their average diameter. However, for small contact regions, (i.e., pin-on-disk contact less than 500 μm), as in this study, the contact can be approximated as a single asperity ($n=1$) of diameter, d .

Because the repassivation rate of oxides disrupted under these conditions is rapid (on the order of milliseconds) compared to the rate of disruption, the rate of repassivation will be limited by the rate of disruption and for most cases of fretting, the two can be equated (i.e., Rate of repassivation = Rate of disruption). Thus, during pin-on-disk sliding (or generally fretting motion), the rate of volume of oxide repassivation during sliding is equal to the rate of volume abraded and the volume of oxide repassivated can be determined using

$$\frac{d\Phi}{dt} = dx_L \frac{d\delta}{dt} = 2 \left(\frac{F_N}{\pi H} \right)^{1/2} m(V - V_o) \frac{d\delta}{dt} \quad \text{Eq. (6)}$$

where Φ is the volume of oxide abraded (and repassivated), and $d\delta/dt$ is the instantaneous sliding speed of the pin on the disk. The oxide thickness, x_L , and the approximate asperity diameter, d , are approximated by Eqs. 2 and 4, respectively. This equation assumes that

everywhere where asperity contact occurs (where the stress of contact is at yielding) the oxide film will be completely removed from the surface.

Thus, this expression combines information on the contact mechanics (hardness and normal force), oxide film repassivation (high field growth), and the sliding behavior of the contact ($d\delta/dt$) to predict the rate of disruption/formation of the oxide film. One assumption in this analysis is that the sliding speed is slow compared to the repassivation speed such that the rate of volume disrupted is equal to the rate of the volume repassivated (i.e., repassivation rate is limited by the depassivation rate). In addition, the contact diameter and oxide film thickness are assumed not to be strong functions of time and their variation with time will be accounted for in the coupled numerical integrals to be developed (see below). Thus, Eq. 6 provides a link between fretting abrasion and oxide film repassivation.

4.2.3 The Current-Oxide Volume Abrasion Heredity Integral

Next in the model is the need to link the film repassivation currents to the rate of oxide film volume repassivation. To do this, a heredity integral, also known as a Duhamel integral, is required [118]. This integral is of the form

$$I(t) = A^T(t)\Phi(0) + \int_0^t A^T(t-\lambda) \frac{d\Phi}{d\lambda} d\lambda \quad \text{Eq. (7)}$$

where $I(t)$ is the current resulting from abrasion (or fretting), Φ is the volume of oxide abraded (and repassivated), A^T is defined here as the tribocorrosion transfer function linking the volume abraded to the current, and λ is a dummy variable in time. The Duhamel integral can predict the current, I , at any time, t , with knowledge of how the

oxide film is abraded and repassivated over time and the tribocorrosion transfer function. These integral functions have been used extensively in viscoelastic theory (i.e., Boltzmann's superposition principle [120]). Schematically, this heredity integral (see Figure. 4.2) represents the sum of infinitesimal oxide disruption/repassivation events summed over time.

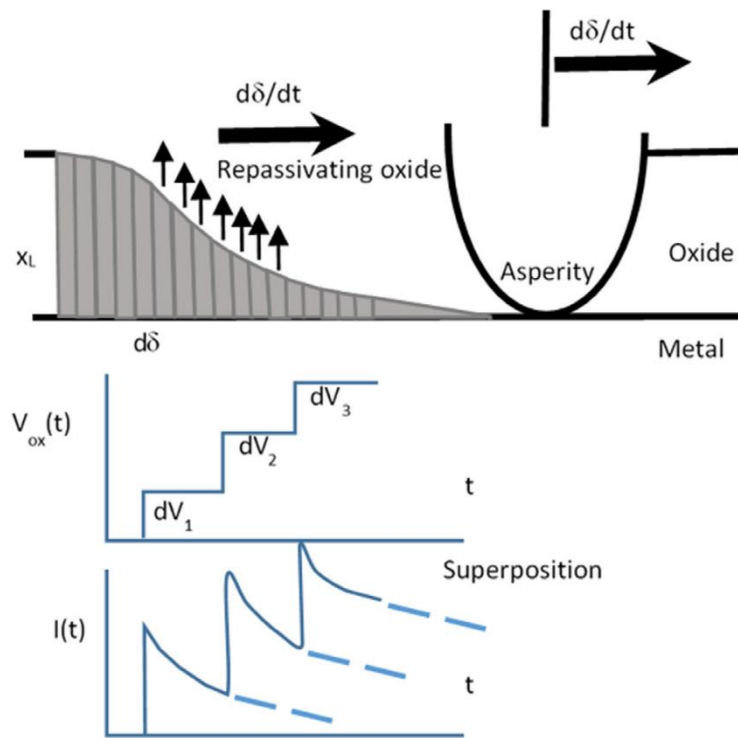


Fig. 4.2. Schematic of the disruption-repassivation process of an asperity. Each infinitesimal disruption-repassivation event generates an infinitesimal column of oxide growth with an associated exponential current transient response that can be summed over time using a Duhamel integral to obtain the overall current response.

The tribocorrosion transfer function, $A^T(t)$, can be found by understanding the current transient response of an oxide film covered surface to an instantaneous removal of a fixed volume of oxide and determining the current-time response at a fixed potential.

This has been done previously [113-114], and the resulting relationship when both film currents and ionic dissolution are present is

$$A^T(t) = \frac{I_o}{\Phi_o} e^{-\frac{t}{\tau}} = \left(\frac{\rho n F}{M_w \tau} + \frac{i_o}{x_L} e^{\frac{\eta}{\beta_a}} \right) e^{-\frac{t}{\tau}} \approx \frac{\rho n F}{M_w \tau} e^{-\frac{t}{\tau}}$$

$$A^T(t) = \frac{I(t)}{\Phi_o} = \frac{\theta}{\tau} e^{-\frac{t}{\tau}} \quad \text{Eq. (8)}$$

where Φ_o is the oxide volume repassivated, θ is the charge per volume oxide and τ is the time constant for the instantaneous scratch response. The value of θ is given by Faraday's equation

$$\theta = \frac{\rho n F}{M_w} \quad \text{Eq. (9)}$$

where ρ is the oxide density, n is the charge per cation, F is Faraday's constant and M_w is the molecular weight of the oxide. Also included are the exchange current density for bare metal surface (i_o), oxide thickness, x_L , the overpotential, η , and the Tafel slope β_a . Prior sensitivity analysis shows that the ionic term is small compared to the film currents and is thus ignored for the remaining analysis. However, in cases where it is not small, the ionic term can be incorporated into the analysis.

The tribocorrosion transfer function ($A^T(t)$) depends on τ the time constant for repassivation which can be directly measured in the experimental setup from the recovery of the current at the end of an abrasion event. Combining Eqs. 6-9 results in

$$I(t) = \frac{\theta}{\tau} e^{-\frac{t}{\tau}} \Phi(t=0) + \int_0^t 2 \frac{\theta}{\tau} \sqrt{\frac{F_N}{\pi H}} m (V - V_o) e^{-\frac{t-\lambda}{\tau}} \frac{d\delta}{d\lambda} d\lambda \quad \text{Eq. (10)}$$

Typically, the volume of oxide abraded at $t = 0$, $\Phi(t=0)$, is zero so the first term drops out. This expression predicts the tribocorrosion current, I , at any arbitrary time point, t , based on the sum of all oxide film disruption events that have occurred up to the time t . This is similar to the approach proposed by Kolman and Scully previously, but never reduced to a theoretical model. It incorporates the contact mechanics and the resulting area or diameter of contact, the instantaneous voltage, V , and a set of parameters related to surface hardness, charge per oxide, onset potential for oxide formation, anodization rate and the time constant for repassivation. It should be noted that the potential, V , associated with fretting corrosion will vary with time and is coupled to the currents generated (see below), therefore, determination of the current at any point in time will also require knowledge of the potential variation in time (i.e., the two functions are coupled in time).

4.2.4 The Potential-Impedance-Current Heredity Integral

The link between abrasion mechanics, current generation and the shifting of electrode potentials depends on the impedance characteristics (resistive and capacitive character) of the electrode system. Both the abraded region, and the regions of the surface that are electrically connected to the abraded region contribute to the overall impedance of the surface. The capacitive character of the electrode surface (which is well studied in electrochemical impedance analyses) provides an ability for the charge associated with the burst-like repassivation reactions to be captured and stored transiently. The area available for capacitive charging and for reduction-reaction-based consumption of charge is accounted for in this analysis. The total area of the electrode

will affect how much the electrode potential drops and how long it takes to recover. Therefore, an approach utilizing the total impedance of the electrode surface is presented [112].

A schematic of this approach is shown in Figure 4.3. The electrode area not engaged in abrasion is the site where reduction currents are passed through resistive elements or stored capacitively until reduction can remove the charge. While the spatial distribution of current densities returned will vary across the electrode area due to varying resistive paths in the solution, it is assumed here that the entire reduction current can be lumped into a single representative Randles circuit as shown. Thus, for the lumped parameter case, the time- and area-dependent impedance of the electrode is

$$Z(t - \lambda) = R_s + R_{ox} \left(1 - e^{-\frac{t-\lambda}{\tau_{ox}}} \right) \quad \text{Eq. (11)}$$

where R_{ox} is the lumped area-dependent representation of the oxide resistance (in Ohms, Ω), C_{ox} is the lumped area-dependent capacitance (in Farads, F), R_s is the lumped solution resistance (between the abraded region and the remaining electrode) and τ_{ox} is the oxide time constant ($R_{ox}C_{ox}$) [112]. In many circumstances, the solution resistance term is small compared to the R_{ox} term ($R_s \ll R_{ox}$) and can be ignored in this analysis. In other cases (low ionic strength electrolyte, crevice-like geometries) the solution resistance can be significant. As mentioned, the values for R and C are dependent on the area of the electrode exposed to solution with larger exposed areas resulting in smaller R's and larger C's. (i.e., these parameters are extrinsic).

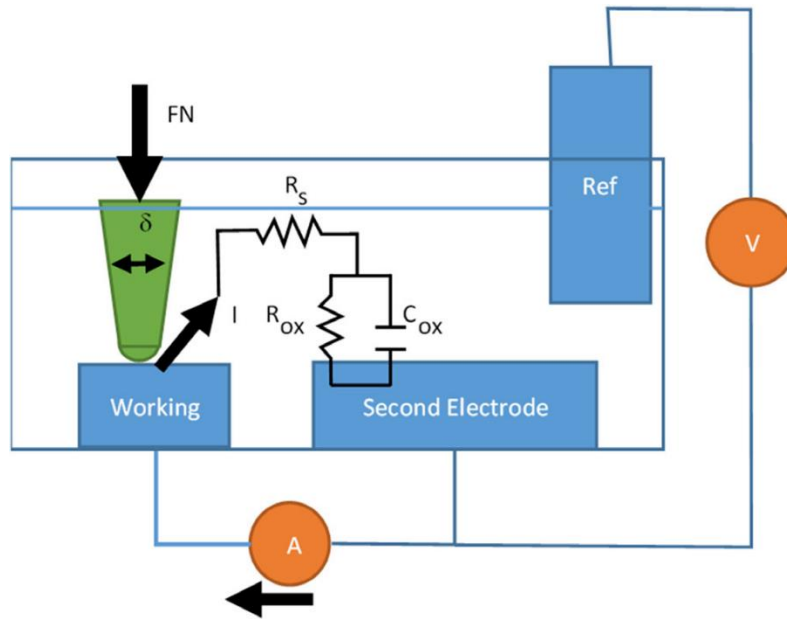


Fig. 4.3. Pin-on-disk impedance-model used in this study to relate potential-time behavior to abrasion-time behavior. All anodic processes are assumed to occur at the working electrode, while the associated charging and reduction currents are assumed to occur at the second electrode. The potential of the entire system is monitored.

The electrode potential can then be determined from another Duhamel integral of the form [110]

$$V(t) = Z(t)I(0) + \int_0^t Z(t - \lambda) \frac{dI}{d\lambda} d\lambda \quad \text{Eq. (12)}$$

This integral, therefore, can determine the electrode potential at any time, t , if the current versus time history is known and the impedance of the electrode surface is known.

4.2.5 The Combined Abrasion-Current-Impedance-Potential Model

In the case where the electrode system undergoing abrasion can freely change its electrode potential (due to abrasion events and the associated generation of currents), then there is a coupling of Eq. 12 and Eq. 10 over time. That is, if the abraded region is

connected to the return electrode region by way of a zero-resistance ammeter to measure the current (see Figure 3) and the potential of the combined electrode system can be monitored, then these currents and electrode potentials will vary and will depend on the electrode area and impedance, as well as the mechanics of the abrasion. To model this circumstance, the two heredity integrals are coupled and interact in an iterative fashion over time such that generation of abrasion currents cause the potential to change, and the changing potential alters how the currents are generated. Since the oxide film thickness depends on the potential, the amount of oxide reformed will decrease as the potential becomes closer to the passivating potential, thus the currents will be affected, which in turn will affect the potential, and so on.

To deal with this coupled interaction, the two integrals need to be integrated numerically where iterative changes in voltage and current are fed back in the next increment in time to the other integral so that both are modified by the effect of the other through time.

This can be done, see Figure 4.4, with the algorithm used, with a set of nested iterative loops over time, where the index j reflects the steps in the variable t , while the index i reflects the steps in the variable λ . Thus, for each step in time the values of both current and potential can be determined as both vary and are affected by the other.

The numerical algorithm in Figure 4.4 was applied to compare with the experimental portions of this work in order to show how one can predict the current and potential variations that arise as the result of mechanical abrasion of a surface oxide film and with knowledge of the impedance of the electrode. The sliding displacement (and

velocity) profile used in the numerical analysis was taken from the measured sliding displacement-time behavior of the experiment so that a direct comparison could be made.

```

For j = 1 to n
'start values for both V and I at zero
  Ij = 0
  Vj = 0
  For i = 1 to j
    Ij = Ij + k(Vi - Vo)e- $\frac{t_j - t_i}{\tau}$  |(δi - δi-1)|
  Next i

  For i = 1 to j
    Vj = Vj - (Rs + Rox (1 - e- $\frac{t_j - t_i}{t_{ox}}$ )) (Ii - Ii-1)
  Next i
Next j

```

Fig. 4.4. A simple algorithm for the coupled iterative calculation of both the V(t) and I(t) heredity integrals over time ($k = 2\frac{\theta}{\tau}\sqrt{\frac{F_N}{\pi H m}}$). These expressions can be used to find the voltage and current at any time from the abrasion-time and impedance characteristics of the electrode.

4.3 Materials and Methods

4.3.1 Materials

To evaluate the proposed model described above, a series of fretting corrosion pin-on-disk experiments were performed. These experiments were conducted using cobalt-chromium-molybdenum alloy (CoCrMo) that adheres to ASTM F1537 high carbon wrought CoCrMo alloy for both pin and disk elements. The disk was covered with

acrylic lacquer except for the electrode area and the pin was similarly coated except for the contact region where fretting was performed.

The solution used in these experiments was a 0.154 M isotonic phosphate buffered saline (PBS) solution at room temperature, made by dissolving one packet of phosphate buffer (P3813, Sigma Aldrich, St. Louis, MO, USA) into distilled water. This physiologically representative inorganic aqueous electrolyte provides a simple, yet representative solution to study oxide film disruption and repassivation to verify the model. In some experiments, DMEM w/10% FBS was used to assess performance in a more physiologically situation.

For the single asperity diamond scratch tests, a diamond stylus 16 μm in radius was used to apply a constant sliding speed scratch to a polished CoCrMo surface while immersed and under a fixed potential (100 mV vs Ag/AgCl) and load.

4.3.2 Methods

4.3.2.1 Electrochemical Test Configurations

In the pin-on-disk fretting corrosion test configuration (see Fig. 3) [121], the pin and disk comprised one electrode (both CoCrMo) while a second electrode, also made from CoCrMo alloy, was connected to the pin and disk through a zero-resistance ammeter (ZRA, 485 Autoranging Picoammeter, Keithley Instruments Inc, Cleveland, OH, USA) to allow measurement of the currents passing from the fretting interface to the area where reduction reactions were taking place. The electrode potential of the combined sample (primary and secondary electrodes) was monitored versus Ag/AgCl reference electrode. The second electrode area was 0.018 cm^2 , the nominal fretting

distance was 50 μm and the normal load, F_N , was 0.5 N for pin and disk fretting corrosion test.

4.3.2.2 Fretting Apparatus

The custom fretting corrosion test system was comprised of a pin mounted to a custom load cell and the disk was mounted in a solution chamber attached to a precision controlled piezoelectric actuator (Burleigh Instruments). The load cell consisted of a calibrated double cantilever system with Linear Variable Differential Transformer (LVDT, Macro Sensors, Pennsauken, NJ, USA) to impart controlled normal loads to the sample. The lateral deflection of the pin (and lateral frictional forces) was captured during fretting by a non-contact differential variable reluctance transducer (DVRT, Micro-Epsilon Inc, Raleigh, NC, USA). The pin deflection was subtracted from the disk motion to obtain the true pin-disk motion over time. The piezoelectric actuator moved the disk relative to the pin to impart controlled sliding displacements over time which were captured by the linear variable differential transformer (LVDT) over a sliding distance of 50 μm for most of these tests. For most frequencies tested, the sliding waveform was trapezoidal wherein for each cycle there was a motion-pause displacement-time response. At higher frequencies (5 Hz and 10 Hz), the displacement-time plots were more saw-tooth in appearance. The mechanical factors of sliding displacement and normal forces, and the electrochemical factors of fretting current and combined electrode potential were captured using data acquisition methods (LabVIEW, National Instruments, Austin, TX, USA) at 200 pts/s per channel. In tests to assess waveform and solution chemistry effects, the pin was replaced by the diamond stylus.

4.3.2.3 Pin-on-Disk Fretting Corrosion Tests

Two fretting corrosion tests were performed to demonstrate the model. In the first experiment, a freely corroding condition (i.e., where the electrode potential of pin, disk and second electrode freely varied over the course of testing) was monitored. Prior to the start of fretting motion, the potential was allowed to equilibrate and was consistently observed to be within -0.1 to -0.11 V (vs Ag/AgCl) prior to the start of testing. The frequency of fretting sliding was varied between 0.2, 0.5, 1, 5 and 10 Hz and the fretting currents and electrode potentials were captured over at least 25 s in each test for comparison. Three tests for each frequency were performed to evaluate the consistency of the time course of the currents and potentials observed.

4.3.2.4 Single Asperity Diamond Tip Fretting Corrosion Tests

The second experiment was performed under fixed potential (0.1 V vs Ag/AgCl) in order to maintain a stable electrochemical condition, therefore, only the current was captured and assessed. A diamond tip with 16 μm radius was placed into contact with the CoCrMo disk. The frequency was 1 Hz and normal load was controlled as 0.2 N. Ten seconds of fretting data was captured to show complete fretting current behavior. Sinewave and square-wave fretting motion were tested in PBS to compare to the currents calculated by the model both in terms of the load – abrasion area (i.e., contact mechanics) effects and to assess the effect of different sliding waveforms (sinusoidal and trapezoidal). Dulbecco's Modification of Eagle's Medium (DMEM, Mediatech, Inc., Manassas, VA, US) was selected as an alternative physiologically representative

electrolyte to simulate biological situation. Results in DMEM were compared with those using PBS as the electrolyte.

4.3.2.5 Single Asperity Single Scratch Tests

In these experiments, a CoCrMo alloy disk with fresh polished surface was mounted in an electrochemical chamber. A pin with a 16 μm radius diamond tip on the end was forced into contact with the surface and single scratches were imparted across the surface in PBS at room temperature. Two different contact loads (0.1 N and 0.25 N) and two different nominal sliding speeds (140 $\mu\text{m/s}$ and 500 $\mu\text{m/s}$) were used to induce controlled scratches and their associated currents. The system motion and loading were controlled with a custom written code (using Component Works, NI) to control DC motors and to measure loads and position. The potential was fixed at 100 mV (vs Ag/AgCl) and current was recorded using the same data acquisition system as fretting corrosion test (LabVIEW, National Instruments, Austin, TX, USA). The scratch distance was fixed at 1000 μm . Scratch widths were measured using a digital microscope (Keyence, KH8800, NJ) after each test to verify abraded area and hardness.

4.3.3 Analysis of Results

The resulting data (displacement, current, potential and time) were analyzed using the model described above. Values for various parameters (e.g., hardness, oxide density, valence, etc.) were either obtained from the literature, calculated based on the mole fraction of alloying elements in the alloy, or measured experimentally. Table 4.2 summarizes the physical properties of the CoCrMo alloy oxide values used in this

analysis. The density, ρ , valence, n , and molecular weight, M_w , of the CoCrMo oxide were calculated from the mole fraction of metal elements (Co, Cr, Mo) in the alloy.

Table 4.2. Oxide Physical Properties Based on Mole Fraction Estimation of Alloy Composition

Parameter	TiO ₂	Co-Cr-Mo oxide	316L SS Oxide	Unit
ρ	4.45	6.1	5.81	g/cm ³
n	4	2.4	2.9	
M_w	79.9	76.91	130.09	g/mol
θ	21498	18369	12498	C/cm ³

Note: ρ , n , M_w are calculated based on the mole fraction of each metal in the alloy.

Table 4.3 summarizes the additional mechanical and electrochemical parameters used in the tests and/or analysis. These values were maintained fixed for the analysis of all results across all frequencies tested. The hardness was estimated from known values of the hardness of CoCrMo surfaces. The onset potential, E_o , and time constant, τ , comes from high speed scratch tests which investigated the potential dependence of the oxide disruption/repassivation response. The anodization rate, m , was also estimated from these scratch tests [111,112,119] and is consistent with what others have reported on the oxide growth rate with potential [121].

Table 4.3. Parameters used for Current and Voltage Calculations

Parameter	Unit	Value
H	GPa	3
F_N	N	0.5
$\Phi(\rho n F / M w)$	C/cm ³	18400
τ	s	0.04
m	cm/V	0.0000002
E_0	V	-0.45
R_s	Ω	10
R_{ox}	Ω	1500000
C_{ox}	F	0.000015
τ_{ox}	s	22.5

The impedance values used to calculate the potential-time response are in the range of those reported for CoCrMo but were selected by manually adjusting R and C and fitting the calculated potential-time response for one specific test result (0.5 Hz, test 1) and then the same impedance values were utilized in all of the other analyses of potential and current behavior for all other cases and frequencies tested with this set up. The fitting of R and C was based on the minimization of the error between the experimental and calculated potential response and was done manually. Once determined, these values were fixed for all experiments.

In order to make comparisons of potential-time and current-time behavior from each experiment with the numerically calculated potentials and currents, the sliding displacement-time data from each test was used (δ_i , see Figure 4.5) in each numerical integral to perform the coupled numerical integration to determine currents and potentials over time for each experiment.

The numerical integration was performed using the Visual Basic Program in Excel, where the displacement-time data from the experiments were imported into Excel and the displacement data were used in the numerical algorithm (Figure 4.4) using the parameters in Tables 4.2 and 4.3 to calculate the theoretical currents and potentials resulting from the sliding displacement time inputs. Prior to their use in the Duhamel integrals, the displacement-time data were smoothed using a nine-point running average smoothing algorithm. This reduced the influence of random electronic noise on the output currents (discussed more thoroughly below).

Experimental potential-time and current-time response for each frequency was compared to the calculated values. In addition, the average current, root-mean square (rms) current about the average, and the average potential excursion at 25 s of testing were measured from the experimental data and calculated from the numerical analysis and compared at each frequency.

The fretting current results using different waveforms were plotted versus time for both experimental and calculated results to demonstrate the model. Average fretting current over 20 s of time was measured and calculated for two different solutions (DMEM, PBS). The average fretting currents obtained experimentally and calculated using the measured displacement waveforms were compared and statistical analysis (one-way ANOVA) was performed to determine whether significant differences between experimental data and calculated data were present for both two solutions.

In the single asperity diamond scratch tests, the theoretical currents were calculated based on the parameters in Table 4.4 and the measured sliding speeds using

the steady state version of Eq. 10. Here the currents depended on the square root of the normal force (F), and the sliding speed (i.e., $I = KF^{1/2}d\delta/dt$, where K is a constant.) Plots of average fretting current versus $F^{1/2}d\delta/dt$ were generated to compare the experimental and theoretical values for two normal loads (0.1 and 0.25 N) and different measured sliding speeds (141, 143, 484, 540 $\mu\text{m/s}$) measured for the sliding motion. In addition, the scratch width versus normal load from these tests were obtained from optical micrographs after different contact loads were applied. Scratch widths were measured using digital optical microscopy (Keyence, KVH600, Keyence, Inc., Mahwah, NJ).

Table 4.4. Parameters used in scratch test to calculate theoretical current

Parameter	Unit	Value
Potential	mV	100
Oxide Thickness	μm	0.0022
Scratch Distance	μm	1000

4.4 Results

Typical results of experimental and theoretical current-time and potential-time responses for 0.2, 0.5 and 5 Hz responses (Figure 4.5) demonstrate the basic response of the system to the sliding waveforms (δ vs t). In each plot in Figure 4.5 the sliding displacement-time curves associated with the experiment and which were used in the numerical calculations are shown. Several observations can be made from these data. First, the theoretically-calculated currents and potentials are consistent with the

experimentally obtained values over time and across the range of frequencies tested. At the lower two frequencies (0.2 and 0.5 Hz, Figures 5a and 5b, respectively), the fast step-like displacement motion followed by a stationary phase resulted in current spikes and decays for each motion (at double the frequency of sliding since there are two strokes in motion for each cycle of fretting). This is seen in higher temporal resolution in Fig. 4.6. The current would spike during sliding and recover to near baseline during the pause phases of the motion waveform. The potentials also show a step drop –exponential recovery like behavior for each sliding increment, both experimentally and theoretically, for these low frequency tests corresponding to the motion-pause nature of the sliding. As the frequency increased to 5 Hz (Figure 4.5c), the sliding waveform became more sinusoidal or sawtooth and the fretting currents demonstrated their cyclic nature, however, a full current recovery was not possible at these frequencies and the sliding of the next adjacent movement segment generated another current transient which was superimposed on the prior current. As a result, the average fretting current rises. In addition, the potential drop observed during the fretting at 5 Hz no longer exhibits the step-recovery-like behavior seen in individual cycles at lower frequencies but does retain the overall exponential potential drop behavior. The experimental results and the theoretical calculations are highly consistent across all of these experimental conditions. Detailed comparisons (Fig. 4.6) between experiments and theory show some variations between the two that, in part, have to do with the inability to directly capture the exact pin motion over time. In some cases the theory predicts lower currents than experiment

shows, and sometimes they are larger. These differences, however, are small and the basic waveform and voltage excursions are reasonably well captured.

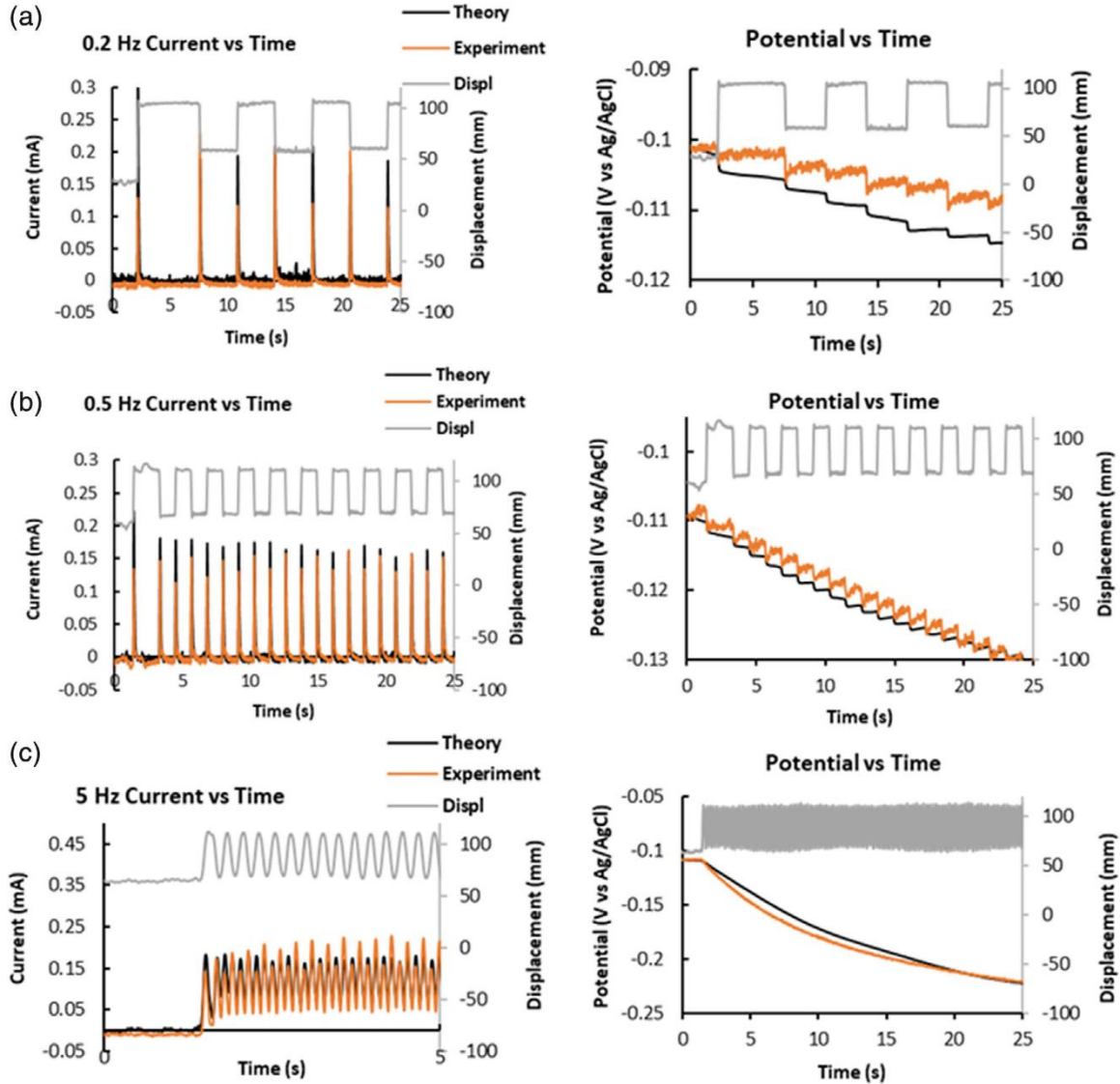


Fig. 4.5. Examples of fretting current and potential time plots from both experiments and Duhamel integral calculations for a) 0.2 Hz, b) 1 Hz, and c) 5 Hz. Theoretical currents and potentials were obtained using fixed parameters (Tables 2 and 3) and displacement-time data. Note: Current-time plot for 5 Hz is shortened in time to 5 s to see waveforms. In addition, the potential-time plots for 0.2 and 0.5 Hz show cyclic responses (oscillations due to each sliding action) superimposed on longer-time exponential transients for both experiment and theory.

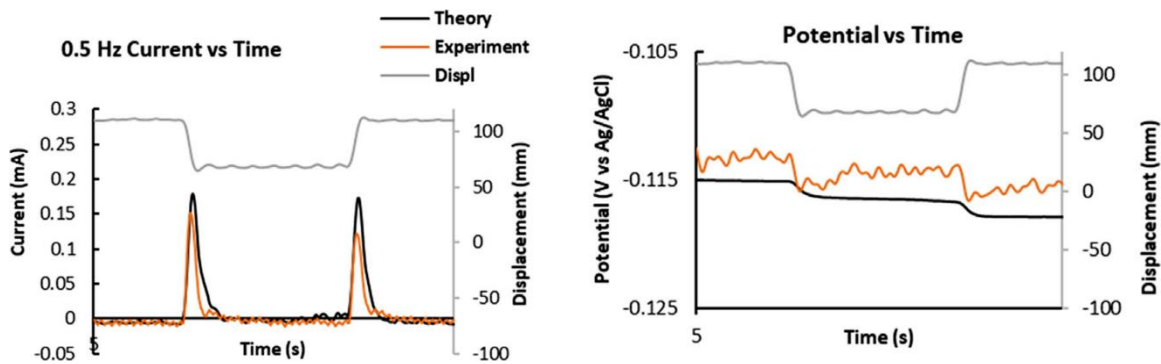


Fig. 4.6. A high temporal resolution example from a 0.5 Hz test of the current vs time and potential versus time for both experiment and theory.

A summary analysis across all frequencies (Figure 4.7) analyzed the average and root mean square about the mean fretting corrosion currents (Figure 4.7a), and the potential change observed from the start of fretting to 25 s after the start (Figure 4.7b) for both the experimental results and the theoretical results obtained from the Duhamel integrals using the mechanical, physical and impedance properties in Tables 4.2 and 4.3. For both experimental and theoretical currents, the average fretting currents rise somewhat exponentially with frequency while the rms currents rise to about 1 Hz and then decrease with increasing frequency. Both theory and experiment show similar results although there are some differences in the magnitude of the results at 5 Hz and 10 Hz. The rms current behavior can be explained by the time constant, τ , in the tribocorrosion transfer function (Eq. 6). As the frequency of fretting increases, the ability of the current to fully decay prior to the next sliding increment is limited, therefore, the next stroke superimposes the next associated current transient and the average current rises while the rms current decreases in magnitude.

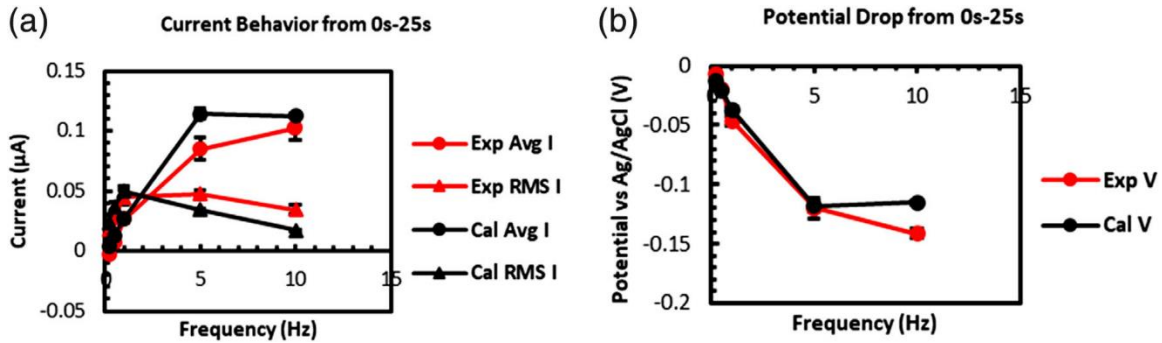


Fig. 4.7. Summary analysis of a) average and root mean square about the average currents and b) potential drop during fretting corrosion of CoCrMo surfaces under controlled loads, electrode area and sliding distance as a function of sliding frequency. Both experimental data and the theoretical results are presented for comparison.

The potential drops observed during the first 25 s of fretting (Figure 4.7b) are very consistent between the experimental and theoretical results, with the exception of the 10 Hz data where the theory underestimates the potential drop. These theoretical electrode potential excursions are highly dependent on both the fretting mechanics but also the impedance values (R_{ox} and C_{ox}) used to make the calculations.

During the single asperity diamond scratch tests, faster scratch speeds and higher loads lead to higher steady state currents at the fixed potential (see Fig. 4.8a and 4.8b). Figure 4.8a shows the raw data for the four tested conditions with the currents increasing at the start of the scratch and falling back to baseline afterwards. When scratch currents are plotted against the sliding speed times the square root of load, a linear variation in current can be seen (Fig. 4.8b) and the calculated currents and measured currents are substantially similar to each other. In addition, the scratch widths measured using optical microscopy (Fig. 4.9a) show the measured widths of the scratches obtained for the loads

applied (Fig. 4.9b). These widths are consistent with the hardness value used in the analysis.

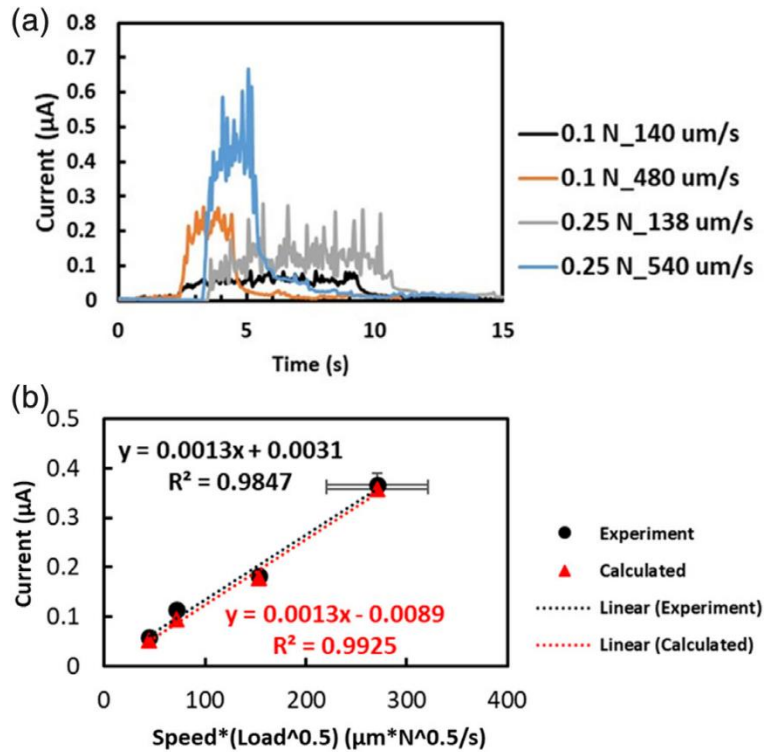


Fig. 4.8. a) Examples of single asperity diamond scratch currents at different loads and speeds. Baseline currents prior to scratching are followed by the scratches 1 mm long at different constant sliding speeds and normal loads, followed by a recovery to the baseline. b) Summary of average scratch test currents plotted against sliding speed times the square root of the load. Note that the black dot represents experimental results and red triangle stands for theoretical results based on the parameters from Table 2.4.

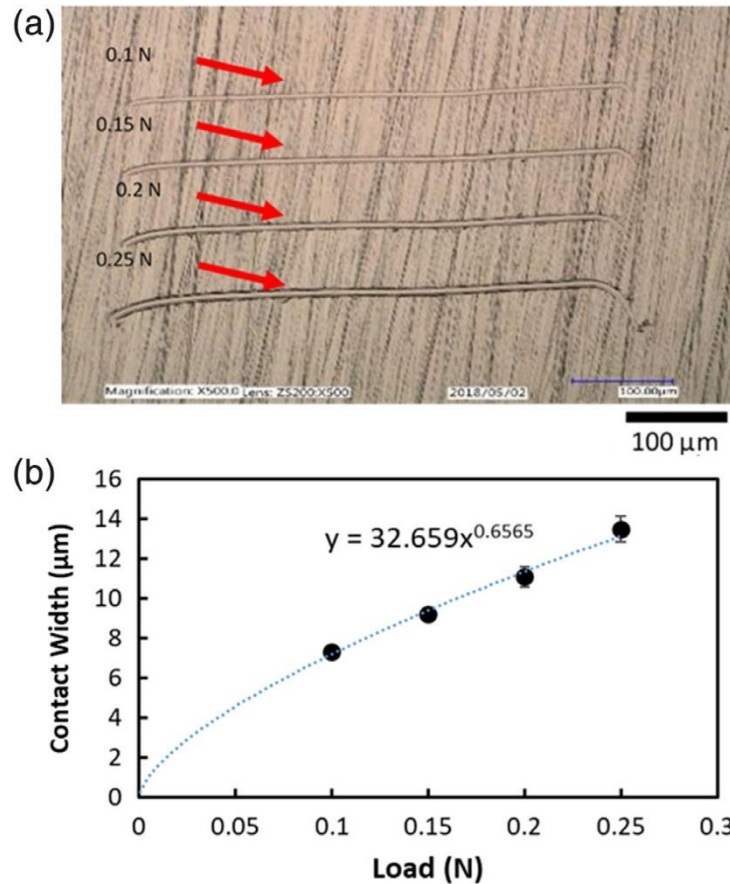


Fig. 4.9. Summary of optical micrograph measurement of scratch widths in CoCrMo surfaces under controlled loads using the diamond stylus. a) Digital optical micrograph of four scratches imparted by the 16 mm radius diamond stylus. b) Summary plots of scratch width versus applied load measured from the images (n=3). These values are consistent with the hardness used in the analysis.

The fretting current during the first 10 s of the single asperity diamond tip sliding experiments using sinusoidal or trapezoidal sliding waveforms shows that the model predicts the experimental current results under sine wave (Fig. 4.10a) and trapezoidal wave (Fig. 4.10b) sliding conditions using the measured fretting motion and the parameters from Table 4.5. The calculated and experimental results under both waveforms show excellent correspondence to one another and identified when sliding was occurring and not occurring.

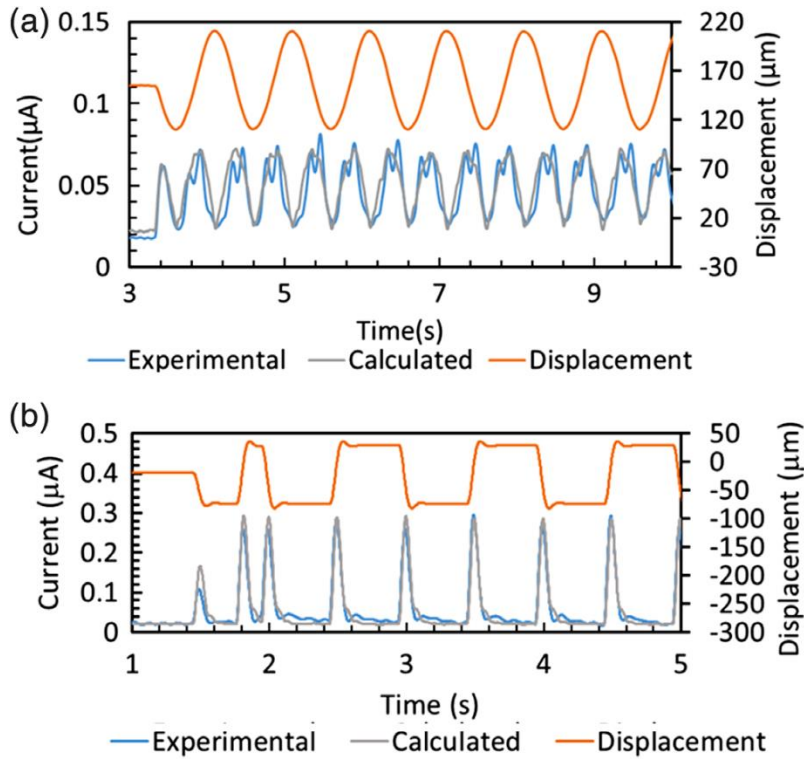


Fig. 4.10. Summary of experimental and calculated fretting current in (a) sine-wave and (b) square-wave. Note that the model well-predicted the fretting current behavior for sine wave. In both cases, the experimental and calculated currents are closely matched to each other showing the power of the model to predict the behavior.

Table 4.5. Parameters used for current calculation in different waveform and different solution

Parameter	Unit	Value
H	GPa	3
F_N	N	0.2
$\Phi(\rho n F / M w)$	C/cm ³	18400
τ	s	0.04
m	cm/V	0.0000002
E_o	V	-0.45

The average fretting currents obtained for PBS and DMEM with FBS from the experiment and the calculated currents were again very similar (Fig. 4.11a and 4.11b).

However, when proteins were present, the experimental currents were slightly smaller than the calculated currents and these were statistically significant ($p < 0.05$). However, the model still showed very similar trends of fretting current behavior for square waveform motion and peak currents close to (not different than) the experimental values were observed in PBS ($p > 0.05$).

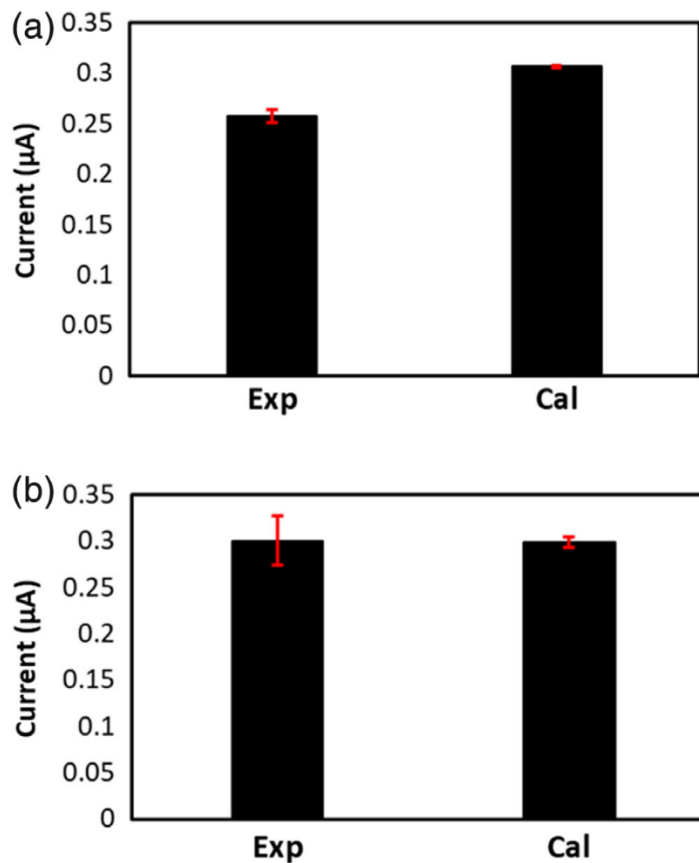


Fig. 4.11. Summary of average fretting current between 4 s to 8 s in (a) DMEM and (b) PBS. Note that there is a small significant difference between the experimental results and calculated in DMEM solution ($p < 0.05$), likely resulting from the proteins present in the solution modifying the contact conditions but there is no significant difference for PBS ($p > 0.05$).

4.5 Discussion

4.5.1. Major Findings and Implications

This study has presented a theoretical approach for predicting the tribocorrosion currents and electrode potential shifts associated with oxide film disruption and repassivation based on the contact mechanics, the oxide film growth and the impedance of the surface. The approach used two different heredity integrals (current-abrasion volume and voltage-current) which were coupled and iteratively solved to predict both the current-time and voltage-time behavior of the abraded electrode. The model incorporated asperity based hard-on-hard contact mechanics to describe the normal-force and hardness-dependent width of the fretted area, high field oxide growth concepts to estimate the oxide film thickness and its voltage dependence, and the measured sliding displacement-time behavior to predict the currents. The current-abraded volume analysis incorporated a tribocorrosion transfer function ($A^T(t)$) that described the exponential form of the instantaneous current response to a high-speed disruption event for an oxide film and its repassivation.

In addition, the electrode potential was predicted based on the currents and the impedance of the electrode which depends on electrode size. The two Duhamel integrals were solved simultaneously in a coupled numerical fashion so that updated voltages and currents could be fed-back into each of the integrals.

This approach was able to recapitulate the experimental response of CoCrMo fretting surfaces across a range of sliding frequencies, loads, sliding waveforms, and solutions using a fixed set of materials, mechanical and electrochemical parameters. The current waveform was reproduced with high similarity to the experimental currents and

the electrode potential drop, and the details of the potential-time waveform (for low frequencies) were accurately captured with this approach.

In addition, the average potential shifts, average current and rms current variations with frequency were also reasonably reproduced with this approach. Interestingly, the fretting currents (both experimentally and theoretically) showed the rms currents to increase and then decrease with increasing frequency (see Figure 4.6). This effect is due to the time constant for repassivation impeding the ability of the system to respond to oxide film disruptions. Overall, the theoretical approach was able to reasonably predict the experimental response based on the measured sliding displacement-time behavior, although not for every condition.

This model provides several important insights into tribocorrosion behavior of CoCrMo (and other electrochemical systems with passive oxide films). First, it appears that the currents generated by abrasion and repassivation, which were calculated based on several first-principle concepts, are close to those currents measured in the electrode system used in these experiments. While the zero-resistance ammeter, which captured the currents in the experimental section, may not detect all electrochemical currents (i.e., some reduction likely occurs at the abrading electrode), and there are likely currents associated with ionic dissolution not accounted for in this model, it was, none-the-less, possible to reproduce the currents and potentials measured over time based on oxide film disruption and repassivation only.

4.5.2 Impedance-Based Tribocorrosion Potential Variations

Another important prediction of this model is that the extent and time-course of the electrode potential observed during tribocorrosion was governed by the tribocorrosion processes, but also the impedance characteristics of the electrode. This concept has been described in detail in a recent publication by our laboratory [110] and this work further supports the predictive capability of this approach. Here, the electrode impedance consists of a resistive element, related to the kinetics of the cathodic reactions, and a capacitive element associated with charge accumulation at the interface. The approach in this study was to utilize a lumped parameter model where R_{ox} and C_{ox} are electrode-area-averaged values. Alternative descriptions of the resistive and capacitive elements representing the surface have been presented previously that can incorporate Mott-Schottky capacitive behavior, Tafel resistive behavior and other more representative models [110]. However, while these alternative model systems could be adapted to this approach, this work used a single set of resistance and capacitance values when analyzing all of the different frequency responses. Importantly, the potential responses observed demonstrated the time course for low frequency (drop-recovery per cycle) and high frequency (smooth exponential drop) behavior reflective of the capacitive effects on the electrode surface and they were similar in the overall changes seen over the 25 s experiments conducted. The exception was the 10 Hz results where the predicted voltage drop was less than observed.

There is currently no other mathematical model that can predict such potential-time variations without inclusion of the capacitive nature of the surface. Such cyclic drop and recovery behaviors are not explained simply by cathodic faradaic processes without

inclusion of the charge accumulation and consumption process that is inherent in the impedance model.

Future work will investigate the role of distributed impedance elements over a surface and the role of solution resistance and local impedance distributions on the associated current density distribution and the local potential distribution resulting from such models which will result in an equivalent lumped impedance response to the overall electrode.

It should be understood that the oxide repassivation anodic processes must be balanced by associated reduction reactions where the currents (averaged over time) must be equal, and that the reduction reactions that return the current to the electrode surfaces are likely governed by Tafel behavior (or Butler-Volmer based behavior), this requirement for equal anodic and cathodic currents (i.e., mixed potential theory) does not instantaneously hold, but rather holds averaged over time. In fact, the capacitive character of the electrode (as described by the impedance of the electrode) will serve as a storage system for charge and allows for transient conditions where oxidation currents are not necessarily balanced every instant in time with the reduction currents. These transient imbalances will affect the time course of potential drops and recoveries and thus the capacitive character of the film plays an important role in this process.

Thus, one can make several predictions of how the electrode's potential will be affected by tribocorrosion and electrode area. For example, larger electrode areas result in larger capacitances and smaller resistances. Therefore, potentials will not drop as much with larger electrode areas, and the time constant ($R_{ox}C_{ox}$) will affect the rate at

which the potentials can change with time either during tribocorrosion or during recovery after abrasion. When sliding frequencies are much higher than the reciprocal oxide time constant, $1/\tau$, there is not enough time for the potential to exhibit an exponential recovery after each sliding event and the potential-time plots become smooth and non-oscillatory.

The impedance values used in the heredity integrals were maintained fixed over all tests analyzed but were also selected by a manual best fitting of the 0.5 Hz (test 1) data. The actual impedance values measured by EIS for this electrode area were in the range of $R_p = 3.5 \times 10^6 \Omega \text{cm}^2$, $C = 1.25 \times 10^{-5} \text{ F/cm}^2$, however these were obtained using a Constant Phase Element Randles' circuit model with the CPE exponent was about 0.935. These values were close to, but not identical with the values used in this analysis. This is, in part, because the R_p measurement had high uncertainty associated with it (10%). The impedance values chosen resulted in reasonably close correspondence with the experimental results but were less accurate for the 10 Hz results (underestimating the potential drop). If the experimentally measured impedances were used in the analysis, then the high frequency data would be more closely matched, while the lower frequency data would have greater deviation from the experimental results.

The solution resistance element in this lumped parameter approximation of the electrode was assumed to be small compared to the oxide film resistance and therefore not significantly affecting the overall currents or potential excursions observed. Sensitivity analysis of the response of the model to different solution resistances found that R_s needs to approach about 1% of R_p (i.e., 20000 Ω) in order to have a noticeable effect on the potential response.

4.5.3 Mechanical Factors

Other factors that may have influenced the analysis of the current-volume abraded heredity integral include the smoothing of the displacement-time data. With no smoothing performed, the noise in the δ vs t plots would result in large and highly variable numerical derivatives even when there was no sliding taking place. This would have the effect of raising the currents (since they depend on $d\delta/dt$) when no sliding was taking place. By smoothing the data, the derivatives (noise) would be reduced and would more closely approximate the actual motion taking place.

The hard-on-hard asperity contact area surface mechanics concepts used in this study appear to do a reasonably good job at predicting the true sliding contact area and effective diameter for abraded area. Several observations result from this understanding of the asperity-based contact condition. First, the true area of contact does not depend on topography in these hard-on-hard surfaces. Rather, because all surfaces have some level of roughness, the true area of contact is a fraction of the nominal contact area. Prior fretting corrosion studies of head-neck modular taper junctions in orthopedic implants show that the typical currents that arise from fretting are in the microamp range. This analysis shows that for $1 \text{ mm}^2/\text{s}$ of area abrasion rate, the current generated will be $37 \text{ }\mu\text{A}$ (assuming a 2 nm thick oxide film). The nominal contact area of a 12/14 modular taper, 11 mm long, in a head-neck junction is about 450 mm^2 . The amount of area actually abraded that would induce $1 \text{ }\mu\text{A}$ of current is about $2.7 \times 10^{-2} \text{ mm}^2/\text{s}$. The associated contact area for such an abrasion area is about 5.7 mm^2 , or about 1.3% of the nominal area. This implies that only a very small area of the modular taper surface experiences

fretting corrosion reactions at any point in time for fretting corrosion currents of this magnitude.

Another important consideration here is that, while this study has focused on fretting corrosion, where small scale cyclic motion was occurring, the approach presented is equally applicable to other tribocorrosion processes, including wear of bearing surfaces where abrasive countersurfaces or particles, if they breach the passive oxide film, will also generate tribocorrosion currents as repassivation occurs. These wear-corrosion processes will also affect the electrode potential of the overall electrode altering the repassivation processes that may subsequently take place.

4.5.4 Area-Dependent Impedance Effects

The area dependence of the potential drop associated with fretting corrosion is also worth some comments. These potential changes may impact both the biology and the surface oxide film. For example, the smaller the overall electrode area exposed, the greater will be the drop-in potential resulting from a similar abrasion event. The more negative the potential drop, the thinner the oxide that reforms. This can have effects on the frictional interactions, where it has been demonstrated that the fretting coefficient of friction for CoCr/Ti interfaces is highly dependent on electrode potential [101]. In addition, negative excursions in potential, and the increased reduction reactions that are associated with these drops can induce biological effects [122-126], thus the size of the electrode available to engage in the reduction reactions *in vivo* is an important consideration in terms of potential adverse local tissue reactions that may arise.

4.5.5 Limitations of the Study

There are several limitations in this study. First, this approach does not account for longer-term changes that may arise in fretting junctions as a result of accumulated damage, oxide debris buildup or other factors (e.g., surface plastic deformation effects, local solution chemistry changes, etc.) that may locally alter the overall surface mechanics or electrode response. For example, if oxide debris accumulation acts like a solid lubricant at the interface thereby reducing the passive film abrasion, currents will decrease. This model does not deal with these effects. It also does not attempt to address other local effects like the high resistive paths that may develop within the fretting crevice interface which may locally alter reactions taking place, or changes in hardness of the surface with deformation. However, these issues may be addressed by using local area impedance characteristics and/or other evolutionary finite element methods.

4.6 Conclusions

This study has presented an analytical approach to determine the time course of currents and potentials associated with tribocorrosion processes and to provide a basis for understanding a number of electrode behaviors and effects. The use of heredity integrals, and the physics and chemistry of passive oxide films, contact mechanics and electrochemical impedance allows detailed predictions of both the current and electrode potential behavior during tribocorrosion processes. The coupled heredity integral equations for current and potential provide a theoretical foundation upon which modeling of tribocorrosion processes can be made. The model was compared to a series of well controlled fretting corrosion and single asperity sliding experiments on CoCrMo alloy

surfaces and were shown to reproduce the resultant current and potential behavior with a high degree of similarity. While there were some assumptions made in this model in terms of chosen parameter values, it is based on first principals of high-field oxide growth, hard-on-hard contact mechanics, the concepts of electrochemical impedance, and the superposition principles associated with Duhamel integrals. The novel coupled integration of the two Duhamel integrals allowed for determination of both current and potential over time. This model is well suited for discretization and finite element analysis of taper contact mechanics.

5. Fretting Initiated Crevice Corrosion of 316LVM Stainless Steel in Physiological Phosphate Buffered Saline: Potential and Cycles to Initiation [90]

5.1 Introduction

AISI 316L stainless steel (an austenitic Ni, Cr, Mo containing steel) has been widely used as a metallic biomaterial for implants (e.g., bone plates, bone screws, hip stems and cardiovascular stents) due to its excellent mechanical properties, corrosion resistance and reasonable cost [127-128]. Stainless steel owes its corrosion resistance to a spontaneously-formed oxide film on its surface [129-130]. However, the surface oxide of stainless steel is highly dynamic under physiological conditions [131-132]. Crevice corrosion and pitting corrosion have been reported to result in removal of stainless steel implants within 2 months [133]. During corrosion, metal ions and debris are released into surrounding tissues, which may cause inflammation [134], implant loosening [135], pseudotumor [136], particle-induced osteolysis [137] and mechanical fracture [138], leading to failure of implants.

Fretting corrosion refers to the conjoint mechanism of fretting (small scale, less than 100 μ m relative motions between two opposing faces), and electrochemically-based corrosion of the passive film and underlying alloy. It occurs in a variety of medical devices, including hip implants with modular designs such as modular head-neck designs, acetabular component designs and headneck/neck-stem taper dual modular designs [139-140]. Recently, fretting crevice corrosion (also called mechanical assisted crevice

corrosion, MACC, [139]) has been associated with modular tapered hip implants and has become a serious concern for metallic biomaterials [141-142]. The mechanism of fretting crevice corrosion of metallic biomaterials has been well studied in recent years [143–146]. Mechanical disruption of oxide films generates repassivation currents as the oxide film reforms and significantly increases the corrosion rate of metallic implants through the instantaneously breached oxide prior to repassivation. However, these studies, for the most part, have not demonstrated a sustained ongoing crevice corrosion reaction when the fretting ceases, but rather that the currents recover to pre-fretting levels. That is, the crevice corrosion aspects of MACC have not been well studied or reproduced in the laboratory.

Crevice corrosion is a form of localized corrosion of a metal surface at the gap or crevice between two joining interfaces. It is well known that stainless steels are more susceptible to crevice corrosion than to pitting corrosion [147]. Crevice corrosion behavior of stainless steel has been studied for many years. Different mechanisms, including the passive dissolution model [148-149], the IR drop theory [150-151], and the metastable pitting mechanism [147,152] have been proposed to explain the initiation of crevice corrosion under various conditions. Although no single mechanism alone is able to explain all crevice corrosion phenomenon, solution chemistry [153], surface potential [154] and crevice geometry [155] have been identified as key factors in crevice corrosion.

It is well known that fretting motion and crevice geometries simultaneously exist at implant interfaces. However, the relationship between fretting and crevice corrosion is still poorly understood for these alloys and geometries. A few studies hypothesized that

fretting accelerates or leads to crevice corrosion of stainless steel in modular hip tapers [156-157]. Previous spinal device testing in our lab showed that run-away crevice corrosion of stainless steel in spinal devices can be triggered by fretting at potential as low as -50 mV (vs Ag/AgCl/KCl (saturated)), which is -300 mV more negative than normal critical pitting potential for stainless steel [158]. This suggests the mechanism of fretting-initiated crevice corrosion is fundamentally different from that of fretting corrosion alone, crevice corrosion alone or a simple combination of both. To date, no systematic study has been conducted to investigate the mechanism of fretting initiated-crevice corrosion. Therefore, the goal of this study is to investigate fretting initiated crevice corrosion (FICC) behavior of stainless steel in physiologically representative saline solution in an in vitro pin-on-disk fretting corrosion model.

The voltage-dependent fretting corrosion behavior of stainless steel pins in contact with stainless steel disks immersed in a physiologically representative phosphate buffered saline was studied. Fretting corrosion experiments were conducted to understand both the mechanical and electrochemical conditions (potential, fretting cycles, crevice) needed for FICC using a customized pin-on-disk fretting corrosion system. Critical potentials for FICC, including triggering crevice corrosion, metastable crevice corrosion and developing of self-sustained crevice corrosion, were identified. Propagation of FICC on stainless steel with time was investigated. In addition, a customized 2-D pin-on-disk fretting corrosion system, interfaced with a digital optical microscope was used to directly observe, in real time, the surface contact geometry and corrosion product generation during fretting and crevice corrosion.

5.2 Materials and Methods

5.2.1 Materials

The pins and disks used in the experiments were sectioned from 316 LVM Stainless Steel (ASTM F138-13) (Chemical composition Fe: balance; C: <0.03%; Cr: 17%; Ni: 14%; Mo: 2.6%; Mn: 2.0%; Si: 0.5%; N: 0.1%; S: 0.01%) rods and were in annealed condition. Pins were cone-shaped with a nominally flat, but slightly convex bottom which had a nominal contact area of about 1.2 mm². However, the true contact area depended on normal load and material hardness and would occur in one locally proud region of the pin. The true contact area of pin on disk was about 40–50 μm in diameter and the immediately-adjacent area consisted of a small crevice region that increased in gap space across the crevice region with distance away from the contact region. This gave a well-defined contact point and local crevice region for the tests to occur. The solution used was PBS (phosphate buffered saline) (Sigma, P3813, 0.135 M NaCl, 0.0027 M KCl, 0.01 M Na₂HPO₄ and 0.002 M KH₂PO₄) solution and is representative of the buffered isotonic saline of the body.

5.2.2 Methods

5.2.2.1 Varied potential tests

Varied potential fretting corrosion tests were conducted on a customized 3D fretting corrosion system. Details related to 3D the pin-on-disk fretting corrosion system were described elsewhere [143]. In the 3D fretting corrosion system (Fig. 5.1a), fretting motion (typically 20 μm) was controlled by a high load piezoelectric actuator (Piezosystems Jena, Germany). The electrochemical chamber, where the disk was

mounted, was fixed to an X-Y linear stage (Newport Corporation, Irvine, California, US) and connected to the piezoelectric actuator. Linear Z-stage with micrometer screw to adjust the loading arm was designed to achieve the vertical load control. A multiaxial load cell (MINI 45 F/T, ATI Industrial automation, Apex, NC, US) was mounted under the loading arm and to which the pin sample was attached to measure instantaneously the normal and frictional loads. A high resolution ($1\mu\text{m}$) contact DVRT (Micro-Epsilon, Raleigh, NC, US) was used to obtain relative displacement on the pin-on-disk interface to capture the fretting motion. Pins and disks were prepared through sequential wet sanding to a 600 grit finish, cleaned with ethanol and distilled water. Surface roughness of pin and disk were measured by contact mode Atomic Force Microscope (Dimension ICON AFM, Brukers, Billerica, MA, US) on $2 \times 2\ \mu\text{m}$ scan area. The exposed disk area was circular, fixed at $0.25\ \text{cm}^2$ and controlled by covering the remaining disk area with transparent tape (Scotch™, 3M, Maplewood, MN, US). The pin and disk samples were rigidly mounted in the fretting corrosion system. Electrochemical tests were conducted using a three-electrode system where the pin-disk couple was the working electrode, Ag/AgCl/KCl (saturated) reference electrode and carbon rod was the counter electrode. All electrochemical measurements were obtained through a potentiostat (Solartron 1280C, AMETEK Scientific Instruments, Berwyn, PA US). Mechanical and electrochemical data was acquired using a National Instruments™ data acquisition card (NI PCI-6229, US), Labview™ program tool and CorrWare™ software. Fixed normal load (2 N), fretting frequency (1.25 Hz) and fretting displacement (20–30 μm) were controlled by the 3D fretting system. All potentials in this study are with reference to the

Ag/AgCl/KCl (saturated) reference electrode potential. The potential of the working electrode was varied from -700 mV to 250 mV with an increment of $+50$ mV or 100 mV between each voltage. Twelve different potentials were tested on different samples. Potentiostatic tests were conducted at each voltage for 1 min to equilibrate the sample surface baseline currents before initiating the fretting and the current was recorded. Fretting was performed for 120 s at each voltage and the fretting currents were determined by the deviation of the current from the baseline during fretting. After fretting was stopped, the baseline current was continually captured for 300 s and used to determine if there was ongoing fretting-initiated crevice corrosion before the pin was lifted from the disk to separate the crevice surfaces. Current after the separation of pin and disk was recorded until it returned to the baseline current level.

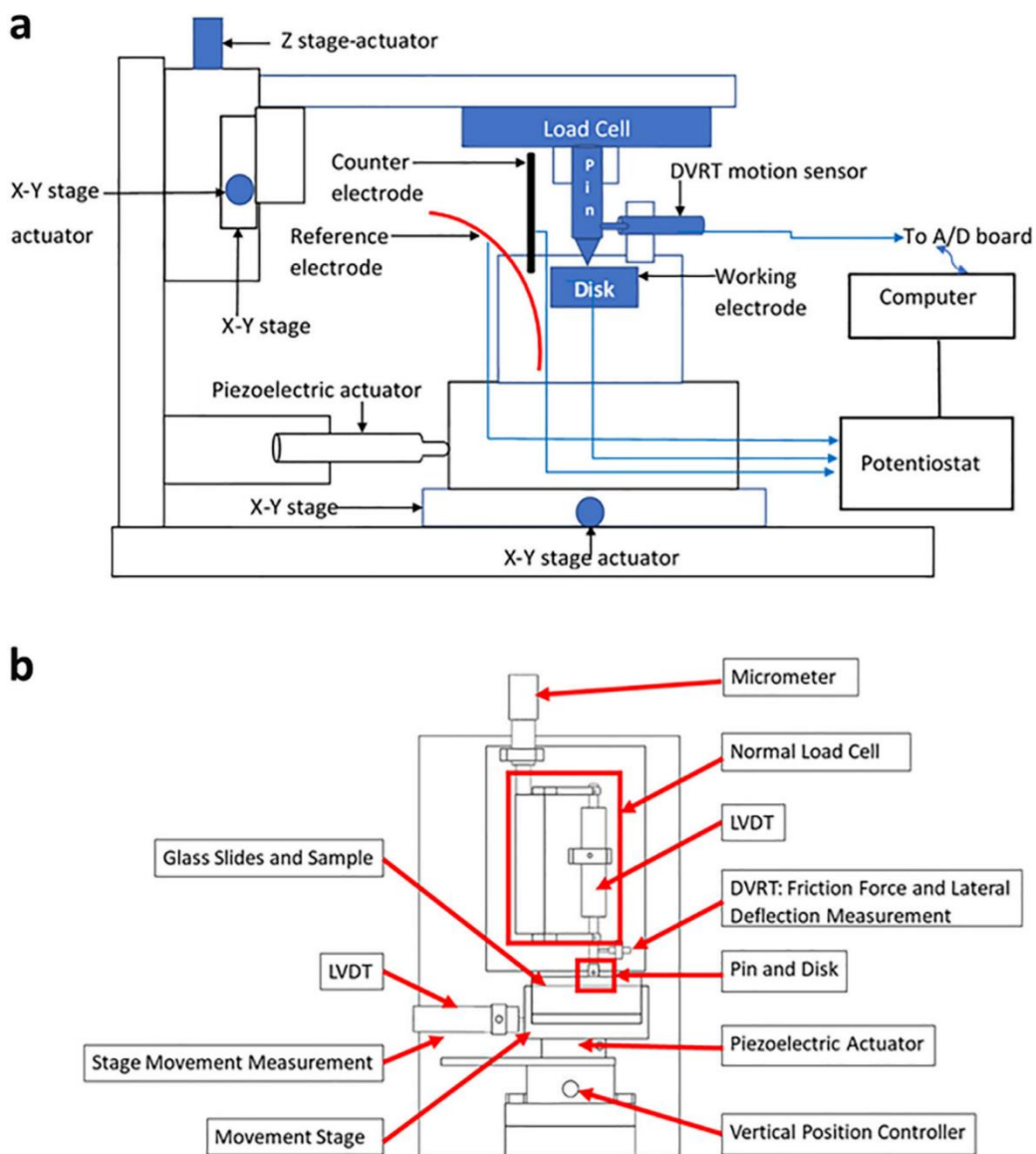


Fig. 5.1. Schematic of a) 3D and b) 2D fretting corrosion systems.

5.2.2.2 Surface morphology and element mapping

Damage induced at the fretting interface was investigated using a Scanning Electron Microscope (SEM, Hitachi 3700, Tokyo, Japan), Energy Dispersive X-Ray

Spectroscopy (EDS, Oxford Instruments X-Max, United Kingdom) element mapping and the Digital Optical Microscope (Keyence VK-8700, Itasca, IL, US). Depth profiles of crevices and corrosion features were measured and documented using the quantitative 3D image capture capabilities of the digital optical microscope. Tapping mode in AFM was used to image the surface near the boundary between corroded and non-corroded areas on samples after FICC at 250 mV. Height sensor, amplitude error and phase images were captured.

5.2.2.3 2D fretting corrosion test and visualization of the fretting crevice interface

A custom-made 2D fretting corrosion test was developed not only to capture electrochemical and mechanical information simultaneously but also to provide visualization of the experiment (Fig. 5.1b) [159]. Both a regular cone-shape SS pin and a slice of SS sample was polished as 600 grit before putting into the system. A custom-made load cell, comprised of two cantilevers and a linear variable differential transformer (LVDT) (DC 750-50, Macro Sensors®, Pennsauken, NJ, USA), was used to measure the normal load applied on the contact surface. Another LVDT and a differential variable reluctance transducer (DVRT) (SN3327, microepsilon®, Raleigh, NC, USA) were responsible for collecting data of stage movement and lateral deflection of the pin (which is a measure of the frictional forces), respectively. The electrochemical chamber, which consists of two parallel glass slides, was mounted on a piezo actuator (Burleigh®, Middle Township, NJ, USA) that can provide 55 μm displacement. An amplifier (Burleigh PZ-300M, Middle Township, NJ, USA) and a function generator (FG-8002, EZ Digital, Seoul, South Korea) were used to perform fretting motion under controlled frequency.

Both pin and disk were submerged into PBS and held under a fixed potential relative to Ag/AgCl/KCl (saturated) using a potentiostat (Model 263, EG&G Princeton Applied Research, Oak Ridge, TN, USA). Fixed normal load (0.5 N), fretting frequency (1 Hz) and amplitude (55 μm) were applied and controlled by the 2-D fretting corrosion test system under 250 mV. The fretting time was limited to 2 min. Pin and disk remained in contact after fretting stopped and then images of the fretting crevice interface were taken using the Digital Optical Microscope up to 30 min after the start of fretting.

5.2.2.4 Instantaneous triggering of stainless steel crevice corrosion

Tests of different fretting cycles (2 cycles to 120 cycles) were performed on the 3D fretting system to find the fewest number of fretting cycles required to initiate crevice corrosion at 250 mV. The loading and fretting conditions were the same as those in the varied potential tests.

5.2.2.5 Crevice propagation tests

Tests of different immersion times, after fretting was stopped, were conducted on the 3D fretting corrosion system to investigate how fretting initiated crevice corrosion propagated with time at 250 mV using the same load conditions as in varied-potential tests. Corrosion damage of the surfaces over different FICC times (1 min, 15 min, 90 min) were observed under digital optical microscopy to explore the progression of the crevice corrosion damage of the surface.

5.2.2.6 Cyclic potentiodynamic anodic polarization

Cyclic polarization test started from a potential 100 mV lower than the open circuit potential and performed in positive potential direction to 1000 mV higher than the

starting potential with a scan rate of 10 mV/min scan rate. Then, the scan direction was reversed to negative potential direction until it reached the starting potential to form a hysteresis loop.

5.2.3 Post-tests data analysis

In all results, tests were repeated at least 3 times. Only representative plots are presented, however, the behavior observed is consistent across repeated testing. Frictional force was plotted versus DVRT displacement to construct a fretting load-displacement plot of tests conducted on the 3D fretting system. Crevice current was defined as the current before separating the pin and disk if crevice corrosion phenomenon was observed. Fretting current was determined by calculating the difference between the current during fretting and the baseline current either prior to or just after fretting ceased.

Analysis of variance (ANOVA) and post hoc comparisons (Tukey's method) were used. A one-way ANOVA statistic was performed to assess the effect of potential on fretting current. A plevel of 0.05 was considered significant in statistical analysis. The error bars in figures represent the standard deviation of related data points (3 samples were analyzed for each condition).

5.3 Results

5.3.1 Contact geometry

Details on contact conditions were revealed by digital optical microscopy imaging, AFM surface roughness measurement and fretting load-displacement analysis.

The disk was a flat surface, the pin consisted of a nominally flat, but slightly convex geometry (Fig. 5.2a) where the actual contact area (identified in Fig. 5.2a) was a small region associated with the convex pin. The surface roughness after 600 grit paper polishing measured by AFM before test were 31.7 ± 6.6 nm for disk and 19.8 ± 12.8 nm for pin ($2 \times 2 \mu\text{m}$ area). Digital optical microscopy image on pin after test shows the total diameter of contact was about $50 \mu\text{m}$ (Fig. 5.2b) and is on the order of or greater than the fretting sliding distance (about $20 \mu\text{m}$), illustrated by the fretting map (Fig. 5.2c). DVRT force vs. displacement curves show that the fretting was in the gross-slip regime.

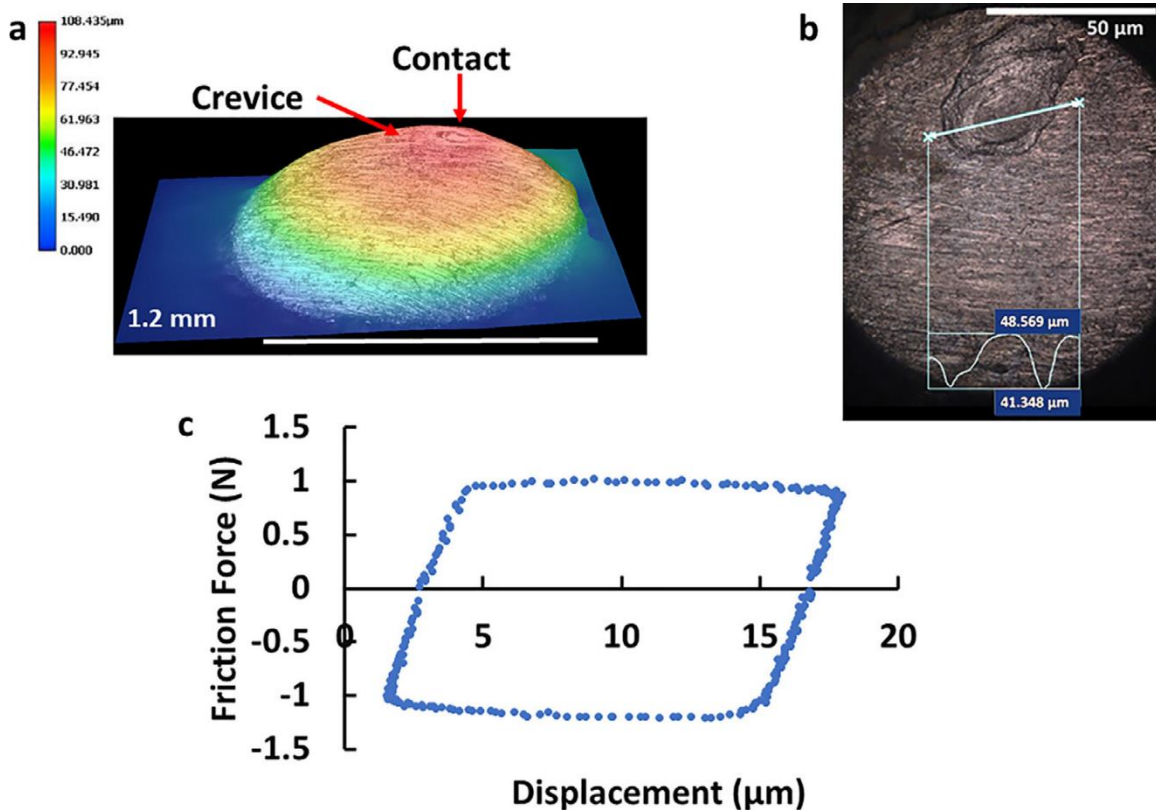


Fig. 5.2. a) 3D Convex geometry of pin by Digital Optical Microscopy, note the vertical scale is expanded to emphasize the slight convexity; b) Contact, crevice and depth profile features on pin surface after test; c) Fretting load-displacement plot for one cycle of fretting motion (nominal displacement of $20 \mu\text{m}$)

5.3.2 Varied potential tests

Fig. 5.3 shows representative current versus time data of fretting corrosion tests on stainless steel pin-on-disk samples in PBS solution at different potentials. Baseline current was recorded before fretting corrosion started at 60 s. Baseline current became more positive as potential rose from -700 mV to 250 mV (Fig. 5.3). Fretting occurred for about 120 s and was stopped, but the pin and disk remained in contact and under load. Lift off of the pin from the disk occurred at around 480 s and, for the higher potentials, the crevice corrosion ceased, and the current returned to the baseline level.

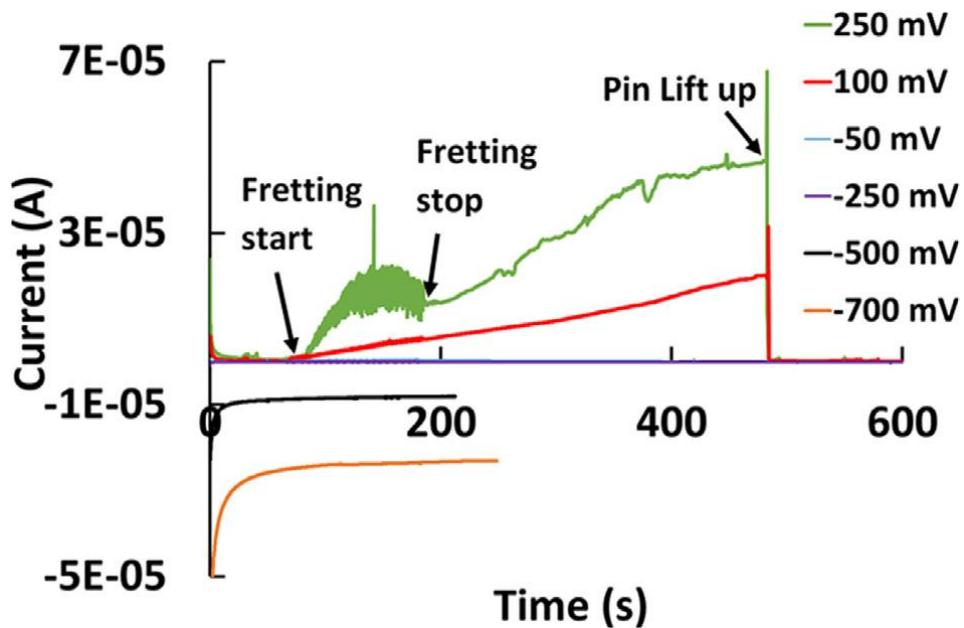


Fig. 5.3. Current profile during fretting corrosion tests at different voltages. Current during fretting corrosion became more positive as potential increases. Current continued to increase after fretting ceased at several positive potentials (eg.100 mV, 250 mV).

Fretting corrosion currents (anodic current excursions above the baseline currents) were observed only at potentials more positive than -500 mV and fretting currents during

fretting motion continued to increase as the potential increased positively above -150 mV (Fig. 5.4 a-d).

The current response after fretting ceased showed three domains of voltage-dependent behavior and current profiles were shown separately according to their domains (Fig. 5.4 a-c). These three voltage domains were: Domain 1) stable post-fretting recovery: -500 mV to -100 mV, Domain 2) metastable post-fretting currents: -100 mV to 0 mV, and Domain 3) unstable post-fretting currents: 50 mV to 250 mV (or higher). The current response in these three voltage-dependent domains are shown in Fig. 5.4a, 3.4b and 4c, respectively. In domain 1 (Fig. 5.4a), at potentials between -500 mV and -150 mV, fretting corrosion current was observed at potentials higher than -500 mV and these repassivation-based currents, due to oxide disruption and repassivation, increased with potential above -500 mV. However, these currents immediately returned to the static baseline current as soon as fretting was stopped. In domain 2 (Fig. 5.4b), at potentials between -100 mV and 0 mV, metastable FICC was observed, where crevice currents post fretting remained elevated but gradually recovered to baseline current after fretting motion. It is interesting to note that the currents remained increased over the baseline current after fretting ceased for between 1 and 3 min before they started to recover (Fig. 5.4b). In domain 3 (Fig. 5.4c), at potentials from 50 mV and higher, a self-sustained unstable fretting-initiated crevice corrosion was observed after fretting stopped. In the unstable domain (domain 3), currents continued to increase even after fretting motion was stopped. It should be noted that fretting-initiated crevice corrosion currents immediately recover to the baseline current once the pin was separated from disk at the

end of the test in all circumstances, indicating that it was, indeed, the crevice conditions that sustained the corrosion reactions. The relationship between fretting current (current generated only due to fretting motion rather than formation of crevice) and potential is shown in Fig. 5.4d. Potential has a significant effect on fretting current of stainless steel ($p < 0.0001$). Fretting currents exhibited an increasing trend as the potential became more positive. Fretting current at 250 mV ($2.35\mu\text{A}$), which is the difference between the total current during fretting and the current immediately after fretting stopped, was significantly higher ($p < 0.005$) compared to other conditions (under mA level).

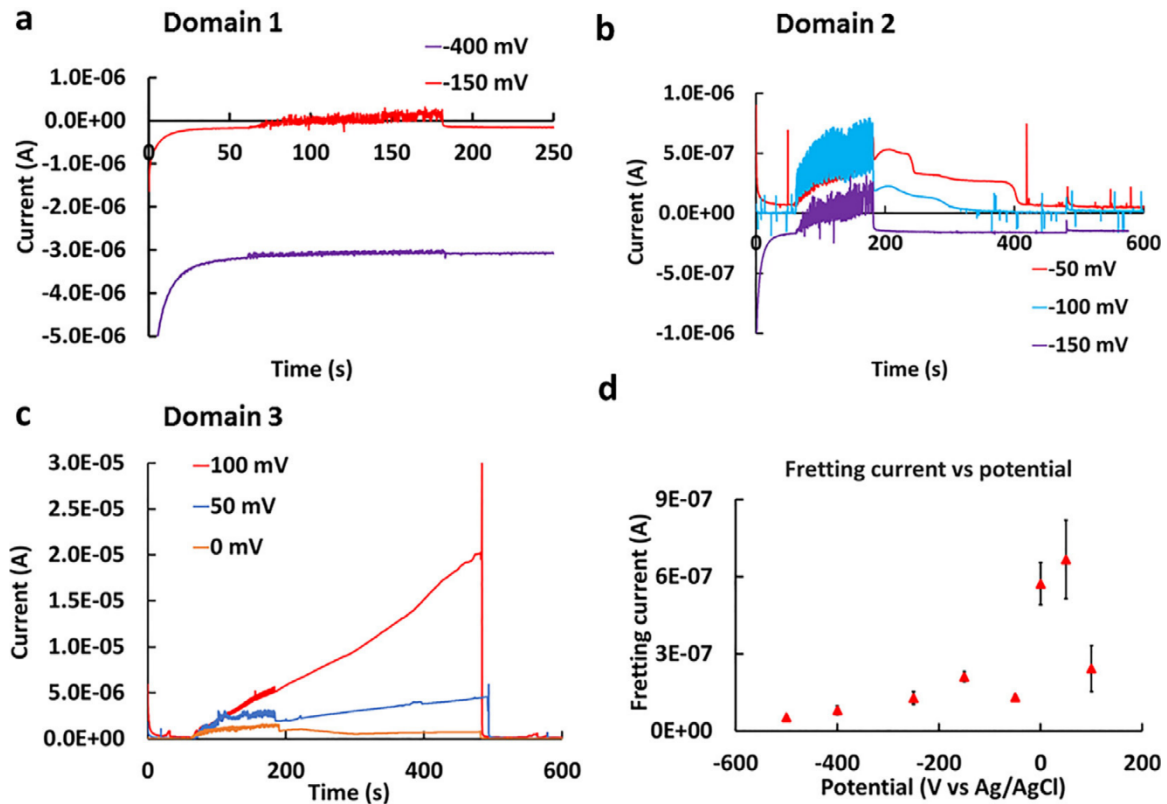


Fig. 5.4. Potential-dependent regions of fretting corrosion and FICC behavior of 316 SS. a) Representative fretting corrosion current in potential regions (-500 mV to -150 mV) with no FICC (stable); b) Metastable FICC started at -100 mV ; c) Unstable FICC initiated at potentials above 50 mV ; d) Potential-dependent fretting corrosion currents occurred at potentials higher than -500 mV .

5.3.3. Surface morphology and element analysis

5.3.3.1 SEM

Fig. 5.5 shows representative SEM images of stainless steel surfaces after fretting corrosion tests at potentials from -150 mV to 250 mV where there was FICC. The fretting contact region and the direction of cyclic motion were identified, and voltage-dependent corrosion damage corresponding to the measured current profiles were observed. At potentials more negative than open circuit potential (Fig. 5.5a, -150 mV), only a light fretting scar and plastic deformation from a few hundred cycles applied was observed while no significant corrosion damage was shown. At potentials higher than -150 mV, pitting corrosion was observed (Fig. 5.5b). Crevice corrosion regions (Fig. 5.5d & 5.5e) featured severe damage at the edge of the crevice boundary when the potential was 50 mV or above (Fig. 5.5d & 5.5e). This crevice region became deeper at more positive potentials (100 mV, 250 mV) and grew with time. It should be noted that the fretting contact area was less corroded compared to adjacent areas within the crevice and forms a 'fretting island' (where fretting scar was clearly shown) at center of the crevice corrosion area (Fig. 5.5e).

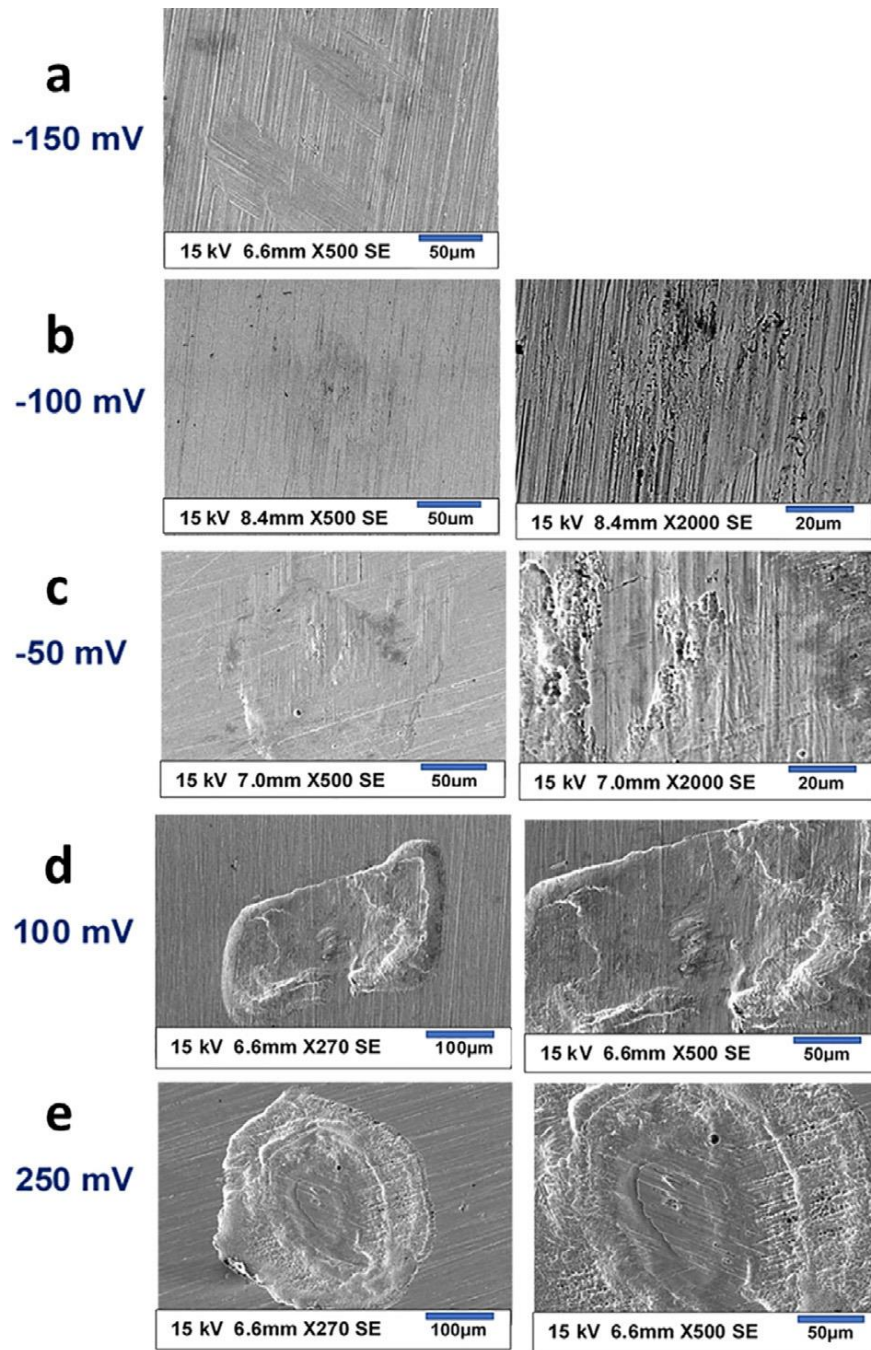


Fig. 5.5. SEM images of fretting contact regions after tests at different potentials. a) At -150 mV and below, fretting scars were shown but no pitting damage; b) Pitting started at -100 mV, where FICC initiated; c) Corrosion damage became more severe as potential increased to 50 mV and above; d, e) Unstable FICC at 50 mV and potentials above.

5.3.3.2 EDS element mapping

Fig. 5.6 shows EDS elemental mapping of the fretted area after fretting crevice corrosion in PBS at 200 mV. SEM/EDS layered images reveal the fretting contact area, crevice corrosion region and a halo of surface-adhered chemistry outside of the crevice corrosion area. Elemental mapping at low voltage (6 kV) shows a chromium and oxygen accumulation zone just outside of the crevice corrosion area where the pin ends. In contrast to the distribution of chromium and oxygen, iron and nickel were depleted in the halo region. Chloride and phosphate were relatively evenly distributed with perhaps a small accumulation of both within the halo region. These results imply that Cr-Oxide and/or Cr-phosphates were precipitated and adhered to the surface just outside of the crevice region.

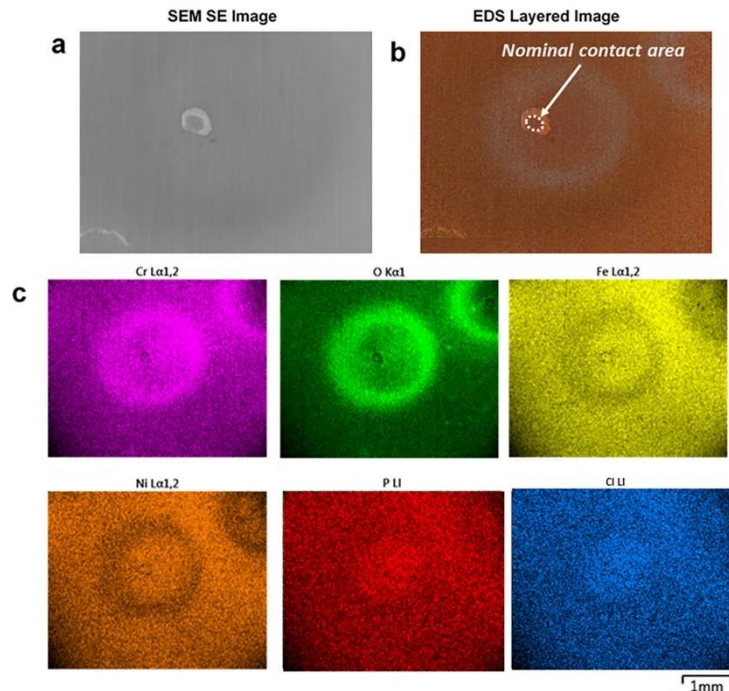


Fig. 5.6. Element mapping of surface after FICC at 200 mV by low kV (6 kV) EDS. a) SEM secondary electron image shows fretting contact and crevice region; b-c) A halo region was featured by enrichment of Cr and O at the edge and depletion of them within and an increase in the chloride and phosphorous levels within.

5.3.3.3 AFM imaging at crevice boundary

Fig. 5.7 shows a set of tapping mode AFM images ($50\mu\text{m} \times 50\mu\text{m}$) of the surface at the boundary between the crevice area (corroded area, left) and non-corroded area (right) on a stainless steel sample after fretting corrosion at 250 mV and 300 s of FICC. The boundary between the crevice corrosion attacked region and the outer uncorroded region is shown (Fig. 5.7a & 5.7b). Small degradation particles at the sub-micron scale were observed. Surface damage inside corroded area exhibited linear directional features (Fig. 5.7c, arrow) reflective of the microstructure of the alloy. Small particles and the surface at the boundary exhibited different phase image features compared to the rest of the area while the surface inside the crevice and non-corroded area show similar phase image signal (Fig. 5.7d). This phase variation is likely due to differences in surface adhesion and modulus response between corrosion particles and the underlying alloy surface.

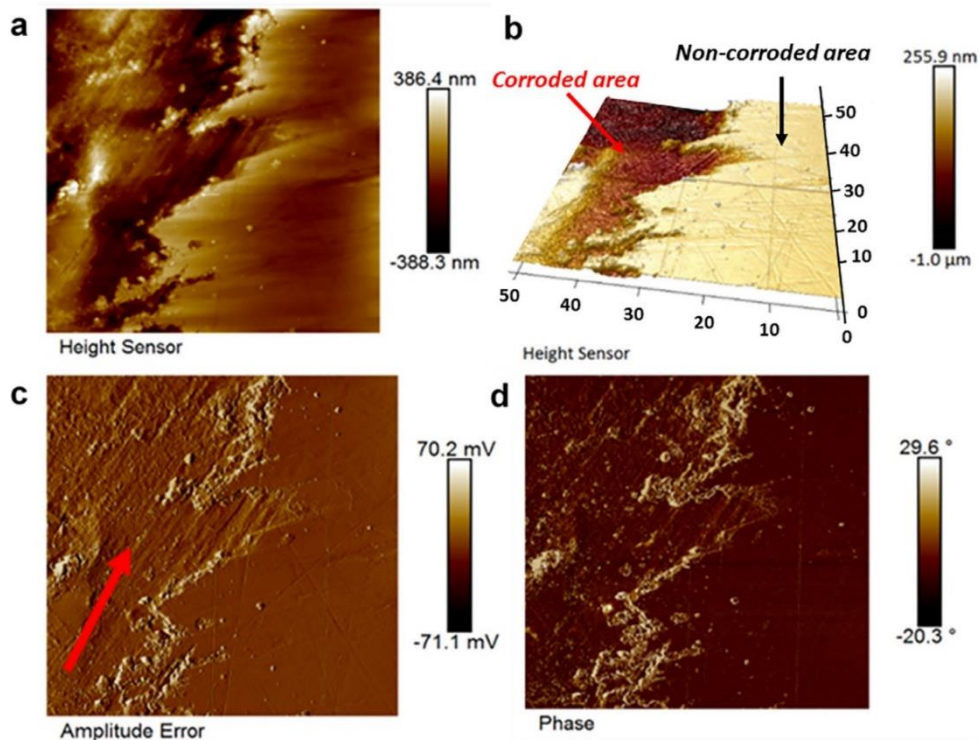


Fig. 5.7. AFM tapping mode images ($50 \times 50 \mu\text{m}^2$) of surface after FICC test at 250 mV. a, b) 2D and 3D height sensor images shows $1 \mu\text{m}$ depth at corroded region; c) Amplitude error image d) Phase image.

5.3.4 In-situ observation of FICC by 2D fretting corrosion system

In-situ observations of fretting-initiated crevice corrosion of the contact interface between pin and disk (Fig. 5.8) using a 2D pin-on-disk fretting corrosion system shows the contact geometry and crevice formed (Fig. 5.8a & 5.8b). Here, thin sections of 316L stainless steel pin and disk are covered by a thin layer of electrolyte over top of the contact and constrained above and below by glass slides so that imaging was possible. The real pin-on-disk nominal contact region (flat-bottomed, slightly convex pin and flat disk), the location of the fretting contact region within the nominal pin-disk contact, and the interposed crevice can be clearly identified. It was observed that the real contact

region was relatively small (on the order of 40 to 50 μm diameter) compared to the total pin area. The experiment was conducted at 250 mV and the fretting motion lasted for 2 min (Fig. 5.8c). Images of the pin-on-disk interface at different time points, after fretting ceased and crevice corrosion continued, were captured. The brown and cloudy solution emanating from the interface was due to generation and transport of crevice corrosion products and the area of this feature became larger and more intense with time corresponding to the increased currents observed.

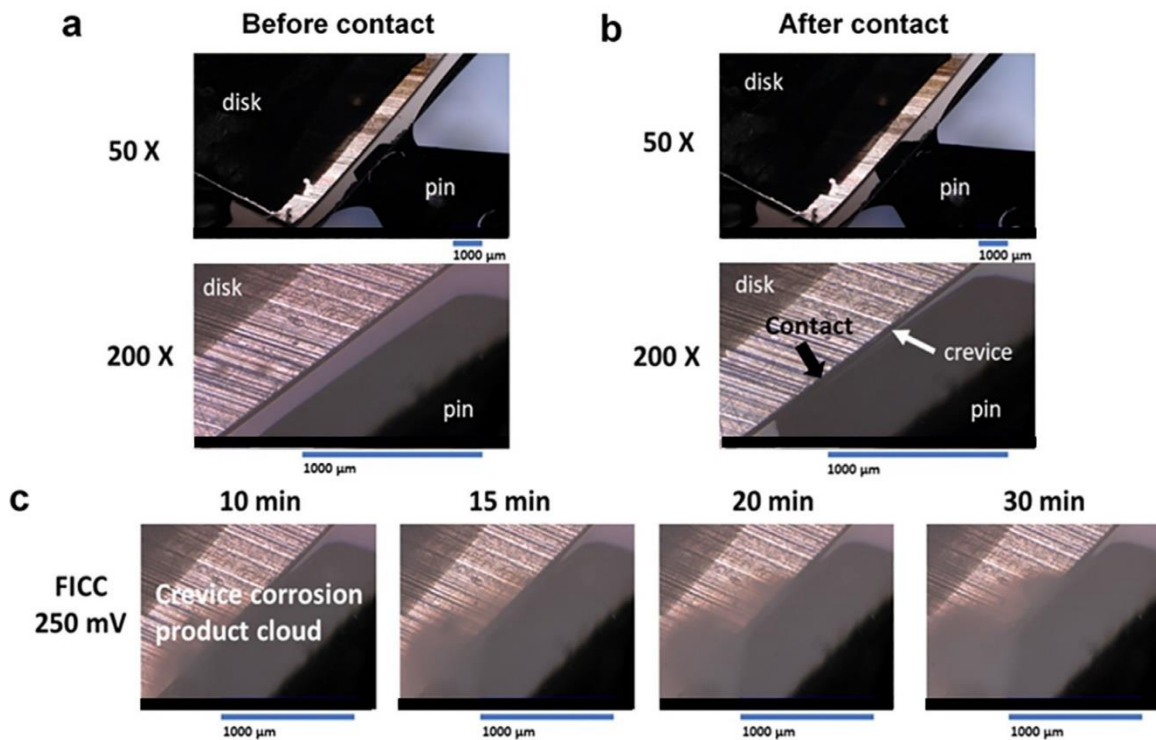


Fig. 5.8. a, b) 2D pin-on-disk interface before and after fretting by digital optical microscopy and c) Pin-on-disk interface after initiation of crevice corrosion at different time points at 250 mV.

5.3.5 Instant triggering of FICC

Fig. 5.9 shows the current vs time profile (Fig. 5.9a), 3D and depth imaging (Fig. 5.9b and 5.9c) and cross-sectional height profile (Fig. 5.9d) results on a disk after a fretting-initiated crevice corrosion test at 250 mV where only two seconds of fretting were applied followed by about 300 s of crevice corrosion reaction. The results reveal fretting-initiated crevice corrosion can be triggered by fretting motion within 2 s at the stainless steel interface under these conditions of potential and crevice geometry. Continued increase of the corrosion current indicates an increasing, unstable, self-sustained crevice corrosion process is ongoing where the area corroding increases with time. The 3D image exhibits a relatively large (400 μ m diameter) crevice region, which has concentric circular surface damage features, around the fretted area (center of target area). The depth profile shows a ‘fretting island’ feature at the center of the crevice where pin contact was made with a deeper damaged surface at the edge of the crevice. Similar corrosion features have been observed on the pin as well (Fig. 5.2b).

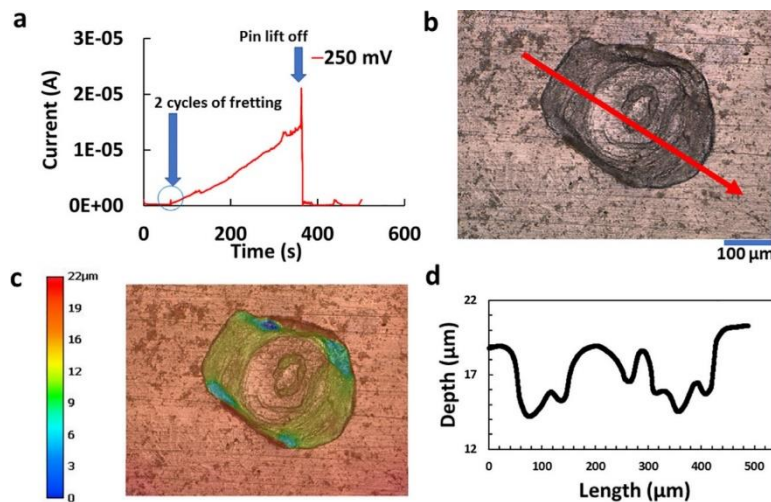


Fig. 5.9. a) Current profile of FICC induced by fretting within 2 s. b) Circle-by circle crevice feature. c) Depth profile across the crevice surface. d) Digital optical microscopy depth analysis of surface damage (corresponding to red line in 5.9b).

5.3.6. FICC propagation

Fig. 5.10 shows 3D digital microscopy images and depth profiles of the fretted and crevice corrosion area at 1 min, 15 min and 90 min after fretting for 10 s at 250 mV. Propagation of fretting-initiated crevice corrosion with time was observed. Significant increase of corrosion width and depth was observed as self-sustained crevice corrosion continues from 1 min to 90 min. Volume loss at 1 min was 0.07 mm^3 and increased to 1.54 mm^3 and 34.44 mm^3 after 15 min and 90 min, respectively. The ‘fretting island’ feature at the center of the crevice was clearly identified by the depth profile and 3D imaging. It is interesting to note that the severity (depth) of corrosion increases as the distance to the center of fretting area becomes larger. At the edge of the crevice, corrosion depth was the largest, which was in agreement with the results from SEM (Fig. 3.5).

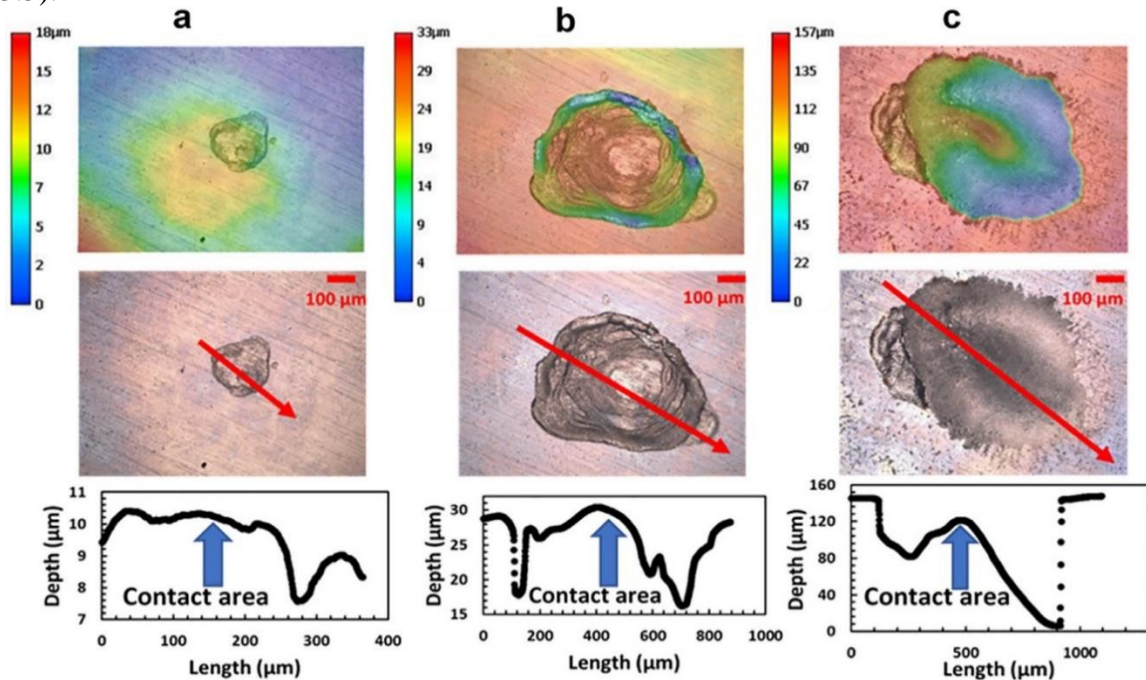


Fig. 5.10. 3D imaging and depth profile analysis of crevice corrosion area after 120 s of fretting and different FICC times (a.1 min, b.15 min, c. 90 min) at 250 mV.

5.3.7. Cyclic polarization

Fig. 5.11 shows a cyclic potentiodynamic polarization curve of stainless steel in PBS. A hysteresis loop showing pitting corrosion behavior of stainless steel was seen. Pitting potential of the passive layer was found to be at 450 mV and the protection potential was -120 mV.

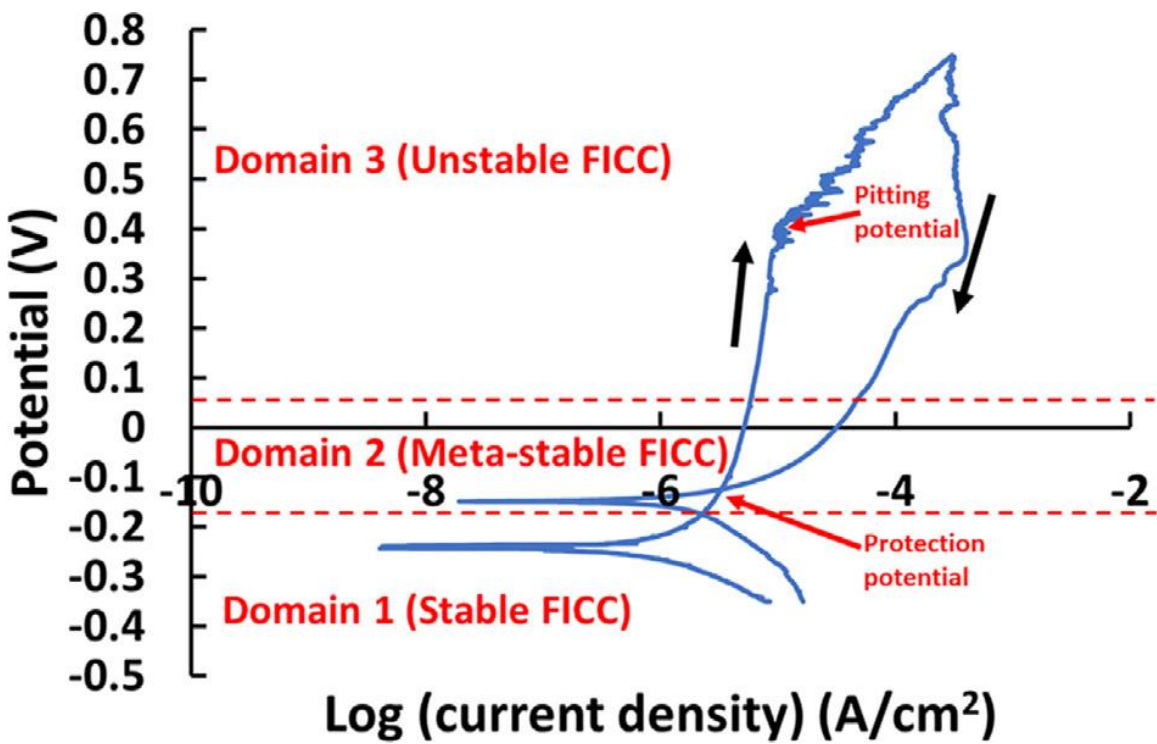


Fig. 5.11. Cyclic potentiodynamic polarization curve of stainless steel.

5.4 Discussion

The goal of this paper was to systematically assess the fretting initiated crevice corrosion behavior of 316L stainless steel used in medical device applications. It was

shown that fretting can initiate crevice corrosion rapidly at potential close to resting open circuit potential conditions in PBS. As little as two seconds of fretting motion was found to be able to trigger immediate and self-sustained crevice corrosion at 250 mV, a potential 200 mV below the normal pitting or breakdown potential of stainless steel (Fig. 11). Both pitting corrosion and crevice corrosion can be induced at potentials as negative as -100 mV by way of fretting crevice corrosion. Mechanical and electrochemical factors influencing fretting-initiated crevice corrosion were investigated. Fretting motion (fretting cycles), surface potential, crevice geometry was found to play important roles in initiation and propagation of crevice corrosion.

5.4.1. Triggering of crevice corrosion

Crevice corrosion of stainless steel has been studied for many years. It has been shown that the initiation of crevice corrosion of SS is potential-dependent and there is a critical potential and incubation time for crevice corrosion to start for a specific crevice geometry and Cl^- concentration condition. Szklarska-Smialowska et al. found that the crevice corrosion potential for 316 L SS is 250 mV (vs Ag/AgCl) in 1 M NaCl and it increased to 400 mV when the Cl^- concentration decreased to 0.5 M [154]. Aoyama et al. reported the critical potential for crevice corrosion initiation on polycarbonate/steel crevice specimens was 250 mV in 1 M NaCl and corresponding incubation time for crevice corrosion was 23 ks (6.5 h) while no crevice corrosion was observed at 200 mV [160]. Our study showed that the critical crevice corrosion initiated by fretting motion was as negative as -100 mV while the crevice corrosion started within 120 s at Cl^- concentration of 0.14 M. Fretting motion dramatically shifted the critical potential to a

more negative value and decreased the incubation time for crevice corrosion at much lower chloride concentration. At 250 mV, fretting-initiated crevice corrosion was triggered within 2 s, more than 10,000 times faster than the initiation of crevice corrosion reported by Aoyama et al. [160]. Thus, the susceptibility of 316 SS alloy to crevice corrosion was significantly increased by fretting (even with just a couple of cycles). Fretting-initiated crevice corrosion of stainless steel doesn't follow the critical potential, chloride concentration and incubation time criteria of crevice corrosion, indicating fretting is the dominate factor in the triggering process and in developing the local solution conditions (e.g., deaerated, increased Cl-ion concentration) necessary to continue crevice corrosion in the absence of fretting.

5.4.2. Potential-dependent FICC domains

Three potential-dependent FICC domains were identified in this study (Fig. 5.11): Domain 3: unstable FICC (above 0 mV), Domain 2: metastable FICC (−150 mV to 0 mV) and Domain 1: stable fretting with no FICC (below −100 mV). Metastable FICC was observed at potentials close to the open circuit potential (−100 mV) and the protection potential for 316L stainless steel in PBS. Increases of potential from open circuit potential to a positive range transformed meta-stable FICC to an unstable, self-sustained FICC. As potential became more positive, FICC was easier to trigger and propagated faster.

This is due to the potential-dependent behavior of both fretting corrosion and crevice corrosion. Previous studies show that the fretting corrosion behavior of CoCrMo alloy and titanium alloy is potential-dependent [143,144,161]. Oxide film thickness,

chemistry and structure of metallic biomaterials vary with potential and influence both the passivation behavior and contact mechanics (e.g., coefficient of friction) at the metal interface [162]. Meanwhile, it's widely known that crevice corrosion behavior is potential dependent. Potentiostatic studies by Yang et al. show that the induction stage of crevice corrosion of stainless steel is highly dependent on applied potential [163]. Potentials of 0.5 V (vs SCE) induced immediate crevice corrosion while a delayed initiation of crevice corrosion was observed at 0.3 V (vs SCE). Thus, shifts of potential to more positive potentials increase the tendency of crevice corrosion, decreases the incubation time and leads to a more rapid increase of current during the crevice propagation stage.

5.4.3. FICC mechanism

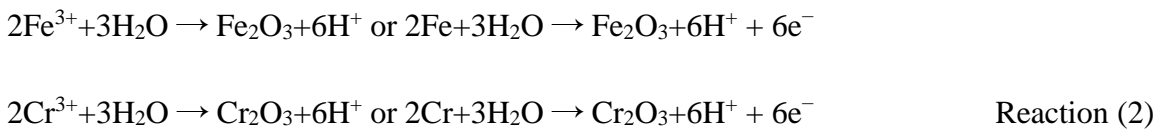
Fretting-initiated crevice corrosion behavior of stainless steel in this study could be described, in part, by the critical crevice solution theory and fretting corrosion model [143,147]. Before fretting, the metal surface consisted of a passive oxide film at the conditions tested (-100 mV to 250 mV in PBS used in this study). As such, the kinetics of oxidation are limited by the presence of the passive film, even in the presence of a crevice. Crevice conditions include the local deaeration of the crevice solution and the ingress of chloride ions in order to balance any excess metal ion levels that may accumulate within the crevice geometry, thereby generating metal chlorides and hydrolyzing water to liberate hydrogen ions lowering the pH. However, in most cases with passivating alloy surfaces, the oxide film limits the rate of the oxidation reactions relative to oxygen transport in and metal ion transport out and hinders the development of

crevice corrosion processes. With fretting, however, these kinetic barrier effects are intermittently eliminated, and rapid oxidation can occur dramatically altering the rates of deaeration, chloride accumulation, water hydrolysis and metal ion release into the crevice.

The anodic reactions are the dissolution of metals (Fe, Cr, Ni), for example:



Hydrolysis of metal ions occurs when metal ion concentrations reach a level, or metal oxide passive films are formed directly from the metal surface:



It should be noted that these reactions occur and are enhanced in the presence of chloride ions and result in metal chloride intermediates and ultimately the hydrogen ions are associated with hydrochloric acid generation within the crevice. The metal oxides may also be in a hydrated form (metal-hydroxides).

The cathodic reaction is typically thought to be the oxygen reduction reaction:



It should be noted that the metal dissolution is slow when open circuit potential is below the critical crevice potential, which makes initiation of crevice corrosion difficult. However, instantaneous removal of oxide film by fretting leads to immediate oxide film repassivation through Reaction (2) and also hydrolysis by released metal ions. These reactions cause a rapid pH to decrease within the crevice in the presence of chloride.

While oxygen is consumed inside the crevice, the majority of the oxygen reduction (Reaction (3)) occurs outside of the crevice and electroneutrality leads to Cl^- ion migration into the crevice. When the environment within the crevice reaches a critical crevice solution (CCS) condition (oxygen depletion, pH decrease and Cl^- migration), the passive film breaks down leading to generalized corrosion within the crevice [147]. Thus, by cyclically abrading the oxide film, fretting motion significantly facilitates the development of critical crevice solution conditions, lowering the critical crevice potential and decreasing the initiation time for crevice corrosion.

5.4.4. Fretting corrosion behavior

It has been shown that compared to the crevice corrosion current at the end of FICC test, the fretting current (current induced by fretting motion only) was smaller (Fig. 5.3c & 5.3d), and thus corrosion damage was mainly caused fretting-initiated crevice corrosion rather than the fretting corrosion itself. It should be mentioned that the fretting current only occurs at potentials higher than -500 mV, which indicates that protective oxide film formation potential is about -500 mV for stainless steel. At potentials more negative than -500 mV, no protective oxide film is formed on the stainless surface after abrasion, thus fretting motion will not generate anodic currents.

5.4.5. Surface morphology

The optical microscopy analysis revealed development of an 'island' feature at the junction of the contact region for fretting with the crevice. This island remained intact for most of the crevice corrosion observed but was lost with extended time of crevice corrosion. This indicates that the tight crevice contact region may be too small and

limited to allow crevice corrosion processes to occur. Over time the crevice attack resulted in an increasing size of the corroded region with deeper corrosion depths at the outer perimeter of the crevice where the crevice edge was the most severely corroded (Fig. 3.9d penetration depth) and the center of the crevice was less attacked. The center of the damaged region was where the real pin-on-disk contact area occurred and was much smaller than the total pin area available. More severe corrosion near the crevice mouth has been reported in a previous study and can be explained by the IR drop mechanism [163]. A large IR drop near the crevice has been shown to bring the localized potential just down to the active region at the edge of the crevice. At the center of the corroded area the surface potential in the active corrosion region decreases as the IR drop increases, leading to smaller currents [151]. Faster corrosion at the edge of the contact zone during wear testing was reported by Geringer et al., where a 'W' shape of wear track was observed at the beginning and gradually changed to a 'U' shape as crevice corrosion propagated, similar in appearance to what is observed here [144,164]. Crevice geometry has been shown to play a vital role in the initiation and development of stable crevice corrosion [155,165,166]. Researchers have shown that a critical crevice mouth value is needed for crevice corrosion to occur [165]. Lifting the pin from contacting the disk immediately stopped FICC in this study as the crevice solution was diluted with external solution. Propagation of crevice corrosion with time was observed starting at the crevice adjacent to the fretting contact region. One interesting question is how far and how deep this crevice corrosion area can propagate. No crevice corrosion exceeded the pin area, so it is likely that this may limit the effect. In addition, the crevice gap between

pin and disk increased with distance away from the contact region and this gap distance may also play a role in the corroded metal geometry. Long-term FICC experiments are planned to answer this question.

5.4.6. Surface element distribution

Element mapping shows a Cr and O (and P) enriched halo outside of the crevice, indicating there were Cr ions migrating from inside the halo and reacted with O₂ at the halo. The diameter of the halo (1.2 mm) is similar to that of the pin. This indicates that depletion of O₂ and hydrolysis of Cr³⁺ occurred outside of the crevice under the pin area and the pH under the pin area might be lower than bulk solution outside. It is also interesting to notice that there was depletion of Fe and Ni at the halo compared to Cr. The reason for this is due to preferential precipitation of Cr-oxides and Cr-Phosphates compared to Fe and Ni oxides [167].

5.4.7. Clinical relevance

This study has shown that fretting initiated crevice corrosion may be a significant potential concern for stainless steel implants. More than 90% of stainless steel failures are caused by crevice corrosion and pitting corrosion [138]. Severe corrosion damage on retrieved stainless steel spinal implants, hip implants and fixation plates have been reported [168-170]. These implants are susceptible to fretting motion at interfaces that typically arise (screw countersinks, implant bone or implant cement interfaces, etc.), where fretting corrosion can trigger fretting-initiated crevice corrosion.

Corrosion of stainless steel leads to release of metal ions such as Cr and Ni [171]. Ni ion is highly toxic and Cr ion is known to be associated with adverse local tissue

reaction, allergens and cause damage to DNA [172]. Stainless steel plates used for fixation have been shown to trigger marked immuno-inflammatory reaction in the tissue surrounding the implants in some cases [134]. *In vivo* solution chemistry is more complicated, reactive oxygen species (ROS) and iron related Fenton reactions may create more aggressive corrosion environment for metallic biomaterials [173]. Study of stainless steel in simulated inflammatory conditions has shown that inflammatory species such as H₂O₂ increases oxidizing power of solution and can cause localized crevice corrosion and severe pitting corrosion [174-175]. Evidence of inflammatory cell-induced corrosion has been reported [176-177]. Corrosion causes inflammation while inflammation may induce and accelerate corrosion. Interaction between inflammation and corrosion may form a positive feedback loop *in vivo* and may lead to further degradation of implants and unwanted biological reactions. Crevice corrosion, once triggered by fretting, can be self-sustained and rapidly propagates. It may also be an important element in inducing immune-inflammatory reactions of patients with SS implants.

There are several limitations of this study. First, it is important to better understand the critical crevice solution chemistry required to sustain crevice corrosion. Knowledge of the constituents and concentration within the crevice was not determined in these experiments and is a critical piece of information to understand the process. Second, the earliest processes of fretting initiation of the crevice conditions could be better understood if the damage regions created immediately after initiation were captured and studied. Finally, the specific crevice geometry was not fully controlled other than to have a small contact zone under a nominally flat, but slightly tapered geometry.

How this geometry affects the initiation process is another important parameter to consider.

5.4.8. Future study

Crevice corrosion was initiated by fretting at open circuit potential level, -100 mV, PBS, which has low Cl^- concentration. Future studies are planned to investigate the FICC behavior of stainless steel under freely corroding conditions. Our study shows that the critical potential for self-sustained FICC was below the open circuit potential of stainless steel in simulated inflammatory conditions [174]. Thus, self-sustained FICC may be expected to occur without applying external potential under inflammatory conditions. It has been shown that the local solution chemistry may be a critical driving force for crevice corrosion once it has been established. It is of interest to design experiments to better understand the chemistry of both the solution inside the crevice and that under the pin region. Protein plays an important role on the electrochemistry of metallic biomaterials [178-179]. Thus, study on how protein affects FICC will provide valuable information on how stainless steel metal implants degrade in vivo. Meanwhile, it is important to understand how the chemistry of the passive oxide film changes locally due to FICC. Micro-Raman spectroscopy and X-ray photoelectron spectroscopy study are planned.

Another interesting area worth exploring is how the variation of potential and crevice geometry affects initiated FICC. Once triggered under potentiostatic conditions, assuming the local chemistry has reached the critical crevice corrosion condition, is it necessary to keep the potential at the same level for FICC to propagate? Future studies

will illustrate the roles potential and solution chemistry play in propagation of crevice corrosion. Also, with precision control of the vertical crevice dimension, experiments investigating the critical crevice gap needed to sustain crevice corrosion will be explored. Studies of FICC of CoCrMo and titanium alloys are planned for the future. These alloys exhibit evidence of such sustained crevice corrosion reaction *in vivo*, however, to date, no similar generation of fretting-initiated crevice corrosion has been documented *in vitro* in a controlled fashion as demonstrated here with stainless steel. This is a significant gap in our understanding of the processes of mechanically assisted crevice corrosion and needs to be addressed.

5.5 Conclusions

This study has demonstrated the process of fretting-initiated crevice corrosion in 316L stainless steel in simulated physiological solution of phosphate buffered saline. The key findings were summarized below:

- Crevice corrosion can be induced by fretting motion at potentials as low as -100 mV in PBS.
- Self-sustained crevice corrosion of stainless steel can be initiated instantaneously by as few as 2 cycles of fretting motion at 250 mV in PBS.
- FICC causes pitting corrosion on stainless steel in PBS at -100 mV and -50 mV adjacent to the fretting contact region.

- Three different FICC domains were identified, including no FICC, metastable FICC and unstable, self-sustained FICC domains. The critical potential for self-sustained FICC is above 0 mV.
- FICC initiates at the fretting contact region and propagates away from the fretting contact-crevice interface where the corrosion damage increases in size and depth with time.

These findings indicate fundamental differences between the FICC mechanism and conventional crevice corrosion theory, showing that fretting can play a significant role in the initiation of crevice corrosion of stainless steel.

6. Fretting Corrosion of Si₃N₄ vs CoCrMo Femoral Heads on Ti-6Al-V

Trunnions [58]

6.1 Introduction

Metallic alloys of cobalt chromium and titanium have been used in total hip arthroplasty (THA) for decades because of their biocompatibility, mechanical properties, and corrosion resistance. All metallic implants corrode to some extent, creating the risk of adverse reactions to degradation products [180-182]. Metal implant degradation is typically a combination of electrochemical corrosion and mechanical wear [183]. Fretting corrosion is one form of mechanically assisted corrosion that is associated with small scale cyclic displacements (<100 μm) between hard-on-hard interfaces. As a result of fretting corrosion, metal ions and metal-oxide particles released into the periprosthetic tissue/fluid may lead to cytotoxicity, tissue necrosis, osteolysis, adverse immunological reactions, hypersensitivity, and pain [184-188].

Implant modularity is one of the most popular ways to achieve off-the-shelf flexibility to accommodate individual patient needs intraoperative. As with other hard-on-hard interfaces, the head-neck modular interface is susceptible to fretting corrosion [189-192]. As cyclic micromotion is unavoidable at the modular junctions, alternative femoral head materials such as ceramics have been investigated to reduce the wear/corrosion associated with cyclic loading. Specifically, alumina (Al₂O₃) and zirconia-toughened alumina (ZTA) have shown biocompatibility and resistance to

taper corrosion and have become standard replacements to avoid metal-on-metal contact at the head-neck interface [193-195]. Balancing this advantage is the negligible risk of catastrophic brittle failure of ceramic femoral heads [196].

Silicon nitride (Si_3N_4) is a biocompatible material that has a successful track record in cervical and thoracolumbar spine fusion [197-199]. Boschetto et al., studied the metabolic responses of ZTA and Si_3N_4 to *Staphylococcus epidermidis* and found that the surface buffering effect slowed bacterial proliferation on Si_3N_4 (relative to ZTA) [200]. Zhou et al., showed that silicon nitride had excellent wear properties when the mating surfaces were ultra-smooth [201]. Bal et al., reported low wear rates for Si_3N_4 femoral heads in a hip simulator test and explored the viability for Si_3N_4 femoral heads [202]. Si_3N_4 also possesses mechanical properties like high fracture toughness and high flexural strength which make it suitable for orthopedic applications as well.

However, most of the research so far on silicon nitride as an arthroplasty material has focused on the bearing properties, such that the fretting corrosion performance of Si_3N_4 against the commonly used Ti-6Al-4V necks has not been reported in the literature. The goal of this study was to investigate the fretting corrosion performance of Si_3N_4 head/Ti-6Al-4V neck modular tapers for THA and compare it to standard CoCrMo head/Ti-6Al-4V neck taper junctions. It is hypothesized that the performance of Si_3N_4 femoral head interfacing with Ti-6Al-4V stem would be better when compared to CoCrMo femoral head/Ti-6Al-4V stem in terms of fretting corrosion in both a short-term incremental fretting corrosion test and in a million-cycle test.

6.2 Materials and Methods

The two test groups consisted of CoCrMo (ASTM F-1537, high carbon wrought alloy) and Si₃N₄ femoral heads mated with cylindrical Ti-6Al-4V trunnions (12/14, 5°40' taper angle; n = 10 samples/group) [203]. The heads had identical form, feature, and taper tolerances (+8 mm offset, Ø32 mm external diameter, both produced by SINTX Technologies, Salt Lake City, UT). The trunnions were comprised of commercial-quality taper junctions with proper tolerances and surface made of 5 to 8 µm ridges separated by 100 µm intervals. The taper angle mismatch tolerance between the head and neck was the same for both groups and the throat engagement was typical for ceramic tapers (ie, the head angle was slightly larger than the trunnion). The engagement length for the head-neck tapers was approximately 11 mm as is typical for modular taper junctions [204]. A hydraulic mechanical testing system (MTS Model 515 HPU, MTS; Eden Prairie, MN) was used to apply cyclic loads to the head-neck construct and the test assembly with sample, environment, and electrodes is shown in Figure 6.1.

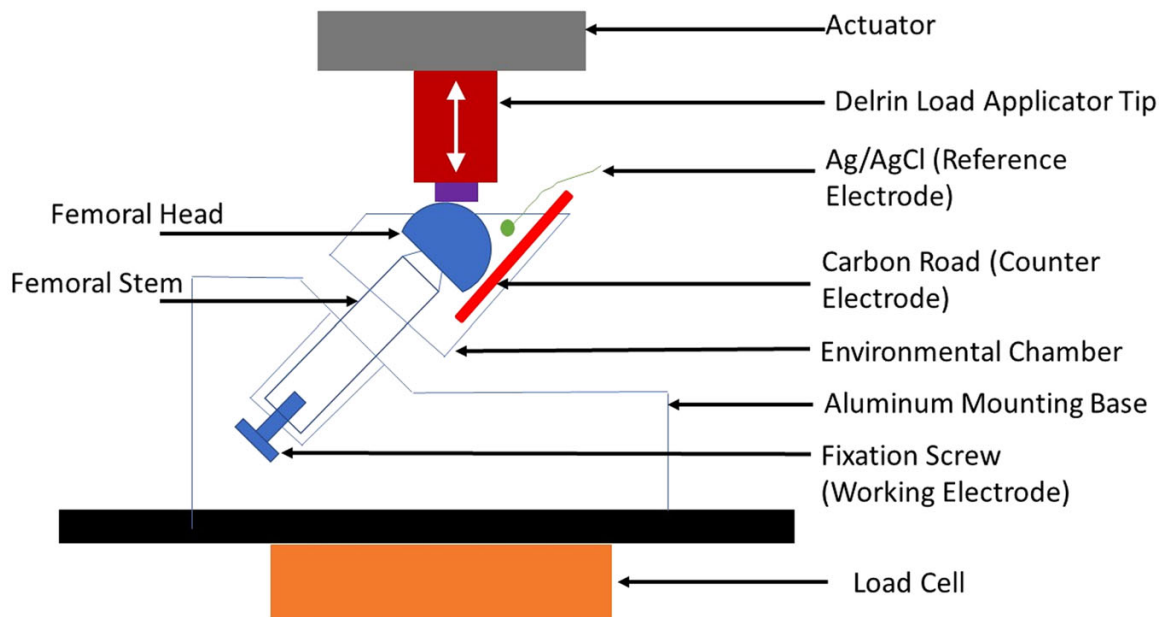


Fig. 6.1. Schematic of assembled femoral head-neck taper immersed in phosphate buffer solution with three electrochemical setups.

6.2.1 Static seating test

Phosphate buffer saline (PBS; Sigma-Aldrich, St. Louis, MO) was used to wet the head-neck interface prior to static seating. Wet assembly during seating was used to mimic the worst-case scenario for fluid ingress into the head-neck attachment. The presence of fluid also facilitated the measurement of corrosion currents. Seating of the tapers was performed by loading the head-trunnion construct axially. Starting at 50 N, the compressive load was increased at 100 N/s until a maximum load of 4000 N was reached.

6.2.2 Incremental cyclic fretting corrosion test

A previously developed incremental cyclic fretting corrosion (ICFC) test protocol was used to capture the load-dependent fretting corrosion response of head-neck tapers [205]. During ICFC testing, cyclic loads (3 Hz, R = 0.1, for 3 minutes) were applied

vertically to the head-neck taper construct. The construct itself was oriented with the neck axis at 35° from vertical (physiological orientation) as shown in Figure 1. The load started at 100 N and was increased in 100 N increments every 3 minutes until 1000 N was reached. It was then increased at 200 N intervals up to 4000 N. At the end of each load cycle, after a dwell of 20 seconds, the load was increased to the next level in 20 seconds. At the end of the test, the load was lowered to 50 N as illustrated by the drop in the force at the end of the test in subsequent figures. A three-electrode electrochemical setup with the trunnion and head as the working electrode, a carbon rod as counter electrode (CE) and Ag/AgCl as reference electrode was used to measure the fretting currents under potentiostatic conditions (-50 mV vs Ag/AgCl). This potential was chosen based on the stable resting (open circuit) potential of CoCrMo and Ti-6Al-4V alloys in PBS. The electrochemical cell was allowed to stabilize for 30 minutes before applying any load. During each 3-minute interval, fretting currents were measured by a bipotentiostat (Model AFRDE4; Pine Instrument Company, Grove City, PA), which was connected to a high-speed data acquisition system (NI USB-6210; National Instrument, Austin, TX). A custom LabVIEW program (National Instrument) was written to capture the data for 2 seconds (every 20 seconds) at 200 Hz.

6.2.3 One million cycle fretting corrosion test

Immediately following the ICFC testing, a long-term (one million cycle) fretting corrosion test was performed. The samples were loaded at 3200 N ($R = 0.1$) at 15 Hz and potentiostatically held at -50 mV (vs Ag/AgCl) while the fretting currents were captured

periodically over the 18 hours required to reach a million cycles. The fretting current and actuator displacements were captured using data acquisition methods to track the progression of fretting corrosion over time.

6.2.4 Pull-off test

At the end of the one million cycle test, the samples were subjected to a pull-off test (ASTM F2009) where the head-neck constructs were axially disassembled in a static tensile manner [206]. The pull-off testing was performed under displacement mode (0.05 mm/s) and the load was measured continuously during pull off. The pull-off force was the highest load measured right before disassembly.

6.2.5 Post-test analysis

After disassembly, the taper surfaces were imaged using a digital optical microscope (Keyence VK-8700; Itasca, IL) and a scanning electron microscopy (SEM; Hitachi S-3700N, Tokyo, Japan). Energy-dispersive X-ray spectroscopy (EDS; Oxford Instruments X-Max, UK) was used to investigate the corroded surfaces and material transfer between the head and neck components. Figure 6.2 shows the schematic of the sequential protocol used for the current study.

Student's t-tests were performed to assess statistical differences between the control and test group. The onset load for fretting, the average fretting current at a fixed load (3200, 3600 and 4000 N), the average fretting current over one million cycles and

the pull-off loads were compared between the $\text{Si}_3\text{N}_4/\text{Ti}-6\text{Al}-4\text{V}$ group and the $\text{CoCrMo}/\text{Ti}-6\text{Al}-4\text{V}$ group, with $p < .05$ considered a statistically significant difference.

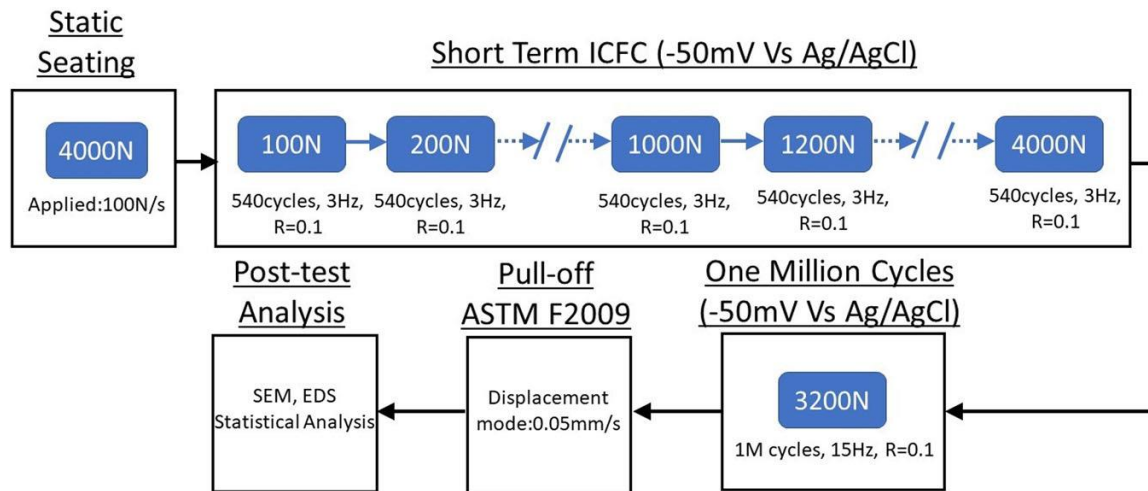


Fig. 6.2. Schematic showing the complete testing protocol including static seating, short term ICFC test, one million cycles test, pull-off and post-test analysis methodology.

6.3 Results

As the femoral head was seated on the trunnion, the measured displacement increased as the load was increased (loading cycle). During unloading, the displacement decreased but did not return to its initial zero value. This nonzero displacement after load removal, also called seating displacement, for the Si_3N_4 and CoCrMo heads was $115 \mu\text{m}$ ($\text{SD} = 29 \mu\text{m}$) and $123 \mu\text{m}$ ($\text{SD} = 40 \mu\text{m}$), respectively. The measurements included displacement of the actuator nose and other components which contributed less than $10 \mu\text{m}$ during the seating test. There were no statistically significant differences in seating displacement between the two groups.

Figure 6.3A shows the measured currents during a single ICFC test (CoCrMo/Ti-6Al-4V) as a function of time over 2 hours of testing. The baseline current, a measure of anodic dissolution at -50 mV vs Ag/AgCl, was established before any load application to the head-neck interface. The baseline was subtracted in subsequent analysis to obtain the true repassivation/fretting current (ie, the current measured above the baseline during cycling). After 30 minutes (1800 seconds), the testing protocol began with the application of 100 N normal cyclic load. When the applied cyclic load was low, the current did not change (indicating an absence of fretting). However, after a certain load, termed as onset-load, the captured current started deviating from the baseline (see black arrow, Figure 6.3A). Figure 6.3B shows an enlarged view of a smaller segment of the plot in Figure 6.3A. Each vertical bar in Figure 6.3B represents data captured during the 2 seconds interval and shows the fretting current response. Figure 6.3C is further enlargement of a section of Figure 6.3B and shows the typical cyclic behavior of the current during fretting corrosion due to oxide film abrasion and repassivation at head-neck taper junction. The biphasic nature of the current peaks indicated oxide abrasion/repassivation during both loading and unloading phase of the cyclic load. During dwell, the current dropped to the baseline before rising again at the start of the next loading increment (see Figure 6.3B). This drop confirmed the absence of fretting when no cyclic motion was present.

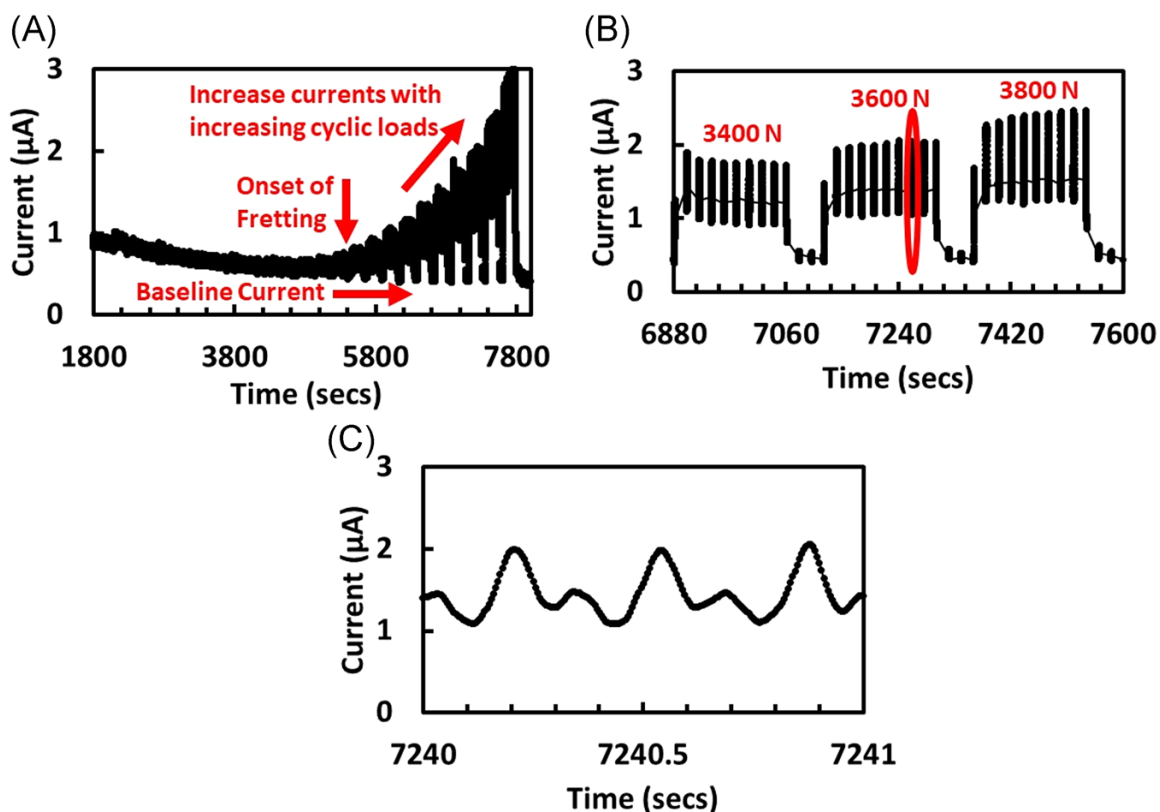


Fig. 6.3. (A) Typical example of currents (vs time) measured using the electrochemical setup for CoCrMo head. Note the baseline current, the time where the onset load is reached, and the rising currents with cyclic load beyond the onset. (B) Fretting currents recorded at three load levels (at about 2 hours, and above onset load) for CoCrMo head. Note the resting interval between cyclic loads where the currents fall, and the repeated intermittent acquisition of currents. (C) One second fretting currents at 3600 N (circled in B) is shown consisting of three higher and three smaller current peaks directly associated with the cyclic loading

The onset load was defined as the applied cyclic load where fretting was first observed in the ICFC protocol. It was defined as the load at which an abrupt change in the slope of root mean square about the mean (RMS) current vs cyclic load took place as shown in Figure 6.4 (for a representative Si_3N_4 and CoCrMo head test, Figures 6.4A and 6.4B, respectively). The RMS currents correlated closely with the average currents and remained stable and constant before fretting started. At the onset of fretting, the RMS

currents kept increasing (as did the average currents) with cyclic load. For example, for the CoCrMo head test shown in Figure 6.4B, this change in RMS current happened at approximately 1800 N and for the Si₃N₄ sample, the onset load was approximately 2200 N. The mean onset load for all Si₃N₄ heads was 2220 N (SD = 188 N) and for CoCrMo heads were 1740N (SD = 360 N; $p < .05$). The higher onset load indicated greater resistance to oxide disruption for the Si₃N₄/Ti-6Al- 4V test group. Also, once the fretting started for both groups, the rate of increase in fretting current for Si₃N₄ test group was lower (compared to CoCrMo) as evident by the smaller slope of the RMS current vs force data in Figure 6.4.

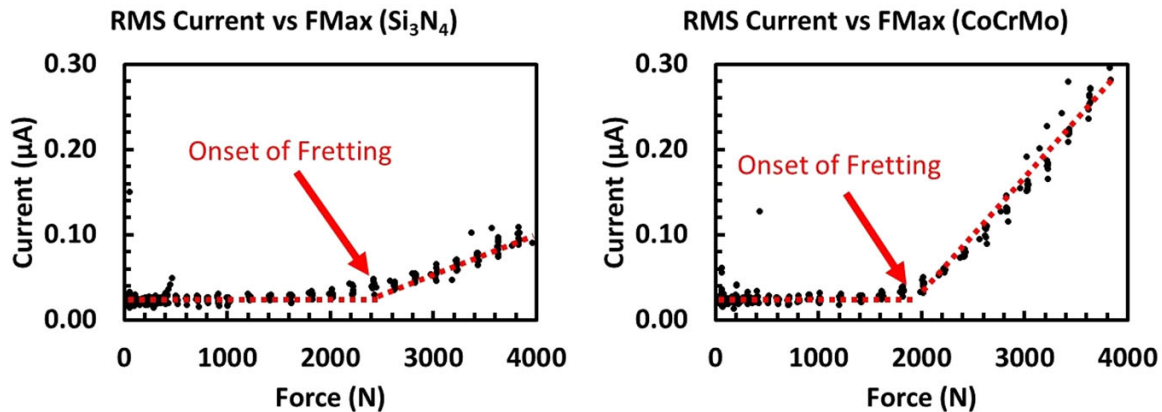


Fig. 6.4. RMS current vs max cyclic load for Si₃N₄ head and CoCrMo head. The sudden change in baseline slope was used to calculate the load at the onset of fretting. RMS, root mean square.

To compare the short-term fretting corrosion performance between Si₃N₄ and CoCrMo in the ICFC test, average fretting currents were calculated at three load levels (above the onset load). Figure 6.5 shows the box plot with fretting currents for the Si₃N₄ and CoCrMo heads ($n = 10$) at 3200, 3600, and 4000 N. Even though the data is

presented for only three applied loads, the CoCrMo heads showed higher average fretting current than the Si₃N₄ heads ($p < .05$) at all applied loads above the onset. For example, at 3200 N, the average fretting current for the CoCrMo heads was 0.685 μ A (SD = 0.631 μ A) whereas it was 0.189 μ A (SD = 0.114 μ A) for the Si₃N₄ heads. Higher cyclic loads led to higher fretting current in each group indicating greater oxide disruption with increasing loads for both groups. However, statistically lower average fretting currents for Si₃N₄ heads/Ti-6Al-4V interfaces indicated better fretting corrosion resistance (vs CoCrMo heads).

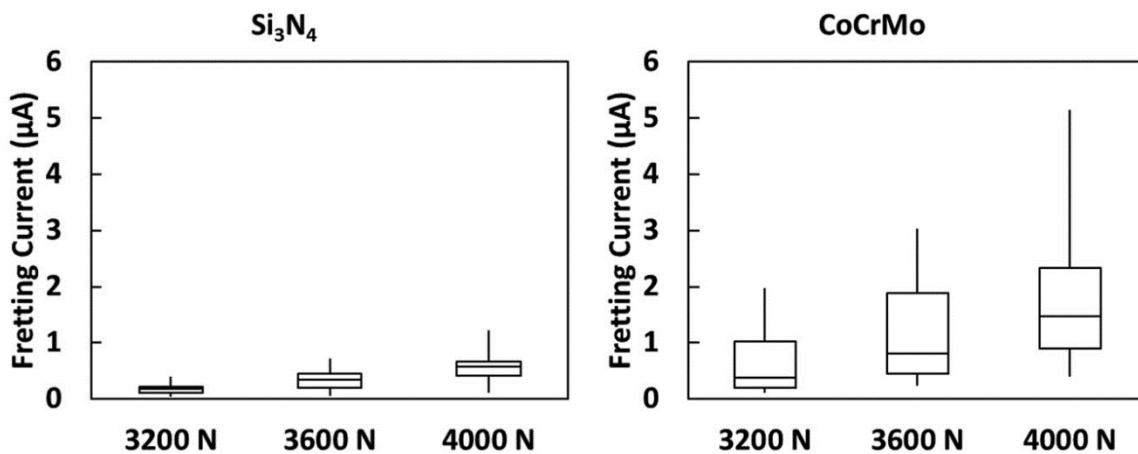


Fig. 6.5. Box plots showing fretting currents at three load levels for Si₃N₄ and CoCrMo heads. Si₃N₄ heads had statistically lower average fretting current ($p < .05$, $n = 10$ for each group) at each load level when compared to CoCrMo heads.

Figure 6.6A shows the fretting currents measured for a Si₃N₄ and a CoCrMo head at 3200 N (15 Hz) for one million cycles. The initial current peak (time, $t = 0$) measured (without cyclic motion) corresponded to the net resting corrosion currents prior to the start of cyclic loading PBS (at -50 mV vs Ag/AgCl). The cyclic motion was started at the

end of 30 minutes (to establish a stable baseline current). For both groups, the fretting currents decreased with time. At the end of one million cycles, the load was ramped down to a static value of 50 N which led to a sudden decrease in measured current as shown in Figure 6.6A. Figure 6.6B and 6.6C show the box plot with fretting currents measured throughout the test and during the last hour of the one-million cycle test. The average current for the Si_3N_4 heads was $0.048 \mu\text{A}$ (SD = $0.025 \mu\text{A}$) vs $0.369 \mu\text{A}$ (SD = $0.143 \mu\text{A}$) for the CoCrMo heads. The last hour and overall currents measured for Si_3N_4 heads were statistically lower than those for CoCrMo heads ($p < .05$).

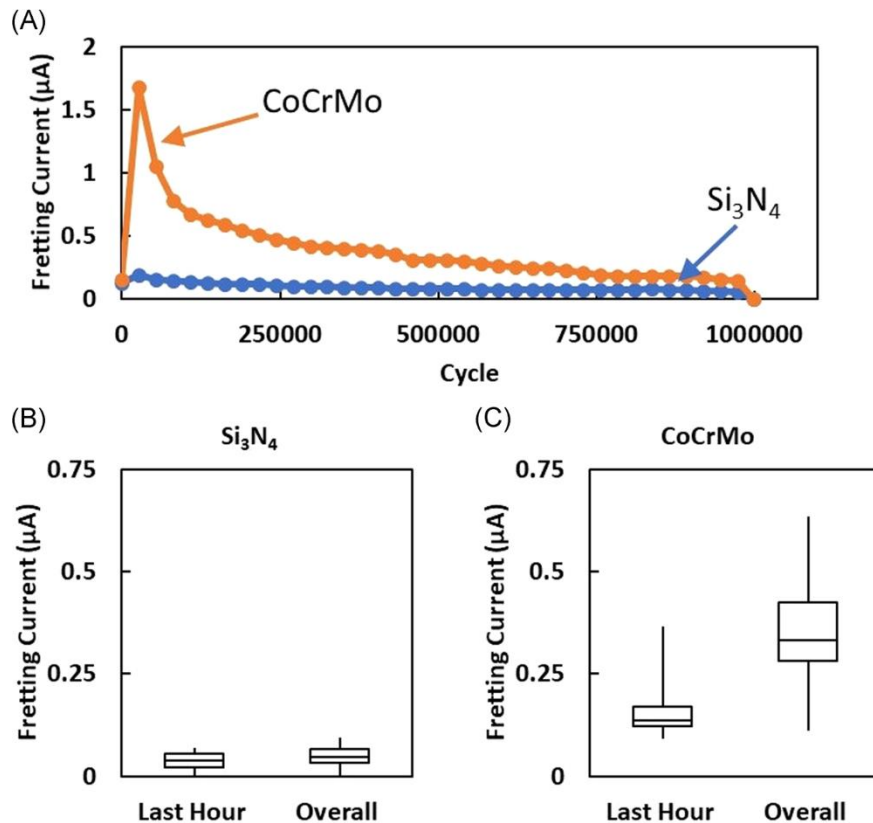


Fig. 6.6. (A) Fretting currents vs time at 3200 N (15 Hz) for both Si_3N_4 and CoCrMo heads during 1 million cycle fretting tests. Box plots showing fretting currents measured for (B) Si_3N_4 and (C) CoCrMo heads ($n = 10$ for each group). The Si_3N_4 heads had significant lower currents than the CoCrMo heads ($p < .05$).

Figure 6.7 shows the pull-off forces for the Si₃N₄ and CoCrMo heads (n = 10). The average pull-off force for the Si₃N₄ heads was 2600 N (SD = 230 N) vs 1450 N (SD = 180 N) for the CoCrMo heads ($p < .05$). A statistical difference in average pull-off forces (especially when the seating load was equal) indicated a difference in contact mechanics between the two interfaces. Figure 6.8 shows SEM image and EDS spectra of a Ti-6Al-4V trunnion that interfaced with a CoCrMo head. The presence of Co and Cr peaks in the corroded area on the trunnion implied that material was transferred from CoCrMo head onto the trunnion. Figure 6.9 shows SEM image and EDS spectra of a Ti-6Al-4V trunnion that interfaced with a Si₃N₄ head. The SEM image shows minimal damage and presence of salt buildup was confirmed by EDS spectra of the highlighted region. Also, only a fraction of the total area was in contact and experienced oxide disruption and no evidence of material transfer from the Si₃N₄ head to the Ti-6Al-4V trunnion was observed.

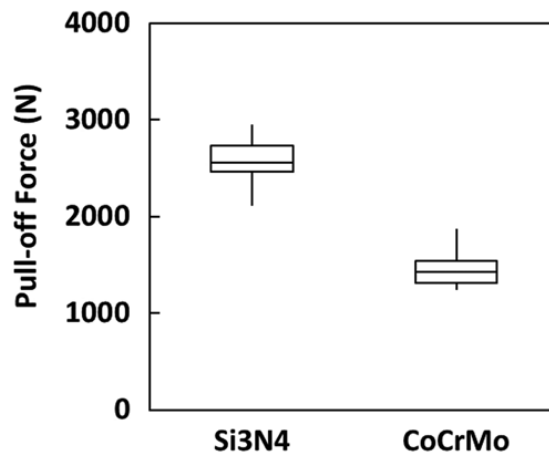


Fig. 6.7. Box plot of pull-off forces measured during head-neck disengagement for Si₃N₄ and CoCrMo samples (n = 10 for each group). Si₃N₄ heads had statistically higher average pull-off forces vs CoCrMo ($p < .05$).

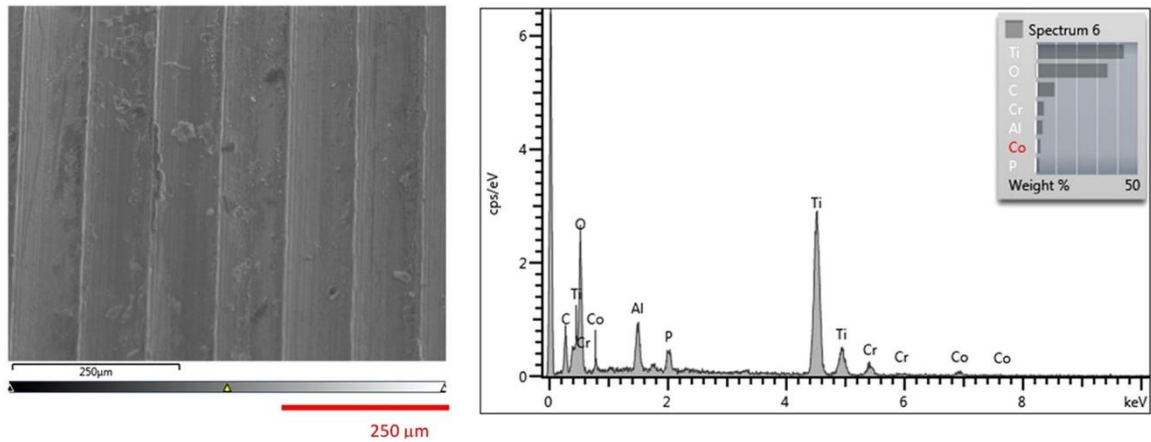


Fig. 6.8. Scanning electron microscopy image and EDS spectra of a Ti-6Al-4V trunnion that interfaced with a CoCrMo femoral head. EDS, Energy-dispersive X-ray spectroscopy.

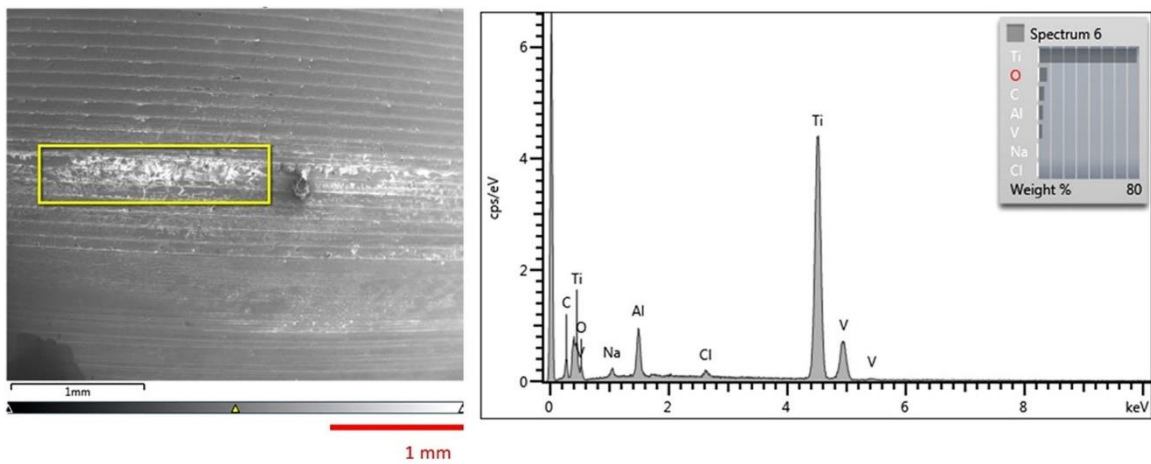


Fig. 6.9. Scanning electron microscopy image and EDS spectra of a Ti-6Al-4V trunnion that interfaced with a Si₃N₄ femoral head. EDS, Energy-dispersive X-ray spectroscopy.

Figure 6.10 shows the SEM images of a CoCrMo head (Figure 6.10A) and Si₃N₄ head (Figure 6.10B) that interfaced with Ti-6Al-4V trunnion. Figure 6.10B represented the most severe damage that was observed for a Si₃N₄ head. The rest of Si₃N₄ heads had

light surface damage at the contact region. The SEM image (Figure 6.10B) showed clear evidence that ridges from the trunnion were imprinted on the femoral heads and indicated material transfer from the trunnions to the heads. EDS spectra obtained from this area showed corrosion product buildup and revealed the presence of titanium oxide.

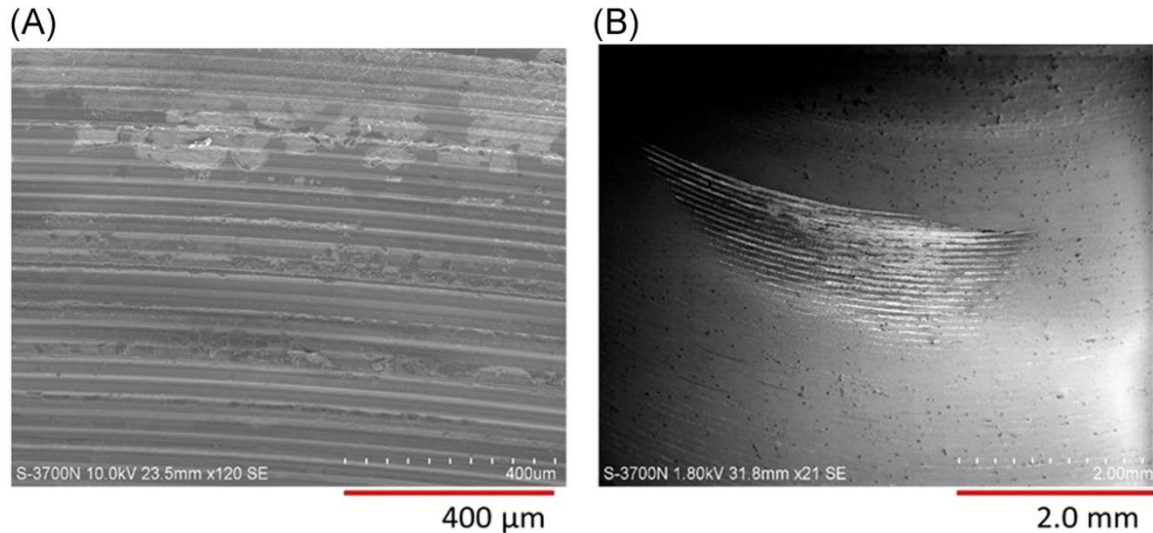


Fig. 6.10. (A) CoCrMo head (inferior). (B) Si₃N₄ head (inferior) that interfaced with Ti-6Al-4V trunnion.

6.4 Discussion

Fretting crevice corrosion has been recognized as a significant risk for modular devices with metal-on-metal surfaces. This study has shown that Si₃N₄ femoral heads reduce fretting corrosion compared with standard metal-on-metal head-neck interfaces. Disruption of passive oxide films (a feature of fretting corrosion) on metallic surfaces can be studied using the electrochemical setup and mechanical testing described in this work. By using a potentiostatic method with a CE, the anodic currents can be collected and used to assess the conditions where fretting corrosion occurs and the magnitude of the

corrosion response to cyclic loading. The anodic currents, in general, consist of both anodic dissolution current and the oxide film repassivation current. Previous work has shown the anodic dissolution current to be minimal when compared to the oxide film repassivation current, for both CoCrMo and Ti alloy oxide film disruption in the potential range investigated [207-208]. In this study, the background currents, which represent the overall electrochemical behavior of the undisrupted surface, were subtracted from the currents measured to obtain the true repassivation currents associated with fretting. The fretting currents provide information about the extent of passive film abrasion and subsequent release of corrosion debris from the interface. Higher fretting currents imply more corrosion debris generated (vs lower currents). When fretting starts, the currents increase and become cyclic in phase with the cyclic loads applied.

In this study, the fretting corrosion performance of Si_3N_4 femoral heads interfacing with Ti-6Al-4V trunnions was investigated and compared to a standard CoCrMo/Ti-6Al-4V combination. Lower fretting currents observed for Si_3N_4 femoral heads at all applied loads support the hypothesis that Si_3N_4 performs better (vs CoCrMo) in terms of fretting corrosion. Rowan et al., reported similar findings when they compared fretting currents for ceramic femoral heads on Ti-alloy trunnions (vs CoCrMo heads on Ti trunnions) [209]. Kyomoto et al., reported markedly less fretting initiated corrosion in ZTA ceramic heads (vs CoCrMo) in a hip simulator study [210].

The long-term fretting corrosion testing led to similar results with considerably lower currents observed for Si_3N_4 femoral head combination. The decrease in measured

currents over the 18 hours testing period for both test and control groups can be attributed to several factors. Plastic deformation is recognized as the primary damage mode for the head-neck taper and the work hardening associated with it will increase the hardness of the surface, decreasing further oxide abrasion at the same load (3200 N in the long-term test). The generation of debris during initial fretting (leading to higher fretting currents) can change the contact mechanics and possibly the fretting damage modes (ie, gross slip to stick). The changes in surrounding electrolyte (due to debris generation) can also change the tribochemical layer which will affect subsequent fretting currents. The decreased fretting currents have a direct implication for corrosion debris generated. In a retrieval study, Kocagoz et al., reported an order of magnitude difference in amount of metal released for head-neck combination involving ceramic heads (vs CoCrMo heads) [211]. The reduced fretting currents observed in the current study imply that a similar reduction in metal released is expected in the case of Si_3N_4 femoral heads. Also, besides the reduction in fretting corrosion response, the removal of Co and Cr debris from the joint space can potentially reduce or eliminate the adverse local tissue reaction (ALTR).

Approximately 25% increase in the average onset load for $\text{Si}_3\text{N}_4/\text{Ti}-6\text{Al}-4\text{V}$ combination (vs CoCr head/ $\text{Ti}-6\text{Al}-4\text{V}$) indicates a higher resistance to oxide disruption. As the combination of Si_3N_4 head/ $\text{Ti}-6\text{Al}-4\text{V}$ trunnion has less metallic area exposed to the electrolyte, it was expected to have less oxide abrasion and hence lower repassivation current as shown. However, higher onset loads for fretting in the case of Si_3N_4 heads indicate that the lower fretting currents are also due to changes in surface mechanics and

interlocking mechanism of head-neck taper between a ceramic and a metallic component. Rowan et al., reported onset loads of 1400 N for CoCr-V40(Ti alloy) couples and 2200 N for ceramic-V40 couples [209]. Bergmann et al., measured contact forces with instrumented hip implants in ten subjects during physically demanding and other less strenuous daily activities [212]. As expected, they reported that maximum forces increased with the level of activity. For example, the maximum force measured during walking for a 75 kg adult patient was a little less than 2000N (3000 N for a 100 kg adult patient) and forces measured during taking stairs down were 2250 N for a 75 kg adult (3750 N for a 100 kg adult patient). This implies that depending on the material combination used for head-neck taper, daily activities can lead to “onset” of fretting corrosion and strenuous activities can exacerbate the situation further.

Approximately 50% increase in pull-off forces observed for Si₃N₄ heads (2600 N) also suggests greater interlocking forces compared to CoCrMo heads (1450 N). Larger interlocking forces would lead to better resistance to micromotion, less oxide abrasion, and reduced fretting corrosion at head-neck taper junction. Previous research showed that larger seating loads result in higher pull-off forces for the same material combination [204,213]. However, our study investigated different material combination with the same seating loads. This could be due to the different interlocking mechanism between two types of interfaces. Using idealized statics, Gilbert et al., showed that the pull-off forces are directly proportional to the coefficient of friction (COF) [214]. Recent work measured the COF between Si₃N₄/Ti-6Al-4V couples and found it to be higher than COF for

CoCrMo/Ti-6Al-4V [215]. Higher coefficients of friction will increase the shear forces at the interface and lead to higher interlocking forces. This will, in turn, reduce the micromotion within head-neck taper junction. As fretting current is directly related to micromotion, greater interlocking forces will also result in lower fretting currents.

The microscopic and EDS analysis of the trunnions revealed the presence of Ti oxide debris which came from surface disruption by the Si_3N_4 and CoCrMo heads. During seating of the femoral head on the stem, plastic deformation leads to an interference fit between the two parts. The initial plastic deformation of Ti-6Al-4V is expected to be small due to its high-yield stress/hardness and the total area in actual contact will also be a small fraction of the total available area. Fretting motion of these interfaces generated oxide debris at the contact points and this oxide debris was transferred from the Ti-6Al-4V trunnion to the Si_3N_4 head. The EDS analysis of trunnions interfacing with CoCr heads also revealed presence of Co and Cr based particles, likely oxides of the alloy, transferred to the trunnions as well as Ti-oxide debris transferred to the CoCr head. This confirms that the fretting currents captured were originating from repassivation of the oxides on both head and neck components. EDS spectra of the trunnions interfacing with Si_3N_4 heads showed oxide debris but no evidence of silicon transfer from the Si_3N_4 femoral head.

The SEM and EDS analysis of Si_3N_4 and CoCrMo femoral heads showed evidence of imprinting of the machined grooves from the Ti-6Al-4V trunnion on the Si_3N_4 head trunnion. Langton et al., observed imprinting of machined grooves in their study and

speculated that this plastic deformation can alter contact stresses and increase the potential for wear [216]. Panagiotidou et al., attributed the enhanced wear and corrosion at the modular taper junction to the surface morphology [217]. They observed a change in the smooth surface of the head taper when it articulated against a “rough” neck taper. Pourzal et al., found a correlation between the stem surface topography and Goldberg damage scores¹¹ for retrieved implants [218]. Moharrami et al., suggested that the increased hardness of titanium oxide might be responsible for abrasive wear of the harder more wear resistant CoCrMo [219]. Imprinting has also been observed on CoCrMo heads interfacing with CoCrMo stems suggesting that it has both electrochemical and mechanical origins related to the nature of local contact [211]. Arnholt et al., investigated the effect of stem taper microgrooves on corrosion at the head-neck junction and concluded that stem taper morphology had no correlation with the fretting corrosion damage or metal release [212]. Overall, although imprinting is a well-documented phenomenon, the published literature is contradictory, and the influence of microgrooves (leading to imprinting) is still not well understood.

Limitations of the present work relate to the nature of *in-vitro* tests. First, each femoral head was manually placed on its respective trunnion, which may have led to uneven placement before the head was seated. This limitation was minimized by applying large seating loads (4000 N) at the initial stage. Second, both ICFC and one-million cycle fretting corrosion test were performed using a uniaxial cyclic force which does not simulate the more complex *in vivo* loading cycles. While it might have simplified the

simulated conditions, it provided for an ability to be more systematic in the comparative assessments. Third, the seating process was performed quasistatically and under highly controlled conditions. This was not the typical impaction performed by surgeons.

However, studies have shown that increasing the seating load has a limited effect on taper stability, thus the seating load (4000 N) used in this study is a reasonable representation of impact magnitude applied by surgeons. Also, inductively coupled plasma mass spectroscopy was not utilized to analyze the metal ion levels in the solution after testing. Despite these limitations, the superior fretting corrosion behavior of $\text{Si}_3\text{N}_4/\text{Ti-6Al-4V}$ over traditional metallic combination ($\text{CoCrMo}/\text{Ti-6Al-4V}$) adds to the growing literature that points to Si_3N_4 femoral heads as a viable option for THA.

6.5 Conclusions

We hypothesized that Si_3N_4 femoral heads will perform better (vs CoCrMo) in terms of fretting corrosion at the head-neck taper interface in a modular hip prosthesis with Ti-6Al-4V trunnion. Fretting currents measured at different loads showed a marked decrease for Si_3N_4 heads vs CoCrMo heads which supports this hypothesis. Both groups exhibited a biphasic current response related to the cyclic loading, but higher average currents observed for CoCrMo heads indicated greater oxide disruption and corrosion as compared to the Si_3N_4 heads. The increase in onset load for the Si_3N_4 heads vs the CoCrMo heads for same seating force indicates a substantial difference in the contact mechanics of taper locking for both materials mounted on Ti-6Al-4V reunions. The

long-term (one million cycle tests) fretting currents also showed a significant reduction for Si_3N_4 heads when compared to CoCrMo heads. SEM/EDS analyses revealed material transfer from the CoCrMo heads onto the Ti-6Al-4V trunnions, but no material transfer from the Si_3N_4 heads was observed onto the Ti-6Al-4V trunnions. Decreased fretting currents (vs CoCrMo heads), and elimination of Co/Cr debris from the periprosthetic joint may reduce ALTRs associated with metal-on-metal interfaces making Si_3N_4 an attractive candidate for femoral head material for THA.

7. Synthesis of the Work

7.1 General Discussion

Modular taper fretting crevice corrosion *in vivo* has multiple interacting processes that lead to a highly complex system that includes surface mechanics and tribology, the physics and electrochemistry of passive oxide film covered alloys, redox reactions that alter potential and generate currents, and metal deformation, and can result in specific and unique degradation products. While mechanically assisted crevice corrosion has been adopted as a term to describe modular taper corrosion, the overwhelming focus of the research community has been on the mechanical aspects of the corrosion/degradation that occurs with very little focus on the crevice and its role in the process, or the nature of the solution changes and potential changes required to induce ongoing crevice corrosion reactions. The purposes of this studies are to undertake both theoretical and experimental results of fretting crevice corrosion to fill up some gaps in the existing corrosion science, which involves complex multi-physics problems associated with THA. By filling these gaps, which are mentioned in chapter one, fundamentals of fretting crevice corrosion, e.g., electrochemical reaction and materials combination, and its related phenomena could be further developed and understood.

So far, the mechanism of fretting initiated crevice corrosion, where fretting is only needed to initiate ongoing crevice corrosion processes, has only been demonstrated for 316L stainless steel alloys in physiological saline at specified potentials [90]. The other alloys, which have been clearly documented to experience crevice corrosion like degradation processes *in vivo* (e.g., etching, intergranular corrosion, etc.) have not been

documented to exhibit a similar fretting initiated process *in vitro* to date. However, 316L SS has shown that fretting can initiate a self-propagating crevice corrosion reaction, generating a local crevice solution chemistry that can sustain and promote attack within the crevice region even with subsequent cessation of fretting. This points to the need to explore alternatives in Ti alloy and CoCr alloy crevice geometries where propagating crevice corrosion reactions can be induced.

A new 2D pin-on-disk system was described in this study, which can provide in-depth understanding of how debris is generated during fretting crevice corrosion and reveal that stainless steel is sensitive to crevice corrosion under fretting initiated conditions. This system can be utilized to analyze solution chemistry after fretting crevice corrosion due to its small amount of solution volume. This feature could assist to address some potential questions regarding post-test ion concentration due to fretting crevice corrosion or other type of MACC. The theoretical model using tribological and electrochemical concepts explains the fundamental mechanism of tribocorrosion [19]. This model, which is the first time, put surface electrochemical impedance and capacitance into account to explain oxide disruption and repassivation during fretting corrosion. This model can be adapted to other types of MACC for better understanding their fundamental mechanism and to be used in numerical modeling techniques to determine fretting corrosion currents based on tribological interactions. The device testing experiments of Si₃N₄ femoral head against Ti-6Al-4V trunnion prove that this ceramic material has better fretting corrosion resistance than the traditional metallic combination and could lead to longer lifetimes for implant devices [58]. The results

expand surgeons' options for choosing appropriate implant materials when preparing for THA.

7.2 Detail of Accomplishments

The goal of chapter 3 was to utilize a custom-made pin-on-disk fretting corrosion setup to investigate debris generation processes, including their chemistry and physical distribution on the contact surface [27]. Another outcome of this chapter is that this setup provides for the visualization of different phases of debris generation. It provides strong evidence to support the clinical observations that debris can escape from fretting contacts and wind up in in the periprosthetic tissue near implants. These results also show how high cobalt ions in the solution can arise simply from the fretting corrosion interactions where the solid debris contains little Co and is mostly comprised of Cr-phosphate-based particles. The significant difference ($p < 0.05$) detected between Cr and Co ionic concentrations in the solution demonstrates that high Co concentration in patient's blood, who have metallic implant device inside their body, can be explained by this simplified laboratory circumstance [222] where the chromium interacts with phosphate and oxygen to form Cr oxides and phosphates, while the Co ions remain soluble in the solution. Thus, this method successfully simulates fretting crevice corrosion debris generation inside the human body by creating a stable electrochemical environment, where critical parameters can be controlled and adjusted for *in-vitro* study purposes. This setup could be utilized to study cellular response to fretting corrosion solid degradation products *in-vitro*. Similar studies have been reported to study the relationship between corrosion debris and cellular

viability [223-224]. However, this setup has two unique features, small solution volume and transparent reaction chamber, that would make it as an ideal system for further exploring any potential effect between different type of cells and various metallic materials during or after fretting corrosion.

Compared with other *in vitro* tribocorrosion testing systems, this custom POD setup has its unique features, such as a visualization capability and small amount of electrolyte volume. Visualization has been combined with corrosion systems in many studies [225-226]. However, none of them focus on debris generation during tribocorrosion. The setup in chapter 3 provides direct evidence of this behavior along with fretting crevice corrosion while capturing electrochemical and mechanical signals. Therefore, this capability may allow one to study the long-term fretting crevice corrosion relationships between debris generation and fretting current, where, for example, increasing amount of debris generated might reduce fretting currents by reducing contact area with the metal surface and alter the coefficient of friction. Another feature, the small volume of solution, helps to better understand ion release processes during corrosion. Most setups studying tribocorrosion, including most POD setup, have larger volumes of testing solution, usually hundreds of milliliters, which can make ion release analysis difficult due to the large dilution effect [227]. In chapter 3, about 1.5 ml solution was used to maintain the required electrochemical environment. The small amount of volume into which metal ions are released thus increase the ion concentration level that could be detected.

Since tribocorrosion is a type of corrosion that takes both electrochemical and mechanical factors into account, a theory or model could become important to reveal the fundamental mechanism of this phenomena. Many theories have been built or developed to assist people for better understanding tribocorrosion from different perspectives [228-229]. However, most theories prefer to define tribocorrosion as the superposition of tribology and corrosion independently with, perhaps, an interaction term. The goal of chapter 4 is to establish a tribocorrosion model, using fretting corrosion as demonstration, based on a series of parameters including load, displacement hardness and impedance etc. This model successfully describes the corrosion response in terms of current and potential versus time with knowledge of the sliding displacement-time behavior and other materials characteristics. The results of this mode show that electrochemical responses (current and potential) and mechanical actions (abrasion deformation and oxide disruption) are combined and synergistic and that the currents generated are not only from ion release, but from oxide film repassivation and thus directly results from oxide disruption processes. Thus, a linear sum of corrosion (current-based measurements) and wear (a volume loss-based measurements) is not an accurate approach for tribocorrosion testing. Different conditions, e.g., waveform and electrolyte, were also examined to exhibit that this model could be applied in varied circumstances and is a general guidance for helping to understand the fundamental mechanism of tribocorrosion. One thing that needs to be noticed is that the setup developed in chapter 3 is used to provide experimental evidence to support the model, which can be treated as a validation test of this custom POD testing system.

Any tribocorrosion that happens within human body is not at a stable environment, or a fixed potential. Most of *in vitro* studies prefer using fixed potential as the electrochemical condition so that oxide film thickness can be well-controlled or estimated due to oxide repassivation theory [230] and the currents generated can be measured and quantified. However, potential varies *in vivo* and could become more negative inside the body because tribocorrosion could lead to numerous electrons getting capacitively tapped at the material surface, which induces a negative charge accumulation and negative potential excursion. The model in chapter 4 is demonstrated not only under fixed potential conditions (scratch test) but also validated in the case where the potential is allowed to fluctuate with conditions, as occurs in the real-world situation. The tests were repeated under different frequencies, where any fretting current was well-predicted based on the corresponding potential change and the rest of parameters.

Even though this model was demonstrated by studying fretting corrosion on CoCrMo alloys, it can be also used to evaluate tribocorrosion behavior of Ti-6Al-4V and stainless steel alloy. As for stainless steel alloy, Chapter 5 reported on a novel phenomenon termed fretting initiated crevice corrosion (FICC) which has been widely used as implant material over decades. The study found that crevice corrosion of 316 LVM stainless steel can be triggered readily by just a few repeated fretting strokes in a POD test system under the appropriate potential conditions. The initiation of crevice corrosion is highly sensitive to electrode potential and can occur hundreds of millivolts below the breakdown potential for stainless steel. As one of the consequences of FICC, island-like corrosion was observed where the crevice attack started at the pin-disk-crevice

contact region within the crevice. The sensitivity to this process increases as the potential is shifted anodically, which can be considered as evidence of FICC. As an electrochemical reaction, crevice corrosion is sensitive to potential. Three domains use specific potentials as the boundary to separate each from the other. Within the unstable domain (anodic potentials), only a few numbers of cycles fretting motion are required to cause crevice corrosion to occur at the pin and disk junction. Here, the corrosion products released into the solution created an altered electrolyte that increased the susceptibility of the surface to break down its oxide and corrode. As long as the crevice geometry was maintained, the crevice corrosion reaction would continue and would expand from the pin-disk junction outward towards the edge of the pin crevice. Once the two surfaces disengaged the crevice corrosion reaction ceases immediately and the surfaces repassivated. This points to the important interplay between fretting corrosion generated solution chemistry changes that subsequently increase the susceptibility of oxide film breakdown and the onset of crevice corrosion.

Even though many implant devices, especially orthopedic devices, are replacing their bulk materials from stainless steel to more corrosion resistance alloy, e.g., Ti and CoCrMo alloy, stainless steel is still on the market in a wide range of devices where fretting crevice corrosion is possible, e.g., spinal implant, due to its low-cost feature. Physical fixation and modular structure of these implant devices will result in contact interfaces or junctions with potential risk of tribocorrosion and fretting initiated crevice corrosion due to daily activities. FICC could become a significant concern in such circumstances and shorten the lifetime of these implanted devices. Corrosion products,

generated by FICC, can release into surrounding biological environment, and increase the possibility of adverse local tissue reaction (ALTR). The results of chapter 5 provide a potential solution for reducing or eliminating FICC, which is to maintain the environmental potential within metastable or stable regions. However, the way to achieve this goal is still a challenge because of highly dynamic and uncertain nature of the body environment.

The studies from chapter 3 to chapter 5 are mainly focused on the fundamental aspects of fretting crevice corrosion. These materials must be applied as implanted devices using manufacturing processes that maximize their corrosion resistance. Chapter 6 introduced a device testing method by assessing fretting corrosion behavior between novel $\text{Si}_3\text{N}_4/\text{Ti-6Al-4V}$ head-neck taper couples and traditional $\text{CoCrMo}/\text{Ti-6Al-4V}$ couples. Even though we did not measure the initial pull-off load, which could provide comparison with the last pull-off tests, right after heads were seated, the fretting current results from both incremental cyclic fretting corrosion (ICFC) and long-term testing still show that ceramic-on-metal combinations exhibit better fretting corrosion resistance than metal-on-metal couples. As a ceramic material, Si_3N_4 , is non-conductive under this circumstance so that corrosion could only occur at the metallic phase instead of on both surfaces. Even though materials transfer were observed at head-neck taper junction in few ceramic-on-metal couples, which may raise concerns regarding wear and particle generation, Si_3N_4 demonstrate itself as a potentially suitable material that can be used in total hip arthroplasty (THA) field.

When consider fretting crevice corrosion in real applications, testing methods usually follow standard protocols, e.g., ASTM or ISO etc. In chapter 6, $\text{Si}_3\text{N}_4/\text{Ti-6Al-4V}$ exhibit significantly less fretting corrosion damage under specific ASTM tests. This study, along with many studies of Zirconia Toughed Alumina (ZTA), points out that ceramic materials may play an important role in future orthopedic implant device development [231]. However, metallic materials as implant devices have their unique advantages, such as high strength and relatively low cost for manufacture and favorability for surface coating or modification. A combination of metallic and ceramic materials as modular implant devices could become a possible solution for reducing fretting corrosion on total hip arthroplasty, or orthopedic implant devices in general.

8. Conclusions

This dissertation has presented a series of studies related to different aspects of the fundamental mechanisms of fretting crevice corrosion, including theoretical, materials-based and application-specific experiments. The major findings could be concluded as followings.

Chapter 3 documented debris generation between CoCrMo alloy pin and disk samples, and the surface deformation resulting from fretting corrosion using a custom 2D pin-on-disk fretting corrosion setup. The results showed that debris was generated rapidly during fretting corrosion virtually. The solid debris generated was along with ions release. Chapter 4 describe a heredity integral model, including the physics and chemistry of passive oxide films, contact mechanics and electrochemical impedance, to determine the time course of currents and potentials associated with tribocorrosion processes. Fretting initiated crevice corrosion (FICC) was studied in chapter 5. This study has demonstrated FICC in 316LVM stainless steel is potential related and several cycles of fretting motion could trigger FICC in PBS. Finally, chapter 6 assessed fretting corrosion behavior between $\text{Si}_3\text{N}_4/\text{Ti-6Al-4V}$ and $\text{CoCrMo}/\text{Ti-6Al-4V}$ head-neck modular tapers. $\text{Si}_3\text{N}_4/\text{Ti-6Al-4V}$ shows better fretting corrosion resistance compare with traditional metallic combination.

The general goal of this dissertation was not to focus on implant design or improvement but to provide fundamental studies of fretting crevice corrosion in orthopedic implant devices using engineering methods. Current research involved in fretting crevice corrosion, or MACC, are often oversimplified or not fully explored,

which could be passed on to the patient eventually and cause unpredictable negative effects to the implant device field. This dissertation introduced several methods for studying fretting crevice corrosion and can be considered as ideas for future research. The ultimate goal of studying metallic orthopedic implant devices is to reduce number of revision surgeries caused by corrosion or other ALTR and achieve life-long improvements in performance.

9. Future Work

This work addressed some aspects of the fundamental mechanism of fretting crevice corrosion using *in-vitro* testing methods including pin-on-disk setup and ASTM standard protocol. While several important conclusions have been made, further research, is still indispensable, especially focusing on cellular culture study and physiologically environmental testing. PBS, as the simplest inorganic physiological solution, was chosen to provide stable electrochemical environment for *in vitro* corrosion studies. However, this simplified solution would be missing important information of how organic molecules and different type of cells react with contact interface, which could reflect the severity of corrosion damage. Solution rich in protein or other complex organic molecules could lead to higher viscosity, which protein adhesion occurs on exposed surface and the create bio-layer for lubrication purpose [232].

Previous works have been reported using fetal bovine serum (FBS) and Dulbecco's Modified Eagle Medium (DMEM) as electrolyte to study fretting corrosion or tribocorrosion on metallic materials. Their results show that solution chemistry have different effect on alloy surface compare with PBS only condition. Except different type of solution, inflammatory condition could also lead to implant corrosion, where inflammatory cell induced corrosion (ICIC) has been reported by Gilbert's lab [233]. Recent work has developed solutions that mimic this condition and tested in pin-on-disk setup [234]. The most ideal electrolyte is human joint fluid or patient synovial fluid as they represent the true solution environment surrounding implants. But there are some challenges for using it for testing. First, the volume of joint fluid is limited, which not

sufficient for most of tribocorrosion testing setup. Second reason is that availability due to surgical procedure. The last one would be the variability in biological sample, where composition need be well-clarified. The 2D custom fretting corrosion setup described in chapter 3 could reduce the difficulty since the electrochemical chamber can keep small volume of solution, e.g., 1.5 ml.

Cellular study, as an important preclinical and lab-based study, in corrosion or tribocorrosion field has not been fully explored or studied. Previous work from Gilbert's lab demonstrated that potential affect cell viability under fretting corrosion [235]. Studies also show that debris due to wear or fretting corrosion could lead to cell death, where debris particle are generated separately from cell culture media [236]. This study could only prove that debris could reduce cell growth or affect its viability but lack of evidence to reflect any change which could affect cellular behavior during fretting corrosion. One possible solution is that a novel electrochemical chamber with high transparency could be designed and combine with the 2D fretting corrosion setup so that cellular reaction along with debris generation could be observed under DOM.

Future study of FICC on stainless steel has been reported in chapter 5, where multiple studies need to be done to better understand FICC from different aspects. Other than that, studies focus on whether FICC occur at different materials combinations, like CoCrMo or Ti-6Al-4V, should also take into account as potential projects that need for exploration because implant device has modular design strategy, which each part made by different material. Besides materials study, *in-vitro* device testing, e.g., long-term cyclic loading test, and retrieval study is also qualified for further investigation. Both of

study are assessing FICC from more comprehensive aspect, which can reflect truly damage on implant device due to FICC.

As for the Si_3N_4 , comparison of tribocorrosion resistance between itself and Zirconia Toughened Alumina (ZTA), which is a ceramic material with zirconia grain in alumina matrix, in hip-neck taper junction testing is needed. ZTA as the most popular ceramic implant materials has been used in orthopedic implant device due to its excellent biocompatibility. Many studies show that both are serving as ideal ceramic materials for clinical purpose based on *in-vitro* material testing [237]. However, there are not enough works, including clinical study, to document their fretting corrosion behavior as femoral head seating on Ti-alloy trunnion for total hip arthroplasty (THA) simulation tests. The potential idea for this or similar test is that same protocol from chapter 6 will applied on a new couple, ZTA/Ti-6Al-4V, and the results will compare with existing data for further analysis.

10. References

1. Corbett KL, Losina E, Nti AA, Prokopetz JJ, Katz JN. Population-based rates of revision of primary total hip arthroplasty: a systematic review. *PLoS One*. 2010 Oct 20;5(10):e13520.
2. Pivec R, Johnson AJ, Mears SC, Mont MA. Hip arthroplasty. *The Lancet*. 2012 Nov 17;380(9855):1768-77.
3. Ulrich SD, Seyler TM, Bennett D, Delanois RE, Saleh KJ, Thongtrangan I, Kuskowski M, Cheng EY, Sharkey PF, Parvizi J, Stiehl JB. Total hip arthroplasties: what are the reasons for revision? *International orthopaedics*. 2008 Oct 1;32(5):597-604.
4. Kavanagh BF, Fitzgerald Jr RH. Multiple revisions for failed total hip arthroplasty not associated with infection. *The Journal of bone and joint surgery. American volume*. 1987 Oct 1;69(8):1144-9.
5. Wodecki P, Sabbah D, Kermarrec G, Semaan I. New type of hip arthroplasty failure related to modular femoral components: breakage at the neck-stem junction. *Orthopaedics & Traumatology: Surgery & Research*. 2013 Oct 1;99(6):741-4.
6. Ekelund A, RYDELL N, NILSSON OS. Total hip arthroplasty in patients 80 years of age and older. *Clinical Orthopaedics and Related Research®*. 1992 Aug 1;281:101-6.
7. Katti KS. Biomaterials in total joint replacement. *Colloids and surfaces B: Biointerfaces*. 2004 Dec 10;39(3):133-42.

8. Sumner DR. Long-term implant fixation and stress-shielding in total hip replacement. *Journal of biomechanics*. 2015 Mar 18;48(5):797-800.
9. Huiskes R, Weinans H, Van Rietbergen B. The relationship between stress shielding and bone resorption around total hip stems and the effects of flexible materials. *Clinical orthopaedics and related research*. 1992 Jan 1:124-34.
10. Montemor MF, Ferreira MG, Hakiki NE, Belo MD. Chemical composition and electronic structure of the oxide films formed on 316L stainless steel and nickel based alloys in high temperature aqueous environments. *Corrosion science*. 2000 Sep 1;42(9):1635-50.
11. Karuppall R. Biological fixation of total hip arthroplasty: facts and factors. *Journal of orthopaedics*. 2016 Sep;13(3):190.
12. Ulrich SD, Seyler TM, Bennett D, Delanois RE, Saleh KJ, Thongtrangan I, Kuskowski M, Cheng EY, Sharkey PF, Parvizi J, Stiehl JB. Total hip arthroplasties: what are the reasons for revision?. *International orthopaedics*. 2008 Oct 1;32(5):597-604.
13. Skendzel JG, Blaha JD, Urquhart AG. Total hip arthroplasty modular neck failure. *The Journal of arthroplasty*. 2011 Feb 1;26(2):338-e1.
14. Magnissalis EA, Zinelis S, Karachalios T, Hartofilakidis G. Failure analysis of two Ti - alloy total hip arthroplasty femoral stems fractured in vivo. *Journal of Biomedical Materials Research Part B: Applied Biomaterials: An Official Journal of The Society for Biomaterials, The Japanese Society for Biomaterials, and The*

- Australian Society for Biomaterials and the Korean Society for Biomaterials.
2003 Jul 15;66(1):299-305.
15. Dobzyniak M, Fehring TK, Odum S. Early failure in total hip arthroplasty.
Clinical Orthopaedics and Related Research®. 2006 Jun 1;447:76-8.
 16. Dangles CJ, Altstetter CJ. Failure of the modular neck in a total hip arthroplasty.
The Journal of arthroplasty. 2010 Oct 1;25(7):1169-e5.
 17. Ingham E, Fisher J. Biological reactions to wear debris in total joint replacement.
Proceedings of the Institution of Mechanical Engineers, Part H: Journal of
Engineering in Medicine. 2000 Jan 1;214(1):21-37.
 18. Sukur E, Akman YE, Ozturkmen Y, Kucukdurmaz F. Particle disease: a current
review of the biological mechanisms in periprosthetic osteolysis after hip
arthroplasty. The open orthopaedics journal. 2016;10:241.
 19. Gilbert JL, Zhu D. A metallic biomaterial tribocorrosion model linking fretting
mechanics, currents, and potentials: Model development and experimental
comparison. Journal of Biomedical Materials Research Part B: Applied
Biomaterials. 2020 Nov;108(8):3174-89.
 20. Langton DJ, Jameson SS, Joyce TJ, Hallab NJ, Natu S, Nargol AV. Early failure
of metal-on-metal bearings in hip resurfacing and large-diameter total hip
replacement: a consequence of excess wear. The Journal of bone and joint
surgery. British volume. 2010 Jan;92(1):38-46.
 21. Gkagkalis G, Mettraux P, Omoumi P, Mischler S, Rüdiger HA. Adverse tissue
reaction to corrosion at the neck-stem junction after modular primary total hip

- arthroplasty. *Orthopaedics & Traumatology: Surgery & Research*. 2015 Feb 1;101(1):123-6.
22. Gilbert JL, Jacobs JJ. The mechanical and electrochemical processes associated with taper fretting crevice corrosion: a review. In *Modularity of orthopedic implants* 1997 Jan. ASTM International.
23. Smith, Stephanie Marie, "Compliance, Hardness, and Fretting Corrosion in Modular Taper Joints: The Micromechanics of Contact" (2020). All Dissertations. 2604. https://tigerprints.clemson.edu/all_dissertations/2604
24. Levine DL, Staehle RW. Crevice corrosion in orthopedic implant metals. *Journal of biomedical materials research*. 1977 Jul;11(4):553-61.
25. Willert HG, Brobäck LG, Buchhorn GH, Jensen PH, Köster G, Lang I, Ochsner P, Schenk R. Crevice corrosion of cemented titanium alloy stems in total hip replacements. *Clinical Orthopaedics and Related Research (1976-2007)*. 1996 Dec 1;333:51-75.
26. Sutow EJ, Jones DW, Milne EL. Materials Science: In vitro Crevice Corrosion Behavior of Implant Materials. *Journal of dental research*. 1985 May;64(5):842-7.
27. Zhu D, Liu Y, Gilbert JL. In vitro fretting crevice corrosion damage of CoCrMo alloys in phosphate buffered saline: Debris generation, chemistry and distribution. *Acta Biomaterialia*. 2020 Sep 15;114:449-59.
28. Hussey DK, McGrory BJ. Ten-year cross-sectional study of mechanically assisted crevice corrosion in 1352 consecutive patients with metal-on-polyethylene total hip arthroplasty. *The Journal of Arthroplasty*. 2017 Aug 1;32(8):2546-51.

29. Jacobs JJ, Urban RM, Gilbert JL, Skipor AK, Black J, Jasty M, Galante JO. Local and distant products from modularity. *Clinical Orthopaedics and Related Research*. 1995 Oct 1;319:94-105.
30. McGrory BJ, McKenney BR. Revision for taper corrosion at the head-neck junction: pearls and pitfalls. *Current reviews in musculoskeletal medicine*. 2016 Mar 1;9(1):97-102.
31. Gill HS, Grammatopoulos G, Adshead S, Tsialogiannis E, Tsiridis E. Molecular and immune toxicity of CoCr nanoparticles in MoM hip arthroplasty. *Trends in molecular medicine*. 2012 Mar 1;18(3):145-55.
32. Gilbert JL, Buckley CA, Jacobs JJ. In vivo corrosion of modular hip prosthesis components in mixed and similar metal combinations. The effect of crevice, stress, motion, and alloy coupling. *Journal of biomedical materials research*. 1993 Dec;27(12):1533-44.
33. Goldberg JR, Gilbert JL, Jacobs JJ, Bauer TW, Paprosky W, Leurgans S. A multicenter retrieval study of the taper interfaces of modular hip prostheses. *Clinical Orthopaedics and Related Research*. 2002 Aug 1;401:149-61.
34. Swaminathan V, Gilbert JL. Potential and frequency effects on fretting corrosion of Ti6Al4V and CoCrMo surfaces. *Journal of Biomedical Materials Research Part A*. 2013 Sep;101(9):2602-12.
35. Liu Y, Gilbert JL. The effect of simulated inflammatory conditions and pH on fretting corrosion of CoCrMo alloy surfaces. *Wear*. 2017 Nov 15;390:302-11.

36. Goldberg JR, Gilbert JL. Electrochemical response of CoCrMo to high-speed fracture of its metal oxide using an electrochemical scratch test method. *Journal of Biomedical Materials Research: An Official Journal of The Society for Biomaterials and The Japanese Society for Biomaterials*. 1997 Dec 5;37(3):421-31.
37. Stern M. A method for determining corrosion rates from linear polarization data. *Corrosion*. 1958 Sep;14(9):60-4.
38. Cabrini M, Lorenzi S, Pastore T. Cyclic voltammetry evaluation of inhibitors for localised corrosion in alkaline solutions. *Electrochimica acta*. 2014 Apr 1;124:156-64.
39. Jüttner K. Electrochemical impedance spectroscopy (EIS) of corrosion processes on inhomogeneous surfaces. *Electrochimica Acta*. 1990 Oct 1;35(10):1501-8.
40. Wu PQ, Celis JP. Electrochemical noise measurements on stainless steel during corrosion-wear in sliding contacts. *Wear*. 2004 Mar 1;256(5):480-90.
41. Smith SM, Gilbert JL. Compliant interfaces and fretting corrosion of modular taper junctions in total hip implants: The micromechanics of contact. *Tribology International*. 2020 May 24:106437.
42. ASTM F1875-98(2014), Standard Practice for Fretting Corrosion Testing of Modular Implant Interfaces: Hip Femoral Head-Bore and Cone Taper Interface, ASTM International, West Conshohocken, PA, 2014, www.astm.org

43. Matusiewicz H. Potential release of in vivo trace metals from metallic medical implants in the human body: from ions to nanoparticles—a systematic analytical review. *Acta biomaterialia*. 2014 Jun 1;10(6):2379-403.
44. Jacobs JJ, Gilbert JL, Urban RM. Current concepts review—corrosion of metal orthopaedic implants. *Jbjs*. 1998 Feb 1;80(2):268-82.
45. Fallahnezhad K, Oskouei RH, Taylor M. Development of a fretting corrosion model for metallic interfaces using adaptive finite element analysis. *Finite Elements in Analysis and Design*. 2018 Sep 1;148:38-47.
46. Schwack F, Prigge F, Poll G. Finite element simulation and experimental analysis of false brinelling and fretting corrosion. *Tribology International*. 2018 Oct 1;126:352-62.
47. Beddoes J, Bucci K. The influence of surface condition on the localized corrosion of 316L stainless steel orthopaedic implants. *Journal of Materials Science: Materials in Medicine*. 1999 Jul;10(7):389-94.
48. Larsson C, von Steyern PV. Five-year follow-up of implant-supported Y-TZP and ZTA fixed dental prostheses. A randomized, prospective clinical trial comparing two different material systems. *International Journal of Prosthodontics*. 2010 Nov 1;23(6).
49. Perrichon A, Liu BH, Chevalier J, Gremillard L, Reynard B, Farizon F, Liao JD, Geringer J. Ageing, shocks and wear mechanisms in ZTA and the long-term performance of hip joint materials. *Materials*. 2017 Jun;10(6):569.

50. Harman MK, Banks SA, Hodge WA. Wear analysis of a retrieved hip implant with titanium nitride coating. *The Journal of arthroplasty*. 1997 Dec 1;12(8):938-45.
51. Higgs G, Hanzlik J, MacDonald D, Kane W, Day J, Klein G, Parvizi J, Mont M, Kraay M, Martell J, Gilbert J. Method of characterizing fretting and corrosion at the various taper connections of retrieved modular components from metal-on-metal total hip arthroplasty. In *Metal-on-metal total hip replacement devices 2013* May. ASTM International.
52. Pivec R, Meneghini RM, Hozack WJ, Westrich GH, Mont MA. Modular taper junction corrosion and failure: how to approach a recalled total hip arthroplasty implant. *The Journal of arthroplasty*. 2014 Jan 1;29(1):1-6.
53. Gilbert JL, Mali S, Urban RM, Silverton CD, Jacobs JJ. In vivo oxide - induced stress corrosion cracking of Ti - 6Al - 4V in a neck - stem modular taper: Emergent behavior in a new mechanism of in vivo corrosion. *Journal of Biomedical Materials Research Part B: Applied Biomaterials*. 2012 Feb;100(2):584-94.
54. Rodrigues DC, Urban RM, Jacobs JJ, Gilbert JL. In vivo severe corrosion and hydrogen embrittlement of retrieved modular body titanium alloy hip - implants. *Journal of Biomedical Materials Research Part B: Applied Biomaterials: An Official Journal of The Society for Biomaterials, The Japanese Society for Biomaterials, and The Australian Society for Biomaterials and the Korean Society for Biomaterials*. 2009 Jan;88(1):206-19.

55. Gilbert JL, Buckley CA, Jacobs JJ. In vivo corrosion of modular hip prosthesis components in mixed and similar metal combinations. The effect of crevice, stress, motion, and alloy coupling. *Journal of biomedical materials research*. 1993 Dec;27(12):1533-44.
56. Hallab NJ, Messina C, Skipor A, Jacobs JJ. Differences in the fretting corrosion of metal–metal and ceramic–metal modular junctions of total hip replacements. *Journal of Orthopaedic Research*. 2004 Mar;22(2):250-9.
57. Sadiq K, Stack MM, Black RA. Wear mapping of CoCrMo alloy in simulated bio-tribocorrosion conditions of a hip prosthesis bearing in calf serum solution. *Materials Science and Engineering: C*. 2015 Apr 1;49:452-62.
58. Khullar P, Zhu D, Gilbert JL. Fretting corrosion of Si₃N₄ vs CoCrMo femoral heads on Ti - 6Al - V trunnions. *J. Orthop. Res*. 2020 Apr 38 (7); 1617–1626
59. Fregly BJ, Sawyer WG, Harman MK, Banks SA. Computational wear prediction of a total knee replacement from in vivo kinematics. *Journal of biomechanics*. 2005 Feb 1;38(2):305-14.
60. Harman MK, Banks SA, Hodge WA. Wear analysis of a retrieved hip implant with titanium nitride coating. *The Journal of arthroplasty*. 1997 Dec 1;12(8):938-45.
61. Alam F, Kumar A, Patel AK, Sharma RK, Balani K. Processing, characterization and fretting wear of zinc oxide and silver nanoparticles reinforced ultra high molecular weight polyethylene biopolymer nanocomposite. *Jom*. 2015 Apr 1;67(4):688-701.

62. Panigrahi P, Durig N, Alvarez E, Harman MK. Damage from unintentional metal–metal articulation of CoCrMo, TiAlV, and oxidized zirconium knee replacements following polyethylene insert failure. *Wear*. 2015 Feb 15;324:1-9.
63. Barril S, Mischler S, Landolt D. Influence of fretting regimes on the tribocorrosion behaviour of Ti6Al4V in 0.9 wt.% sodium chloride solution. *Wear*. 2004 May 1;256(9-10):963-72.
64. Barril S, Debaud N, Mischler S, Landolt D. A tribo-electrochemical apparatus for in vitro investigation of fretting–corrosion of metallic implant materials. *Wear*. 2002 May 1;252(9-10):744-54.
65. Benson LC, DesJardins JD, Harman MK, LaBerge M. Effect of stair descent loading on ultra-high molecular weight polyethylene wear in a force-controlled knee simulator. *Proceedings of the Institution of Mechanical Engineers, Part H: Journal of Engineering in Medicine*. 2002 Jun 1;216(6):409-18.
66. Geringer J, Forest B, Combrade P. Fretting-corrosion of materials used as orthopaedic implants. *Wear*. 2005 Jul 1;259(7-12):943-51.
67. Kim K, Geringer J, Pellier J, Macdonald DD. Fretting corrosion damage of total hip prosthesis: Friction coefficient and damage rate constant approach. *Tribology International*. 2013 Apr 1;60:10-8.
68. Muñoz AI, Mischler S. Effect of the environment on wear ranking and corrosion of biomedical CoCrMo alloys. *Journal of Materials Science: Materials in Medicine*. 2011 Mar 1;22(3):437-50.

69. Munoz AI, Mischler S. Interactive effects of albumin and phosphate ions on the corrosion of CoCrMo implant alloy. *Journal of the electrochemical Society*. 2007 Aug 13;154(10):C562.
70. Zhang E, Liu C. A new antibacterial Co-Cr-Mo-Cu alloy: Preparation, biocorrosion, mechanical and antibacterial property. *Materials Science and Engineering: C*. 2016 Dec 1;69:134-43.
71. Pearson MJ, Williams RL, Floyd H, Bodansky D, Grover LM, Davis ET, Lord JM. The effects of cobalt–chromium–molybdenum wear debris in vitro on serum cytokine profiles and T cell repertoire. *Biomaterials*. 2015 Oct 1;67:232-9.
72. Urban RM, Jacobs JJ, Gilbert JL, Rice SB, Jasty M, Bragdon CR, Galante JO. Characterization of solid products of corrosion generated by modular-head femoral stems of different designs and materials. In *Modularity of orthopedic implants* 1997 Jan. ASTM International.
73. De Martino I, Assini JB, Elpers ME, Wright TM, Westrich GH. Corrosion and fretting of a modular hip system: a retrieval analysis of 60 rejuvenate stems. *The Journal of arthroplasty*. 2015 Aug 1;30(8):1470-5.
74. Gill IP, Webb J, Sloan K, Beaver RJ. Corrosion at the neck-stem junction as a cause of metal ion release and pseudotumour formation. *The Journal of bone and joint surgery. British volume*. 2012 Jul;94(7):895-900.
75. Cooper HJ, Della Valle CJ, Berger RA, Tetreault M, Paprosky WG, Sporer SM, Jacobs JJ. Corrosion at the head-neck taper as a cause for adverse local tissue

- reactions after total hip arthroplasty. *The Journal of bone and joint surgery. American volume*. 2012 Sep 19;94(18):1655.
76. Zhu D, "DEVELOPMENT OF A "2-D" TEST SYSTEM FOR VISUALIZING FRETTING CORROSION: A STUDY OF THE FRETTING CORROSION BEHAVIOR OF Co-Cr-Mo ALLOY" (2016). *Dissertations - ALL*. 497.
<https://surface.syr.edu/etd/497>
77. ASTM F1537-20, Standard Specification for Wrought Cobalt-28Chromium-6Molybdenum Alloys for Surgical Implants (UNS R31537, UNS R31538, and UNS R31539), ASTM International, West Conshohocken, PA, 2020, 3.
78. Lu F, Royle M, Lali FV, Hart AJ, Collins S, Housden J, Shelton JC. Simple isolation method for the bulk isolation of wear particles from metal on metal bearing surfaces generated in a hip simulator test. *Journal of Materials Science: Materials in Medicine*. 2012 Apr 1;23(4):891-901.
79. Pedersen A, Kjelleberg S, Hermansson M. A screening method for bacterial corrosion of metals. *Journal of microbiological methods*. 1988 Aug 1;8(4):191-8.
80. Missert N, Barbour JC, Copeland RG, Mikkalson JE. The localized corrosion of Al at engineered Cu islands. *Jom*. 2001 Jul 1;53(7):34-6.
81. Stevenson H, Parkes M, Austin L, Jaggard M, Akhbari P, Vaghela U, Williams HR, Gupte C, Cann P. The development of a small-scale wear test for CoCrMo specimens with human synovial fluid. *Biotribology*. 2018 Jun 1;14:1-0.
82. Cobb AG, Schmalzreid TP. The clinical significance of metal ion release from cobalt-chromium metal-on-metal hip joint arthroplasty. *Proceedings of the*

- Institution of Mechanical Engineers, Part H: Journal of Engineering in Medicine. 2006 Feb 1;220(2):385-98.
83. Vendittoli PA, Amzica T, Roy AG, Lusignan D, Girard J, Lavigne M. Metal ion release with large-diameter metal-on-metal hip arthroplasty. *The Journal of arthroplasty*. 2011 Feb 1;26(2):282-8.
84. Milošev I, Strehblow HH. The composition of the surface passive film formed on CoCrMo alloy in simulated physiological solution. *Electrochimica Acta*. 2003 Aug 15;48(19):2767-74.
85. Yan Y, Neville A, Dowson D. Biotribocorrosion—an appraisal of the time dependence of wear and corrosion interactions: I. The role of corrosion. *Journal of Physics D: applied physics*. 2006 Jul 21;39(15):3200.
86. Bettini E, Leygraf C, Lin C, Liu P, Pan J. Influence of grain boundaries on dissolution behavior of a biomedical CoCrMo alloy: in-situ electrochemical-optical, AFM and SEM/TEM studies. *Journal of The Electrochemical Society*. 2012 Aug 14;159(9):C422.
87. Hoffman EE, Lin A, Liao Y, Marks LD. Grain boundary assisted crevice corrosion in CoCrMo alloys. *Corrosion*. 2016 Nov;72(11):1445-61.
88. Panigrahi P, Liao Y, Mathew MT, Fischer A, Wimmer MA, Jacobs JJ, Marks LD. Intergranular pitting corrosion of CoCrMo biomedical implant alloy. *Journal of Biomedical Materials Research Part B: Applied Biomaterials*. 2014 May;102(4):850-9.

89. Liu Y, Gilbert JL. Effect of simulated inflammatory conditions and potential on dissolution and surface oxide of CoCrMo alloy: In situ electrochemical atomic force microscopy study. *Electrochimica Acta*. 2018 Feb 1;262:252-63.
90. Liu Y, Zhu D, Pierre D, Gilbert JL. Fretting initiated crevice corrosion of 316LVM stainless steel in physiological phosphate buffered saline: Potential and cycles to initiation. *Acta biomaterialia*. 2019 Oct 1;97:565-77.
91. Gilbert JL, Buckley CA, Jacobs JJ. In vivo corrosion of modular hip prosthesis components in mixed and similar metal combinations. The effect of crevice, stress, motion, and alloy coupling. *Journal of biomedical materials research*. 1993 Dec;27(12):1533-44.
92. Urban RM, Jacobs JJ, Gilbert JL, Galante JO. Migration of corrosion products from modular hip prostheses. Particle microanalysis and histopathological findings. *JBJS*. 1994 Sep 1;76(9):1345-59.
93. Goldberg JR, Gilbert JL, Jacobs JJ, Bauer TW, Paprosky W, Leurgans S. A multicenter retrieval study of the taper interfaces of modular hip prostheses. *Clinical Orthopaedics and Related Research*. 2002 Aug 1;401:149-61.
94. Cooper HJ, Della Valle CJ, Berger RA, Tetreault M, Paprosky WG, Sporer SM, Jacobs JJ. Corrosion at the head-neck taper as a cause for adverse local tissue reactions after total hip arthroplasty. *The Journal of bone and joint surgery. American volume*. 2012 Sep 19;94(18):1655.

95. Liu Y, Zhu D, Pierre D, Gilbert JL. Fretting initiated crevice corrosion of 316LVM stainless steel in physiological phosphate buffered saline: Potential and cycles to initiation. *Acta biomaterialia*. 2019 Oct 1;97:565-77.
96. Oladokun A, Pettersson M, Bryant M, Engqvist H, Persson C, Hall R, Neville A. Fretting of CoCrMo and Ti6Al4V alloys in modular prostheses. *Tribology- Materials, Surfaces & Interfaces*. 2015 Oct 2;9(4):165-73.
97. Bryant M, Neville A. Fretting corrosion of CoCr alloy: Effect of load and displacement on the degradation mechanisms. *Proceedings of the Institution of Mechanical Engineers, Part H: Journal of Engineering in Medicine*. 2017 Feb;231(2):114-26.
98. Swaminathan V, Gilbert JL. Fretting corrosion of CoCrMo and Ti6Al4V interfaces. *Biomaterials*. 2012 Aug 1;33(22):5487-503.
99. Papageorgiou N. The relevance of cathode kinetics to the interpretation of triboelectrochemical corrosion. *Tribology International*. 2013 Oct 1;66:60-71.
100. Maldonado SG, Mischler S, Cantoni M, Chitty WJ, Falcand C, Hertz D. Mechanical and chemical mechanisms in the tribocorrosion of a Stellite type alloy. *Wear*. 2013 Nov 30;308(1-2):213-21.
101. Swaminathan V, Gilbert JL. Potential and frequency effects on fretting corrosion of Ti6Al4V and CoCrMo surfaces. *Journal of Biomedical Materials Research Part A*. 2013 Sep;101(9):2602-12.
102. Jiang J, Stack MM, Neville A. Modelling the tribo-corrosion interaction in aqueous sliding conditions. *Tribology International*. 2002 Oct 1;35(10):669-79.

103. Jemmely P, Mischler S, Landolt D. Electrochemical modeling of passivation phenomena in tribocorrosion. *Wear*. 2000 Jan 1;237(1):63-76.
104. Landolt D, Mischler S, Stemp M. Electrochemical methods in tribocorrosion: a critical appraisal. *Electrochimica acta*. 2001 Aug 15;46(24-25):3913-29.
105. Papageorgiou N, Mischler S. Electrochemical simulation of the current and potential response in sliding tribocorrosion. *Tribology Letters*. 2012 Dec 1;48(3):271-83.
106. Kolman DG, Scully JR. Limitations of potentiostatic repassivation techniques and their relationship to the applicability of the high field approximation to the repassivation of titanium. *Journal of the Electrochemical Society*. 1995 Jul 1;142(7):2179.
107. Kolman DG, Scully JR. On the Repassivation Behavior of High - Purity Titanium and Selected α , β , and $\beta + \alpha$ Titanium Alloys in Aqueous Chloride Solutions. *Journal of the Electrochemical Society*. 1996 Jun 1;143(6):1847.
108. Kolman DG, Gaudett MA, Scully JR. Modeling of anodic current transients resulting from oxide rupture of plastically strained $\beta + \alpha$ titanium. *Journal of the Electrochemical Society*. 1998 Jun 1;145(6):1829.
109. Kolman DG, Scully JR. Continuum mechanics characterization of plastic deformation-induced oxide film rupture. *Philosophical Magazine A*. 1999 Oct 1;79(10):2313-38.

110. Gilbert JL, Mali SA, Liu Y. Area-dependent impedance-based voltage shifts during tribocorrosion of Ti-6Al-4V biomaterials: theory and experiment. *Surface Topography: Metrology and Properties*. 2016 Jun 24;4(3):034002.
111. Gilbert JL, Buckley CA, Lautenschlager EP. Titanium oxide film fracture and repassivation: the effect of potential, pH and aeration. In *Medical applications of titanium and its alloys: The material and biological issues* 1996 Jan. ASTM International.
112. Goldberg JR, Gilbert JL. Electrochemical response of CoCrMo to high - speed fracture of its metal oxide using an electrochemical scratch test method. *Journal of Biomedical Materials Research: An Official Journal of The Society for Biomaterials and The Japanese Society for Biomaterials*. 1997 Dec 5;37(3):421-31.
113. Scully JC. Stress corrosion cracking. In *Treatise on Materials Science and Technology* 1983 Jan 1 (Vol. 23, pp. 103-174). Elsevier.
114. Cabrera NF, Mott NF. Theory of the oxidation of metals. *Reports on progress in physics*. 1949 Jan 1;12(1):163-84.
115. Gunterschulze A and Betz H. *Elektrolyt-Kondensatoren* (Herbert Cram, Berlin, 1937; Oborongiz, Moscow, 1938) [in German and Russian].
116. Jones DA. *Principles and prevention of corrosion*. Macmillan; 1992.
117. Olsson CO, Hamm D, Landolt D. Evaluation of passive film growth models with the electrochemical quartz crystal microbalance on PVD deposited Cr. *Journal of the Electrochemical Society*. 2000 Nov 1;147(11):4093.

118. Popov VL. Contact mechanics and friction. Berlin, Heidelberg: Springer Berlin Heidelberg; 2010.
119. Peer Wiley CR. Advanced Engineering Mathematics 4th Edition, (New York, NY: McGraw Hill) 1975: 313.
120. Goldberg JR, Gilbert JL. The electrochemical and mechanical behavior of passivated and TiN/AlN-coated CoCrMo and Ti6Al4V alloys. *Biomaterials*. 2004 Feb 1;25(5):851-64.
121. Zhu D, "DEVELOPMENT OF A “2-D” TEST SYSTEM FOR VISUALIZING FRETTING CORROSION: A STUDY OF THE FRETTING CORROSION BEHAVIOR OF Co-Cr-Mo ALLOY" (2016). Dissertations - ALL. 497.
<https://surface.syr.edu/etd/497>
122. Aladjem A. Anodic oxidation of titanium and its alloys. *Journal of Materials Science*. 1973 May 1;8(5):688-704.
123. Ehrensberger MT, Sivan S, Gilbert JL. Titanium is not “the most biocompatible metal” under cathodic potential: The relationship between voltage and MC3T3 preosteoblast behavior on electrically polarized cpTi surfaces. *Journal of Biomedical Materials Research Part A: An Official Journal of The Society for Biomaterials, The Japanese Society for Biomaterials, and The Australian Society for Biomaterials and the Korean Society for Biomaterials*. 2010 Jun 15;93(4):1500-9.

124. Haeri M, Wöllert T, Langford GM, Gilbert JL. Electrochemical control of cell death by reduction-induced intrinsic apoptosis and oxidation-induced necrosis on CoCrMo alloy in vitro. *Biomaterials*. 2012 Sep 1;33(27):6295-304.
125. Sivan S, Kaul S, Gilbert JL. The effect of cathodic electrochemical potential of Ti - 6Al - 4V on cell viability: Voltage threshold and time dependence. *Journal of Biomedical Materials Research Part B: Applied Biomaterials*. 2013 Nov;101(8):1489-97.
126. Hui T, Kubacki GW, Gilbert JL. Voltage and wear debris from Ti - 6Al - 4V interact to affect cell viability during in - vitro fretting corrosion. *Journal of Biomedical Materials Research Part A*. 2018 Jan;106(1):160-7.
127. Q. Chen, G.A. Thouas, *Metallic implant biomaterials*, Mater. Sci. Eng. R Rep. 2015 Jan 87: 1–57
128. Navarro M, Michiardi A, Castano O, Planell JA. Biomaterials in orthopaedics. *Journal of the royal society interface*. 2008 Oct 6;5(27):1137-58.
129. Gilbert JL. 1.2 Electrochemical Behavior of Metals in the Biological Milieu. *Comprehensive Biomaterials II*. 2017 Jan 1:19.
130. Virtanen S, Milošev I, Gomez-Barrena E, Trebše R, Salo J, Konttinen YT. Special modes of corrosion under physiological and simulated physiological conditions. *Acta Biomaterialia*. 2008 May 1;4(3):468-76.
131. Gilbert JL, Bai Z, Bearinger J, Megremis S. The dynamics of oxide films on metallic biomaterials. In *Medical Device Materials. Proceedings of Materials and*

- Processes for Medical Devices Conference. Materials Park, OH: ASM International 2004 (pp. 139-143).
132. Kocijan A, Donik Č, Jenko M. Electrochemical and XPS studies of the passive film formed on stainless steels in borate buffer and chloride solutions. *Corrosion science*. 2007 May 1;49(5):2083-98.
133. Sivakumar M, Dhanadurai KS, Rajeswari S, Thulasiraman V. Failures in stainless steel orthopaedic implant devices: A survey. *Journal of materials science letters*. 1995 May 1;14(5):351-4.
134. Voggenreiter G, Leiting S, Brauer H, Leiting P, Majetschak M, Bardenheuer M, Obertacke U. Immuno-inflammatory tissue reaction to stainless-steel and titanium plates used for internal fixation of long bones. *Biomaterials*. 2003 Jan 1;24(2):247-54.
135. Soultanis KC, Pyrovolou N, Zahos KA, Karaliotas GI, Lenti A, Liveris I, Babis GC, Soucacos PN. Late postoperative infection following spinal instrumentation: stainless steel versus titanium implants. *Journal of surgical orthopaedic advances*. 2008 Jan 1;17(3):193-9.
136. Case CP, Langkamer VG, James C, Palmer MR, Kemp AJ, Heap PF, Solomon L. Widespread dissemination of metal debris from implants. *The Journal of bone and joint surgery. British volume*. 1994 Sep;76(5):701-12.
137. Maloney WJ, Smith RL. Periprosthetic osteolysis in total hip arthroplasty: the role of particulate wear debris. *JBJS*. 1995 Sep 1;77(9):1448-61.

138. Sivakumar M, Rajeswari S. Investigation of failures in stainless steel orthopaedic implant devices: pit-induced stress corrosion cracking. *Journal of Materials Science Letters*. 1992 Jan 1;11(15):1039-42.
139. Gilbert JL, Buckley CA, Jacobs JJ. In vivo corrosion of modular hip prosthesis components in mixed and similar metal combinations. The effect of crevice, stress, motion, and alloy coupling. *Journal of biomedical materials research*. 1993 Dec;27(12):1533-44.
140. Liu Y. The effects of simulated inflammatory conditions on the corrosion and fretting corrosion of CoCrMo alloy. Syracuse University, 2017, Retrieved from <https://surface.syr.edu/etd/705/>.
141. Meyer H, Mueller T, Goldau G, Chamaon K, Ruetschi M, Lohmann CH. Corrosion at the cone/taper interface leads to failure of large-diameter metal-on-metal total hip arthroplasties. *Clinical Orthopaedics and Related Research®*. 2012 Nov 1;470(11):3101-8.
142. Cooper HJ, Della Valle CJ, Berger RA, Tetreault M, Paprosky WG, Sporer SM, Jacobs JJ. Corrosion at the head-neck taper as a cause for adverse local tissue reactions after total hip arthroplasty. *The Journal of bone and joint surgery. American volume*. 2012 Sep 19;94(18):1655.
143. Swaminathan V, Gilbert JL. Fretting corrosion of CoCrMo and Ti6Al4V interfaces. *Biomaterials*. 2012 Aug 1;33(22):5487-503.
144. Geringer J, Forest B, Combrade P. Fretting-corrosion of materials used as orthopaedic implants. *Wear*. 2005 Jul 1;259(7-12):943-51.

145. Gilbert JL, Mali SA, Liu Y. Area-dependent impedance-based voltage shifts during tribocorrosion of Ti-6Al-4V biomaterials: theory and experiment. *Surface Topography: Metrology and Properties*. 2016 Jun 24;4(3):034002
146. Barril S, Mischler S, Landolt D. Electrochemical effects on the fretting corrosion behaviour of Ti6Al4V in 0.9% sodium chloride solution. *Wear*. 2005 Jul 1;259(1-6):282-91.
147. Stockert L, Boehni H. Susceptibility to crevice corrosion and metastable pitting of stainless steels. In *Materials Science Forum 1989* (Vol. 44, pp. 313-328). Trans Tech Publications Ltd.
148. Oldfield JW, Sutton WH. Crevice corrosion of stainless steels: II. Experimental studies. *British Corrosion Journal*. 1978 Jan 1;13(3):104-11.
149. Oldfield JW, Sutton WH. Crevice corrosion of stainless steels: I. a mathematical model. *British corrosion journal*. 1978 Jan 1;13(1):13-22.
150. Pickering HW, Frankenthal RP. On the mechanism of localized corrosion of iron and stainless steel: I. Electrochemical studies. *journal of the Electrochemical Society*. 1972 Oct 1;119(10):1297.
151. Xu Y, Pickering HW. The initial potential and current distributions of the crevice corrosion process. *Journal of the electrochemical society*. 1993 Mar 1;140(3):658.
152. Punckt C, Bölscher M, Rotermund HH, Mikhailov AS, Organ L, Budiansky N, Scully JR, Hudson JL. Sudden onset of pitting corrosion on stainless steel as a critical phenomenon. *Science*. 2004 Aug 20;305(5687):1133-6.

153. Leckie HP, Uhlig HH. Environmental factors affecting the critical potential for pitting in 18–8 stainless steel. *Journal of the electrochemical society*. 1966 Dec 1;113(12):1262.
154. Szklarska-Smialowska Z, Mankowski J. Crevice corrosion of stainless steels in sodium chloride solution. *Corrosion Science*. 1978 Jan 1;18(11):953-60.
155. Hu Q, Zhang G, Qiu Y, Guo X. The crevice corrosion behaviour of stainless steel in sodium chloride solution. *Corrosion science*. 2011 Dec 1;53(12):4065-72.
156. Brown SA, Flemming CA, Kawalec JS, Placko HE, Vassaux C, Merritt K, Payer JH, Kraay MJ. Fretting corrosion accelerates crevice corrosion of modular hip tapers. *Journal of Applied Biomaterials*. 1995 Mar;6(1):19-26.
157. Gilbert JL, Mehta M, Pinder B. Fretting crevice corrosion of stainless steel stem–CoCr femoral head connections: comparisons of materials, initial moisture, and offset length. *Journal of Biomedical Materials Research Part B: Applied Biomaterials: An Official Journal of The Society for Biomaterials, The Japanese Society for Biomaterials, and The Australian Society for Biomaterials and the Korean Society for Biomaterials*. 2009 Jan;88(1):162-73.
158. Mali SA, Singh V, Gilbert JL. Effect of mixed alloy combinations on fretting corrosion performance of spinal screw and rod implants. *Journal of Biomedical Materials Research Part B: Applied Biomaterials*. 2017 Jul;105(5):1169-77.
159. Zhu D, "DEVELOPMENT OF A “2-D” TEST SYSTEM FOR VISUALIZING FRETTING CORROSION: A STUDY OF THE FRETTING CORROSION

- BEHAVIOR OF Co-Cr-Mo ALLOY" (2016). Dissertations - ALL. 497.
<https://surface.syr.edu/etd/497>
160. Aoyama T, Sugawara Y, Muto I, Hara N. In situ monitoring of crevice corrosion morphology of Type 316L stainless steel and repassivation behavior induced by sulfate ions. *Corrosion Science*. 2017 Oct 1;127:131-40.
161. Liu Y, Gilbert JL. The effect of simulated inflammatory conditions and pH on fretting corrosion of CoCrMo alloy surfaces. *Wear*. 2017 Nov 15;390:302-11.
162. Liu Y, Gilbert JL. Effect of simulated inflammatory conditions and potential on dissolution and surface oxide of CoCrMo alloy: In situ electrochemical atomic force microscopy study. *Electrochimica Acta*. 2018 Feb 1;262:252-63.
163. Yang YZ, Jiang YM, Li J. In situ investigation of crevice corrosion on UNS S32101 duplex stainless steel in sodium chloride solution. *Corrosion science*. 2013 Nov 1;76:163-9.
164. Geringer J, Macdonald DD. Modeling fretting-corrosion wear of 316L SS against poly (methyl methacrylate) with the Point Defect Model: Fundamental theory, assessment, and outlook. *Electrochimica Acta*. 2012 Sep 30;79:17-30.
165. Abdulsalam MI, Pickering HW. The effect of crevice - opening dimension on the stability of crevice corrosion for nickel in sulfuric acid. *Journal of the Electrochemical Society*. 1998 Jul 1;145(7):2276.
166. Matsushima I, Sakai J, Masamura K. Mechanism of crevice corrosion. In *Proceedings of the Seventh International Congress on Metallic Corrosion, Rio De Janeiro, Brazil 1978 Oct 4*.

167. Geringer J, Atmani F, Forest B. Friction–corrosion of AISI 316L/bone cement and AISI 316L/PMMA contacts: Ionic strength effect on tribological behaviour. *Wear*. 2009 Jun 15;267(5-8):763-9.
168. Akazawa T, Minami S, Takahashi K, Kotani T, Hanawa T, Moriya H. Corrosion of spinal implants retrieved from patients with scoliosis. *Journal of Orthopaedic Science*. 2005 Mar 1;10(2):200-5.
169. Walczak J, Shahgaldi F, Heatley F. In vivo corrosion of 316L stainless-steel hip implants: morphology and elemental compositions of corrosion products. *Biomaterials*. 1998 Jan 1;19(1-3):229-37.
170. Kamachimudali U, Sridhar TM, Raj B. Corrosion of bio implants. *Sadhana*. 2003 Jun 1;28(3-4):601-37.
171. Eliades T, Pratsinis H, Kletsas D, Eliades G, Makou M. Characterization and cytotoxicity of ions released from stainless steel and nickel-titanium orthodontic alloys. *American journal of orthodontics and dentofacial orthopedics*. 2004 Jan 1;125(1):24-9.
172. Gibon E, Amanatullah DF, Loi F, Pajarinen J, Nabeshima A, Yao Z, Hamadouche M, Goodman SB. The biological response to orthopaedic implants for joint replacement: Part I: Metals. *Journal of Biomedical Materials Research Part B: Applied Biomaterials*. 2017 Oct;105(7):2162-73.
173. Liu Y, Gilbert JL. The effect of simulated inflammatory conditions and Fenton chemistry on the electrochemistry of CoCrMo alloy. *Journal of Biomedical Materials Research Part B: Applied Biomaterials*. 2018 Jan;106(1):209-20.

174. Brooks EK, Brooks RP, Ehrensberger MT. Effects of simulated inflammation on the corrosion of 316L stainless steel. *Materials Science and Engineering: C*. 2017 Feb 1;71:200-5.
175. Blackwood DJ, Pereira BP. No corrosion of 304 stainless steel implant after 40 years of service. *Journal of Materials Science: Materials in Medicine*. 2004 Jul 1;15(7):755-8.
176. Gilbert JL, Sivan S, Liu Y, Kocagöz SB, Arnholt CM, Kurtz SM. Direct in vivo inflammatory cell - induced corrosion of CoCrMo alloy orthopedic implant surfaces. *Journal of Biomedical Materials Research Part A*. 2015 Jan;103(1):211-23.
177. Di Laura A, Hothi HS, Meswania JM, Whittaker RK, de Villiers D, Zustin J, Blunn GW, Skinner JA, Hart AJ. Clinical relevance of corrosion patterns attributed to inflammatory cell-induced corrosion: A retrieval study. *Journal of Biomedical Materials Research Part B: Applied Biomaterials*. 2017 Jan;105(1):155-64.
178. Yu F, Addison O, Davenport AJ. A synergistic effect of albumin and H₂O₂ accelerates corrosion of Ti6Al4V. *Acta biomaterialia*. 2015 Oct 15;26:355-65.
179. Simoes TA, Bryant MG, Brown AP, Milne SJ, Ryan M, Neville A, Brydson R. Evidence for the dissolution of molybdenum during tribocorrosion of CoCrMo hip implants in the presence of serum protein. *Acta Biomaterialia*. 2016 Nov 1;45:410-8.

180. Patterson SP, Daffner RH, Gallo RA. Electrochemical corrosion of metal implants. *American Journal of Roentgenology*. 2005 Apr;184(4):1219-22.
181. Gilbert JL. 1.2 Electrochemical Behavior of Metals in the Biological Milieu. *Comprehensive Biomaterials II*. 2017 Jan 1:19.
182. Yaszemski MJ. *Biomaterials in orthopedics*. CRC Press; 2003 Oct 17.
183. Gilbert JL. Corrosion in the human body: Metallic implants in the complex body environment. *Corrosion*. 2017 Dec 1;73(12):1478-95.
184. Gkagkalis G, Mettraux P, Omoumi P, Mischler S, Rüdiger HA. Adverse tissue reaction to corrosion at the neck-stem junction after modular primary total hip arthroplasty. *Orthopaedics & Traumatology: Surgery & Research*. 2015 Feb 1;101(1):123-6.
185. Pearson MJ, Williams RL, Floyd H, Bodansky D, Grover LM, Davis ET, Lord JM. The effects of cobalt–chromium–molybdenum wear debris in vitro on serum cytokine profiles and T cell repertoire. *Biomaterials*. 2015 Oct 1;67:232-9.
186. Gibon E, Amanatullah DF, Loi F, Pajarinen J, Nabeshima A, Yao Z, Hamadouche M, Goodman SB. The biological response to orthopaedic implants for joint replacement: Part I: Metals. *Journal of Biomedical Materials Research Part B: Applied Biomaterials*. 2017 Oct;105(7):2162-73.
187. Cook RB, Bolland BJ, Wharton JA, Tilley S, Latham JM, Wood RJ. Pseudotumour formation due to tribocorrosion at the taper interface of large diameter metal on polymer modular total hip replacements. *The Journal of arthroplasty*. 2013 Sep 1;28(8):1430-6.

188. Doorn PF, Mirra JM, Campbell PA, Amstutz HC. Tissue reaction to metal on metal total hip prostheses. *Clinical Orthopaedics and Related Research* (1976-2007). 1996 Aug 1;329:S187-205.
189. Gilbert JL, Buckley CA, Jacobs JJ. In vivo corrosion of modular hip prosthesis components in mixed and similar metal combinations. The effect of crevice, stress, motion, and alloy coupling. *Journal of biomedical materials research*. 1993 Dec;27(12):1533-44.
190. Goldberg JR, Gilbert JL, Jacobs JJ, Bauer TW, Paprosky W, Leurgans S. A multicenter retrieval study of the taper interfaces of modular hip prostheses. *Clinical Orthopaedics and Related Research*®. 2002 Aug 1;401:149-61.
191. Atwood SA, Patten EW, Bozic KJ, Pruitt LA, Ries MD. Corrosion-induced fracture of a double-modular hip prosthesis: a case report. *JBJS*. 2010 Jun 1;92(6):1522-5.
192. Grupp TM, Weik T, Bloemer W, Knaebel HP. Modular titanium alloy neck adapter failures in hip replacement-failure mode analysis and influence of implant material. *BMC musculoskeletal disorders*. 2010 Dec;11(1):1-2.
193. Capello WN, D'Antonio JA, Feinberg JR, Manley MT, Naughton M. Ceramic-on-ceramic total hip arthroplasty: update. *The Journal of arthroplasty*. 2008 Oct 1;23(7):39-43.
194. Zhou YS, Ikeuchi K, Ohashi M. Comparison of the friction properties of four ceramic materials for joint replacements. *Wear*. 1997 Sep 1;210(1-2):171-7.

195. Hallab NJ, Messina C, Skipor A, Jacobs JJ. Differences in the fretting corrosion of metal–metal and ceramic–metal modular junctions of total hip replacements. *Journal of Orthopaedic Research*. 2004 Mar;22(2):250-9.
196. Barrack RL, Burak C, Skinner HB. Concerns about ceramics in THA. *Clinical Orthopaedics and Related Research (1976-2007)*. 2004 Dec 1;429:73-9.
197. e Silva CG, Higa OZ, Bressiani JC. Cytotoxic evaluation of silicon nitride-based ceramics. *Materials Science and Engineering: C*. 2004 Nov 1;24(5):643-6.
198. Howlett CR, McCartney E, Ching W. The effect of silicon nitride ceramic on rabbit skeletal cells and tissue: An in vitro and in vivo investigation. *Clinical Orthopaedics and Related Research®*. 1989 Jul 1;244:293-304.
199. Rambo Jr WM. Treatment of lumbar discitis using silicon nitride spinal spacers: a case series and literature review. *International journal of surgery case reports*. 2018 Jan 1;43:61-8.
200. Boschetto F, Bock R, McEntire B, et al. Hinderance of bacterial proliferation by a silicon nitride surface buffering effect. 2019.
201. Zhou YS, Ohashi M, Tomita N, Ikeuchi K, Takashima K. Study on the possibility of silicon nitride—silicon nitride as a material for hip prostheses. *Materials Science and Engineering: C*. 1997 Dec 1;5(2):125-9.
202. Bal BS, Khandkar A, Lakshminarayanan R, Clarke I, Hoffman AA, Rahaman MN. Testing of silicon nitride ceramic bearings for total hip arthroplasty. *Journal of Biomedical Materials Research Part B: Applied Biomaterials: An Official Journal of The Society for Biomaterials, The Japanese Society for Biomaterials,*

- and The Australian Society for Biomaterials and the Korean Society for Biomaterials. 2008 Nov;87(2):447-54.
203. F04 Committee. [date unknown]. Specification for wrought Cobalt 28Chromium-6Molybdenum alloys for surgical implants (UNS R31537, UNS R31538, and UNS R31539). ASTM International.
204. Pierre D, Swaminathan V, Scholl L, TenHuisen K, Gilbert JL. Effects of seating load magnitude and load orientation on seating mechanics in 5° 40' mixed-alloy modular taper junctions. *Journal of biomechanics*. 2019 Jan 3;82:251-8.
205. Goldberg JR, Gilbert JL. In vitro corrosion testing of modular hip tapers. *Journal of Biomedical Materials Research Part B: Applied Biomaterials: An Official Journal of The Society for Biomaterials, The Japanese Society for Biomaterials, and The Australian Society for Biomaterials and the Korean Society for Biomaterials*. 2003 Feb 15;64(2):78-93.
206. F04 Committee. [date unknown]. Test method for determining the axial disassembly force of taper connections of modular prostheses. ASTM International
207. Goldberg JR, Gilbert JL. Electrochemical response of CoCrMo to high - speed fracture of its metal oxide using an electrochemical scratch test method. *Journal of Biomedical Materials Research: An Official Journal of The Society for Biomaterials and The Japanese Society for Biomaterials*. 1997 Dec 5;37(3):421-31.

208. Gilbert JL, Buckley CA, Lautenschlager EP. Titanium oxide film fracture and repassivation: the effect of potential, pH and aeration. In *Medical applications of titanium and its alloys: The material and biological issues* 1996 Jan. ASTM International.
209. Rowan FE, Wach A, Wright TM, Padgett DE. The onset of fretting at the head - stem connection in hip arthroplasty is affected by head material and trunnion design under simulated corrosion conditions. *Journal of Orthopaedic Research®*. 2018 Jun;36(6):1630-6.
210. Kyomoto M, Shoyama Y, Saiga K, Moro T, Ishihara K. Reducing fretting - initiated crevice corrosion in hip simulator tests using a zirconia - toughened alumina femoral head. *Journal of Biomedical Materials Research Part B: Applied Biomaterials*. 2018 Nov;106(8):2815-26.
211. Kocagoz SB, Underwood RJ, MacDonald DW, Gilbert JL, Kurtz SM. Ceramic heads decrease metal release caused by head-taper fretting and corrosion. *Clinical Orthopaedics and Related Research®*. 2016 Apr 1;474(4):985-94.
212. Bergmann G, Bender A, Dymke J, Duda G, Damm P. Standardized loads acting in hip implants. *PloS one*. 2016 May 19;11(5):e0155612.
213. Ouellette ES, Mali SA, Kim J, Grostefon J, Gilbert JL. Design, material, and seating load effects on in vitro fretting corrosion performance of modular head-neck tapers. *The Journal of arthroplasty*. 2019 May 1;34(5):991-1002.
214. Gilbert J, Mali S, Sivan S. Corrosion of modular tapers in total joint replacements: A critical assessment of design, materials, surface structure,

- mechanics, electrochemistry, and biology. In Modularity and tapers in total joint replacement devices 2015 Dec. ASTM International.
215. Khullar P, Zhu D, Gilbert JL. [date unknown]. Modular head-neck taper fretting mechanics: Si₃N₄ vs CoCrMo head on Ti-6Al-4V trunnion.
216. Langton DJ, Sidaginamale R, Lord JK, Nargol AV, Joyce TJ. Taper junction failure in large-diameter metal-on-metal bearings. Bone & joint research. 2012 Apr;1(4):56-63.
217. Panagiotidou A, Meswania J, Hua J, Muirhead - Allwood S, Hart A, Blunn G. Enhanced wear and corrosion in modular tapers in total hip replacement is associated with the contact area and surface topography. Journal of orthopaedic research. 2013 Dec;31(12):2032-9.
218. Pourzal R, Hall DJ, Ha NQ, Urban RM, Levine BR, Jacobs JJ, Lundberg HJ. Does surface topography play a role in taper damage in head-neck modular junctions?. Clinical Orthopaedics and Related Research®. 2016 Oct 1;474(10):2232-42.
219. Moharrami N, Langton DJ, Sayginer O, Bull SJ. Why does titanium alloy wear cobalt chrome alloy despite lower bulk hardness: A nanoindentation study?. Thin Solid Films. 2013 Dec 31;549:79-86.
220. Hall DJ, Pourzal R, Lundberg HJ, Mathew MT, Jacobs JJ, Urban RM. Mechanical, chemical and biological damage modes within head - neck tapers of CoCrMo and Ti6Al4V contemporary hip replacements. Journal of Biomedical Materials Research Part B: Applied Biomaterials. 2018 Jul;106(5):1672-85.

221. Arnholt CM, MacDonald DW, Underwood RJ, Guyer EP, Rimnac CM, Kurtz SM, Mont MA, Klein GR, Lee GC, Chen AF, Hamlin BR. Do stem taper microgrooves influence taper corrosion in total hip arthroplasty? A matched cohort retrieval study. *The Journal of arthroplasty*. 2017 Apr 1;32(4):1363-73.
222. Vendittoli PA, Amzica T, Roy AG, Lusignan D, Girard J, Lavigne M. Metal ion release with large-diameter metal-on-metal hip arthroplasty. *The Journal of arthroplasty*. 2011 Feb 1;26(2):282-8.
223. Hallab NJ, Cunningham BW, Jacobs JJ. Spinal implant debris-induced osteolysis. *Spine*. 2003 Oct 15;28(20S):S125-38.
224. Donati ME, Savarino L, Granchi D, Ciapetti G, Cervellati M, Rotini R, Pizzoferrato A. The effects of metal corrosion debris on immune system cells. *La Chirurgia degli organi di movimento*. 1998 Oct 1;83(4):387-93.
225. Lamaka S, Souto RM, Ferreira MG. In-situ visualization of local corrosion by Scanning Ion-selective Electrode Technique (SIET). *Microscopy: Science, technology, applications and education*. 2010;3:2162-73.
226. Bond JW. Visualization of latent fingerprint corrosion of metallic surfaces. *Journal of forensic sciences*. 2008 Jul;53(4):812-22.
227. Mathew MT, Abbey S, Hallab NJ, Hall DJ, Sukotjo C, Wimmer MA. Influence of pH on the tribocorrosion behavior of CpTi in the oral environment: synergistic interactions of wear and corrosion. *Journal of Biomedical Materials Research Part B: Applied Biomaterials*. 2012 Aug;100(6):1662-71.

228. Cao S, Maldonado SG, Mischler S. Tribocorrosion of passive metals in the mixed lubrication regime: theoretical model and application to metal-on-metal artificial hip joints. *Wear*. 2015 Feb 15;324:55-63.
229. Landolt D, Mischler S, Stemp M. Electrochemical methods in tribocorrosion: a critical appraisal. *Electrochimica acta*. 2001 Aug 15;46(24-25):3913-29.
230. Mathew MT, Wimmer MA. Tribocorrosion in artificial joints: in vitro testing and clinical implications. In *Tribocorrosion of passive metals and coatings 2011* Jan 1 (pp. 368-400). Woodhead Publishing.
231. Capello WN, D'Antonio JA, Feinberg JR, Manley MT, Naughton M. Ceramic-on-ceramic total hip arthroplasty: update. *The Journal of arthroplasty*. 2008 Oct 1;23(7):39-43.
232. Simoes TA, Brown AP, Milne SJ, Brydson RM. Bovine serum albumin binding to CoCrMo nanoparticles and the influence on dissolution. In *Journal of Physics: Conference Series* 2015 Sep 1 (Vol. 644, No. 1, p. 012039). IOP Publishing.
233. Gilbert JL, Sivan S, Liu Y, Kocagöz SB, Arnholt CM, Kurtz SM. Direct in vivo inflammatory cell - induced corrosion of CoCrMo alloy orthopedic implant surfaces. *Journal of Biomedical Materials Research Part A*. 2015 Jan;103(1):211-23.
234. Berbel LO, Banczek ED, Karousis IK, Kotsakis GA, Costa I. Determinants of corrosion resistance of Ti-6Al-4V alloy dental implants in an In Vitro model of peri-implant inflammation. *PloS one*. 2019 Jan 31;14(1):e0210530.

235. Hui T, Kubacki GW, Gilbert JL. Voltage and wear debris from Ti - 6Al - 4V interact to affect cell viability during in - vitro fretting corrosion. *Journal of Biomedical Materials Research Part A*. 2018 Jan;106(1):160-7.
236. Rovetta F, Stacchiotti A, Faggi F, Catalani S, Apostoli P, Fanzani A, Aleo MF. Cobalt triggers necrotic cell death and atrophy in skeletal C2C12 myotubes. *Toxicology and applied pharmacology*. 2013 Sep 1;271(2):196-205.
237. Gallo J, Barry Goodman S, Lostak J, Janout M. Advantages and disadvantages of ceramic on ceramic total hip arthroplasty: a review. *Biomedical papers*. 2012 Sep 1;156(3):204-12.

Curriculum vitae

Dongkai Zhu

Doctoral Candidate
Clemson-MUSC Bioengineering Program
Clemson University
Charleston, 29425

Email: dongkaz@clemson.edu
Phone: (315)391-0385

Professional Preparation:

Capital Medical University 2013	Prosthetics and Orthotics Engineering	B.E.
Syracuse University 2016	Biomedical and Chemical Engineering	M.S.
Clemson University 2021	Bioengineering	Ph.D.

Appointments:

Summer 2017	Graduate Research Assistant
Fall 2017	Graduate Research Assistant
Spring 2018	Graduate Research Assistant
Summer 2018	Graduate Research Assistant
Fall 2018	Graduate Research Assistant
Spring 2019	Graduate Research Assistant
Summer 2019	Graduate Research Assistant
Fall 2019	Graduate Research Assistant
Spring 2020	Graduate Research Assistant
Summer 2020	Graduate Research Assistant
Fall 2020	Graduate Research Assistant

Journal Publications:

1. Liu Y, **Zhu D**, Pierre D, Gilbert JL. Fretting initiated crevice corrosion of 316LVM stainless steel in physiological phosphate buffered saline: Potential and cycles to initiation. *Acta Biomaterialia*. 2019 Oct 1;97:565-77.
2. Smith SM, **Zhu D**, Pierre D, Gilbert JL, Chinn JA. Effect of multipurpose care solutions upon physical dimensions of silicone hydrogel contact lenses. *Journal of Biomedical Materials Research Part B: Applied Biomaterials*. 2020 Jul;108(5):1915-24.
3. Gilbert JL, **Zhu D**. A metallic biomaterial tribocorrosion model linking fretting mechanics, currents, and potentials: Model development and experimental comparison. *Journal of Biomedical Materials Research Part B: Applied Biomaterials*. 2020 Nov;108(8):3174-89.

4. Khullar P, **Zhu D**, Gilbert JL. Fretting corrosion of Si₃N₄ vs CoCrMo femoral heads on Ti-6Al-4V trunnions. *Journal of Orthopaedic Research*®. 2020 Jul;38(7):1617-26.
5. **Zhu D**, Liu Y, Gilbert JL. In vitro fretting crevice corrosion damage of CoCrMo alloys in phosphate buffered saline: Debris generation, chemistry and distribution. *Acta Biomaterialia*. 2020 Sep 15;114:449-59.
6. Vo A, Feng X, Smith W, **Zhu D**, Patel M, Kozak D, Wang Y, Zheng J, Ashraf M, Xu X. Analyzing Ophthalmic Suspension Particle Size Distributions Using Laser Diffraction: Placebo Background Subtraction Method. *International Journal of Pharmaceutics*. 2021 Feb 23:120401.

Conference Presentations & Posters:

1. **Zhu D**, Gilbert JL. “Development of a “2-D” Test System for Visualizing Fretting Corrosion: A Study of the Fretting Corrosion Behavior of CoCrMo Alloy”. Annual Meeting of the Orthopedic Research Society in San Diego (Feb. 2017)
2. Gilbert JL, Li Z, **Zhu D**, Kubacki GW. “Tribocorrosion Heredity Integral Modeling of Abrasion-Current-Impedance-Voltage Relationships”. Annual Meeting of the Society for Biomaterials in Minneapolis, MN (Mar. 2017)
3. Gilbert JL, **Zhu D**, Smith SM, Pierre D. “A Model of Taper Seating Impaction: Head Size, Substrate Stiffness and Impulse Effects”. Annual Meeting of the orthopedic Research Society in New Orleans, LA (Feb. 2018)
4. **Zhu D**, Khullar P, Gilbert JL. “Long-term Fretting Corrosion Behavior of Si₃N₄/Ti-6Al-4V Head Neck Taper Interface”. Annual Meeting of the Orthopedic Research Society, in Austin, TX (Feb. 2019)
5. **Zhu D**, Smith SM, Pierre D, Gilbert JL, Chinn J. “Effect of Multipurpose Care Solutions Upon Physical Dimensions of Silicone Hydrogel Contact Lenses”. Annual Meeting of the Society for Biomaterials in Seattle, WA (Mar. 2019)
6. Khullar P, Gilbert JL, **Zhu D**. “Modular Head-Neck Taper Fretting Mechanics: Si₃N₄ vs CoCrMo Head on Ti-6Al-4V Trunnion”. Annual Meeting of the International Society for Technology in Arthroplasty in Toronto, Canada (Feb. 2019)
7. **Zhu D**, Liu Y, Gilbert JL. “Fretting Corrosion Debris Analysis of CoCrMo Alloy in Physiological Phosphate Buffered Saline”. Annual Meeting of the Orthopedic Research Society in Phoenix, AZ (Feb. 2020)
8. Liu Y, **Zhu D**, Gilbert JL. “In-situ Nanoscale Wear of Native Titanium Oxide by Partial Removal Using Atomic Force Microscopy”. World Biomaterials Congress in Glasgow, Scotland (Dec. 2020) (Conference is cancelled due to COVID-19)

9. **Zhu D**, Liu Y, Gilbert JL. “Micromechanical Measurement of Adhesion of Dehydrating Silicone Hydrogel Contact Lenses”. Annual Meeting of the Adhesion Society in Charleston, SC (Feb. 2020)
10. **Zhu D**, Gilbert JL. “Demonstration of a Tribo-corrosion Model by Using Single Asperity Tribo-corrosion test on CoCrMo Alloy Surface”. Corrosion Conference & Expo, Houston in TX (Jun. 2020) (*Conference is cancelled due to COVID-19*)

Professional Members:

Society for Biomaterials, SFB (2017 - present)

Orthopedic Research Society, ORS (2017 - present)